2022

S-values for Holmium-166, Lutetium-177 and Yttrium-90 for the ICRP 110 voxel phantom and ICRP 145 mesh phantom using the Geant4/GATE Monte Carlo tool

Samuel Montgomery Lilli

UNIVERSITY
OF WOLLONGONG
AUSTRALIA

S-values for Holmium-166, Lutetium-177 and Yttrium-90 for the ICRP 110 voxel phantom and ICRP 145 mesh phantom using the Geant4/GATE Monte Carlo tool

Samuel Montgomery Lilli

This thesis is presented as part of the requirements for the conferral of the degree:

Masters of Research (Medical and Radiation Physics)

Supervisor:
Dr. A. Malaroda

Co-supervisor:
Assoc. Prof. S. Guatelli

The University of Wollongong
School of Physics, Centre for Medical and Radiation Physics

March 2022

This research has been conducted with the support of an Australian Government Research Training Program Scholarship.

Declaration

I, *Samuel Montgomery Lilli*, declare that this thesis is submitted in partial fulfilment of the requirements for the conferral of the degree *Masters of Research (Medical and Radiation Physics)*, from the University of Wollongong, is wholly my own work unless otherwise referenced or acknowledged. This document has not been submitted for qualifications at any other academic institution.

Samuel Montgomery Lilli

September 4, 2022

Abstract

In Molecular Radiation Therapy, the estimation of energy absorbed within tissue is critical for the assessment of the efficacy of radiopharmaceuticals. Computational phantoms are a valuable tool to estimate radiation dose and to ensure that radiation dose to healthy tissue is minimised whilst still achieving a therapeutic level of radiation dose to disease cells.
The International Commission on Radiological Protection (ICRP) has published several computational phantoms for the radiation protection of the population, amongst these are female and male adult voxelised phantoms (ICRP Publication 110) and adult mesh reference phantoms (ICRP Publication 145). The ICRP 110 voxelised phantoms have been widely used for the investigation of radiation dose from internalization of radionuclides. The ICRP 145 mesh phantom has multiple advantages compared to the voxel phantom, with the ability to morph the phantom, as well as create more accurate organ shapes with the availability of rendering software. The aim of this study was to implement the latter in the Geant4/GATE Monte Carlo tool and assess its performance when compared to the ICRP 110 phantom, of which it is an adaptation.
The ICRP 145 mesh phantom was implemented in the Geant4/GATE Monte Carlo simulation environment, making use of the Geant4 C++ classes allowing recording dose in a mesh geometry. Radiation doses to lungs, kidneys, pancreas and spleen of the ICRP 145 adult phantoms were estimated from the distributions of Holmium-166, Lutetium-177 and Yttrium-90 in spherical hepatic lesions of sizes ranging between 0.1 and 3 cm. These were then compared with radiation doses estimated using the voxelised ICRP 110 phantoms for the same lesions. These absorbed dose values were used to calculate S-values, the mean absorbed dose to a target organ per unit cumulated activity in a source organ. This S-value is a specific value for radionuclides and phantoms which describe dose to a target organ. These radionuclides were chosen as candidates in hepatic radioembolization using microspheres and to investigate their impact on radiation dose to healthy surrounding organs.
Significant differences in the radiation deposited in organs can were noted between the ICRP 145 and the ICRP 110 phantoms. This is due to the differences in mass and volume of organs and tissues between the two phantoms, this also is the reason for variation between male and female phantoms. However when the mass dependence was removed, the dose deposited to the liver was similar to that of the ICRP 110 phantoms. However, in this study and for the organs investigated outside the liver (kidneys, pancreas and lungs) the coefficient of variation was as large as 100% due to low hits. As expected, the radionuclide giving the maximum dose to the surrounding tissues is Y-90 (with an S-value Right Lung $\leftarrow$ Lesion of $1.296 \times 10^{-9}\ mGyMBq^{-1}s^{-1}$ compared to $5.023 \times 10^{-11}\ mGyMBq^{-1}s^{-1}$ for Ho-166

and 4.190×10^{-11} $mGyMBq^{-1}s^{-1}$ for Lu-177) while the radionuclide depositing the maximal energy locally was Lu-177.

Acknowledgments

I would like to thank Dr. Alessandra Malaroda for allowing me to conduct this research project through the University of Wollongong. Her knowledge and expertise in the field is second to none, and I have benefited greatly from working with her.

I would like to thank my co-supervisor Dr. Susanna Guatelli. Dr Guatelli ensured this project ran smoothly and the final thesis is of the top quality. Dr Guatelli's expertise in Geant4 has allowed us to ensure the simulations conducted have statistical significance, and are physically precise.

I would like to also thank Professor Alexey Pan for his assistance in thesis writing, literature and presentation skills. Alexey's insight and encouragement to create presentations of the highest standard have allowed me to excel in presenting.

I would like to thank David Bolst. David was instrumental in helping me to access and operate the NCI cluster, and ensure our simulations ran smoothly.

I would like to thank Distinguished Professor Anatoly Rosenfeld, for inspiring me to follow the path I currently find myself on, and pursuing a career in Nuclear Medicine.

I am also incredibly blessed to be supported by my parents, Fiona Mackey and Beraldo Lilli, and my partner Aylah West, assisting with editing, proofing and motivation.

Contents

List of Figures

List of Tables

List of Abbreviations and Definitions

AF - Absorbed Fraction
AIHW - Australian Institute of Health and Welfare
ALARA - As low as reasonably achievable
CSFA - Carrier-free Specific Activity
CT - Computed Tomography
DAWN - Data Analysis WorkbeNch
DC - Dose Coefficient
EC - Electron Capture
EGSnrc - Electron gamma shower
EM - Electromagnetic
GATE - Geant4 Application for Tomographic Emission
Geant4 - Geometry and Tracking
HCC - Hepatocellular Carcinoma
ICRP - International Commission on Radiological Protection
ICRU - International Commission on Radiation Units and Measurements
LET - Linear Energy Transfer
MCNP - Monte Carlo N-Particle
MIRD - Medical Internal Radiation Dose
MRCP - Mesh-reference Computational Phantom
NURBS - Non-uniform rational B-spline
PET - Positron Emission Tomography
PM - Polgyon Mesh
PSMA - Prostate-specific membrane antigen
RBM - Red Bone Marrow
SAF - Specific Absorbed Fraction
SPECT - Single Photon Emission Computed Tomography
S-value - Mean absorbed dose to a target organ t per unit of cumulated activity in a source region s
TACE - Trans-arterial Chemoembolisation
TARE - Trans-arterial Radioembolisation
TM - Tetrahedral Mesh
YBM - Yellow Bone Marrow

Chapter 1

Introduction

1.1 Cancer in Australia

Cancer is a disease where tissue with compromised cell growth and cell division invades other nearby tissue. These cancerous cells have originated from one or more cells that had sustained some damage which did not lead to cell death but to an abnormal cell growth giving the cells the ability to spread.

Cancer is still a significant cause of disease and death in the world. In Australia, data recorded by the Australian Institute of Health and Welfare (AIHW), reports that between 2017 and 2021 there was an estimated seven hundred thousand Australians that were diagnosed with a form of cancer [1]. Thanks to a better understanding of the disease and to new treatment regiments, in 2019 7 cancer patients out of 10 survived at least 5 years post diagnosis, up from 5 in 10 patients 30 years earlier [2]. This is also reflected in a decreasing mortality rate, with only 3 in 10 deaths in Australia due to cancer, and a decrease in the incidence rate since 2008 as summarised in cancer statistics from 1982, in Figure 1.1 [1]. This trend is also observed in Figure 1.2, where the actual rate and projected rate has decreased since 2008, despite the number of cases increasing over time [1].

The decrease in mortality rates in Australia can be accounted for by the use of radiation therapy (external beam and radionuclide) for the treatment of cancer. Radiotherapy kills cancer by damaging the DNA strand in the cancer. Some radiation directly breaks the DNA strand (direct damage) but most cell death results from indirect damage from hydroxyl free radicals being produced (OH^-) and these cause DNA breaks. According to literature, if two base pairs are broken within a distance of four base pairs of each other they are unlikely to repair and cell death occurs [3]. External beam radiotherapy utilises electrons, photons, protons and heavy ions. These are delivered to the tumour volume, and can be used in conjunction with surgery to either shrink the tumour volume prior to surgery or kill the cancerous cells post surgery. These particles will interact with the tumorous cells in different manners based on their linear energy transfer (LET). High LET radiation will deposit a large amount of energy in a short range, whilst a low LET will deposit less energy in the same range [4]. This is a consideration for radiotherapy (external beam and radionuclide therapy) as alpha particles have the highest LET, and in turn will

deposit the most dose (and therefore largest biological damage) to tumorous cells. The other form of radiotherapy is internal radiation, utilising radioactive sources secured in seeds which are directly implanted into the tumour volume (Brachytherapy) or sources chelated to pharmaceuticals [5]. These radiopharmaceuticals can systemically target metastatic cancers in the body.

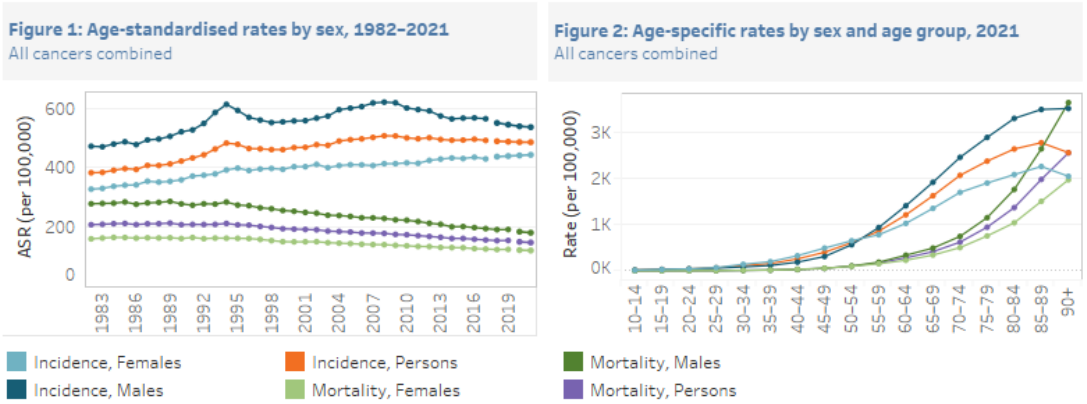

Table 1: Summary of projected incidence and mortality statistics in 2021 by sex
All cancers combined

	Incidence			Mortality		
	Males	Females	Persons	Males	Females	Persons
Count	80,371	70,411	150,782	27,600	21,621	49,221
Crude rate	616.4	530.9	573.3	211.7	163.0	187.1
ASR (Australian Population)	536.7	443.7	486.1	182.0	122.3	149.1
ASR (WHO Standard)	390.7	337.9	362.0	117.7	82.0	98.3
ASR (Segi Standard)	347.6	304.5	324.3	98.5	69.7	83.0

Rates are expressed as per 100,000 population.

Figure 1.1: Summary of Cancer Data in Australia since 1982 [1]

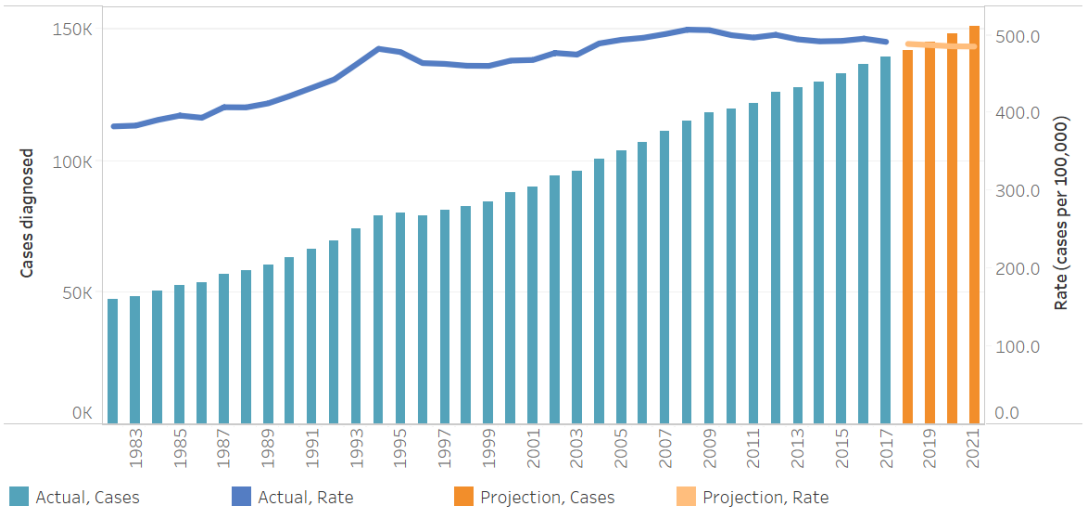

Figure 1.2: All cancers incidence counts and age-standardised rates for all persons [1]

1.1.1 Liver Cancer

Liver cancer shows primarily as a malignant tumour and is often found in patients suffering from a pre-existing liver disease [6]. Liver cancer has a much larger incidence in men (13.2 males per 100 000 individuals compared to 4.3 females) [2], and has the poorest survival rate (19%) of the most commonly diagnosed cancers in men, due to other underlying health conditions that are often associated with the disease [7]. The primary form of liver cancer is hepatocellular carcinoma (HCC), with liver cancer being the leading cause of cancer death globally [8]. Computed tomography (CT) is the method of choice for the diagnosis of HCC, with the use of pre-contrast and three post-contrast (late hepatic, arterial and delayed) image to visualise HCC. CT has excellent sensitivity for lesions greater than 2cm, with sensitivity reducing with reduced lesion size [8]. For patients diagnosed, HCC is surveyed using ultrasounds in conjunction with the monitoring of a serum marker (α-fetoprotein)[8]. Australia's management works on a curative where possible basis, often resulting in surgical and non-ablative therapies. The most common non-ablative therapy is transarterial chemoembolisation (TACE), where chemotherapy and embolic substances are injected through the hepatic artery. Hepatic carcinomas are supplied through this arterial branch, with this method providing a 75-80% disease control rate in support with surgical therapies [9]. Transarterial radioembolisation (TARE) utilises radioembolisation with the selective delivery of radionuclides, usually the pure beta emitting Yttrium-90, to primary or metastatic liver cancer via radiolabeled beads. This has been shown to result in longer time to progression and lower toxicity than conventional chemotherapy treatments [10]. TARE is mostly used in intermediate or locally advanced HCC cases, with the radiation treatment allowing for surgical responses [8].

1.2 Molecular Radiation Therapy

Radiation emitted by radioactive isotopes can be exploited to cause damage to cells. These radionuclides can be attached to drugs that can target specific cellular receptors expressed mainly in diseased (cancerous) cells, minimizing uptake in healthy tissue [11]. The treatment of benign or malignant diseases with the use of internally distributed radionuclides is called Molecular Radiation Therapy (MRT).

The ability to selectively deliver radiation dose to targeted cells whilst sparing healthy tissue is one of the advantages of MRT over other treatments. In fact, MRT is an effective method to target metastatic cancer cells [12]. Moreover, the choice of short range beta or of alpha emitting radionuclides ensures minimizing the radiation dose to healthy surrounding or neighbouring tissue.

The radiation dose delivered by the radiopharmaceutical is determined by its pharmacokinetics, which describes how the radionuclide moves between tissues and organs as a function of time [13]. The pharmacokinetics of the radiopharmaceutical differs in each individual and information on the radiopharmaceutical's pharmacokinetics can be obtained by administering radionuclides that can emit also photons of a useful imaging energy (between 80 and 400 keV) [14].

Ideal radionuclides for MRT emit short range particles, such as beta or alpha particles, so to deposit most of their energy locally, they have a half-life of the order of days to maximise the time the therapy is given without having long term effect and, potentially, emit photons of energies that can be imaged using a SPECT or a PET camera. Radionuclides such as Lutetium-177 (gamma emissions at 112 keV and 208 keV), Yttrium-90 (positron emission at 936 keV) or Holmium-166 (gamma emission at 83 keV) meet these criteria [11],[15].

1.2.1 Trans-arterial Radioembolisation

One of the strategies to manage cancer is to cut off its blood supply (embolisation) so to starve the cells of oxygen and nutrients. Trans-arterial radioembolisation (TARE) achieves this by injecting embolisation agents labelled with radionuclides into the arterial blood supply [16]. An established application of this technique is the trans-arterial embolisation of liver cancer [17] with microspheres labelled with the pure beta emitter Y-90. The microspheres will lodge into the small vessels of the tumour where they will emit radiation. The β^- particles have a short range (millimetres) and will deposit their energy in the tissue.

This method generates a large dose level to tumour, by injecting the spheres through a catheter, the cancer draws upon hepatic arterial blood while the portal vein provides the main blood supply for healthy liver tissue [18]. 1 GBq of Y-90 labelled microspheres will deposit 50Gy/kg to the patient [17]. There are two commercially available spheres which are commonly used for radioembolisation; the glass based TheraSphere®
(https://www.bostonscientific.com) and the resin based SIR-Sphere®(`https://www.sirtex.com/us/`). The TheraSphere®(MDS Nordion, Ottawa, Canada) uses a non-biodegradable glass sphere, ranging from 20-30 microns in diameter with each micron holding an activity of 2500 Becquerel at time of calibration [18]. This varies slightly to the SIR-Sphere® (Sirtex, Lane Cove, Australia) which utilises a biodegradable resin sphere. The resin has a lower density than the glass sphere however is slightly larger (20-60 microns in diameter) and is beneficial for patients with metastatic cancers in the liver. These spheres each contain a specific activity of 50 Bq at the time of calibration. Both these spheres are valuable for treating liver tumours which are inoperable, with a minimal level of invasion required whilst delivering a high dose of radiation to the targeted area. A difference between the resin and glass spheres is the type of distribution throughout the liver, the glass spheres homogeneously distributed while the resin spheres are heterogeneously distributed [19]. Table 1.1 describes the characteristics of each of these microspheres, however Sangro et. al., [20] demonstrates the equivalence for the use of either microsphere.

1.2.2 Dosimetry in Molecular Radiation Therapy

In radiation therapy, it is important to be able to assess the radiation dose imparted to the diseased cells and to healthy tissue. The methodology to estimate dose in MRT is discussed in chapter 2 (Section 2.3), in summary knowledge of the type of emission, energy of emitted particles and location of the radionuclide in the body is required, together with information on the time the radionuclide will spend in each

	Sir-Spheres®	TheraSphere®
Diameters (μm)	32 ± 10	22 ± 10
Specific weight (g/dL)	1.6	3.6
Activity per microsphere to date calibration (Bq)	50	2500
Number of microsphere (vial, million)	40-80	1.2-8
Material	Resin	Glass
Activity in the vial (GBq)	$3 \pm 10\%$	3,5,7,10,15 or 20

Table 1.1: Characteristics of Sir-Spheres® & TheraSphere® [21]

organ or tissue as this will determine how many particles and how much energy has been released by the radionuclide.

In MRT, radionuclides are chosen so that most of the energy released is deposited close to the position of emission, however some dose will be deposited further away from where the radiopharmaceutical has been taken up, this can lead to radiation dose to healthy tissue. However, radiation dose to healthy tissue is also due to the radiopharmaceutical taken up in the healthy tissue itself. An example is the radiation dose to kidneys due to radiopharmaceutical clearance from Y-90 microsphere therapy.

In trans-arterial radioembolisation, the local administration of the radiopharmaceutical, via the blood supply, highly reduces the possibility of the radiopharmaceutical to redistribute throughout the patient's body. Radiation dose to neighbouring organs will be mainly due to emitted particles (photons or beta electrons) that have enough energy to travel the distance [16].

Computational models of the uptake of radiopharmaceuticals in patients offer a flexible tool to investigate radiation dose to organs and tissues from Molecular Radiation Therapy. These phantoms are analytical, voxelised or tetrahedral representation of standard adult or children population [22] and allow radiation dose estimation when implemented in Monte Carlo codes.
Dosimetry refers to the determination of energy deposition in tissue through the use of measurements and calculations. In most cases, patients are administered the same activity on each therapy cycle, and will often not consider the variations in metabolic clearance or uptake of a radiopharmaceutical in different individuals. *MIRD pamphlet 21* [23] outlines a general guideline for dose estimation whilst *MIRD pamphlet 23* provides best-practice SPECT guidance for radionuclide dosimetry [24], however it is demonstrated in Strigari et al., [25] that 48 of 79 studies demonstrated an absorbed radiation dose-effect in MRT. The study suggests 'dosimetry-based personalised treatments would improve outcome and increase survival' as well as tissue toxicity [25]. This personalised dosimetry is time consuming and must be obtained from quantitative imaging studies for the patient [26].

Despite the general guidelines supplied by MIRD, there still exists a large amount of variation in dosimetry measurements. Uribe et al., [27] took 119 submissions that were asked to present details and results from a ^{177}Lu dosimetry challenge designed by the Society of Nuclear Medicine and Molecular Imaging (SNMMI). Of the sub-

missions, 60% used voxelised dose methods, with 47% of those being commercially available software. In these voxelised results, organ volumes differed up to 49.8% whilst lesion's volumes showed a max difference of 176%. With computational calculations, an important consideration is also the time to complete computations, in which the median segmentation time was 43 minutes and total simulation time was 89 minutes [27]. This variability demonstrates the need for a standardised method and procedure for the determination of nuclear medicine dosimetric calculations. Mattsson et al., also discusses the need for a review of radiopharmaceutical bio-kinetic data, with some radiopharmaceutical data being more than 20 years old [28],[29]. As computing processes have improved, there is a need for the reassessment of these for a more accurate representation of the biokinetic processes through the body. The limited number of subjects per study in both genders and varying ages has generated a lack of representation in some categories [28].

In order to improve dosimetric calculations (rather than have radiation-absorbed dose derived from models and bio-kinetics) internal dosimetry programs have been developed. IDAC-Dose2.1 was developed based on the ICRP133 publication [30]. The program calls from the ICRP107 decay database [31], considering 83 different source regions and irradiating 47 target tissues [32]. IDAC was validated against the ICRP dosimetry program, Dose and Risk calculation (DCAL) and employs the same computational framework. IDAC-Dose2.1 has a sub-module for absorbed dose estimates in radiopharmaceutical therapy [32]. IDAC-Dose2.1 also calculated absorbed doses in spherical structures 1mm to 9cm in diameter.

1.3 The ICRP and the evolution of computational phantoms for radiation protection

The International Commission on Radiological Protection (ICRP) is an independent, international organisation that is the primary body in the protection of people, animals and the environment from ionising radiation [33]. In order to protect people from ionising radiation, the commission has used, and published information on, computational phantoms that, implemented into radiation transport Monte Carlo codes, allow to investigate radiation risks to the population. In 2009, the ICRP presented a voxelised computational phantom of the reference male and female [33], these computational phantoms can be and have been used for the assessment of radiation dose for medical use, such as external radiation beam therapy or molecular radiation therapy.

Before the development of voxelised computational phantoms, mathematical models were utilised to determined dosimetric quantity such as Specific Absorbed Fractions or S-values (see Chapter 2.4.1-3). These phantoms have evolved into voxelised phantoms, such as the ICRP 110 phantoms, based on magnetic resonance and computed tomographic models of the human body, and then into Adult Mesh-type reference computational phantoms. In voxel phantoms, slice thickness is in the order of a few

millimetres, which is insufficient for calculating dose to areas of the body such as the eye lens, the skin, and organ walls [34]. One of the advantages of the new ICRP 145 phantoms, with its polygon mesh, is to allow dosimetric calculations that are closer matched to individuals, improving safety and accuracy [34].

1.3.1 ICRP 110 voxelised phantom

The voxelised adult male and adult female reference phantoms, originally published in ICRP's 2007 recommendations [35], are based on the anatomical parameters published in ICRP's 2002 publication [36]. At the time, the best methodology was the use of voxels to define organs and tissues. These voxel phantoms are based on high-resolution scans of male and female patients, if a male or female phantom was required, the voxel dimensions needed to be altered account for different organ dimensions and masses for males and females. The difference in the number of voxels (approx. 2 million for males and 4 million for females) lead to a discrepancy in the resolution of the two phantoms. However, despite improvements to the models based on the GSF Munich voxel phantoms [37, 38], there are still limitations to the voxel models for respiratory and alimentary tracts, as well as the difficulty in deforming the phantoms for paediatric patients. These phantoms have been developed from CT high-resolution scans of a male and female patient, which information allowed a spatial resolution of 2.137 x 2.137 x 8 mm^3 for the male phantom and 1.775 x 1.775 x 4.8 mm^3 for the female phantom [33]. The voxelised models are limited by the low spatial resolution as some tissues were not possible to be segmented directly, e.g. the lens of the eyes, and they had to be added to the model post-segmentation. Other organs such as the skin layer or the extra-thoracic (ET) airways had to be represented by an entire voxel layer. Bronchioles were also not possible to segment, and these are taken into account in the lung tissue assuming a lung density given by the weighted average of the two tissues densities including air [39]. Moreover, voxelised human phantoms are difficult to scale to represent the range of sizes and shapes in the human population and between children and adults.

1.3.2 ICRP 145 mesh-type phantom

In 2018, mesh-type reference phantoms (MRCP) were generated from the ICRP 110 voxelised phantoms using a TetGen formatting program [40], Figure 1.3. The majority of the structures were implemented directly through conversion of the voxel phantom to the polygon-surface phantom using 3D-DOCTOR (Able Software Corp., Lexington, MA) [41]. Figure 1.4, reproduced from the conversion of the voxelised liver to the polygon-surface [42], summarises the process of converting and refining the conversion of a voxelised liver to a polygon-surface and then modifying the volumes to match the liver mass [36].

More complex organs, such as the large intestine, required the use of the non-uniform rational B-spline (NURBS) format; the small intestine was developed using a simple pipe model [45]. Other complex anatomical features (skull, ribs and spine), were generated using a well-defined model adjusted three-dimensionally to match the ICRP reference phantoms [43]. So in order to handle the NURBS or mesh-based phantoms, the development of Monte Carlo methods has been at the forefront of research [46], [47] and led to the development of programs such as GATE.

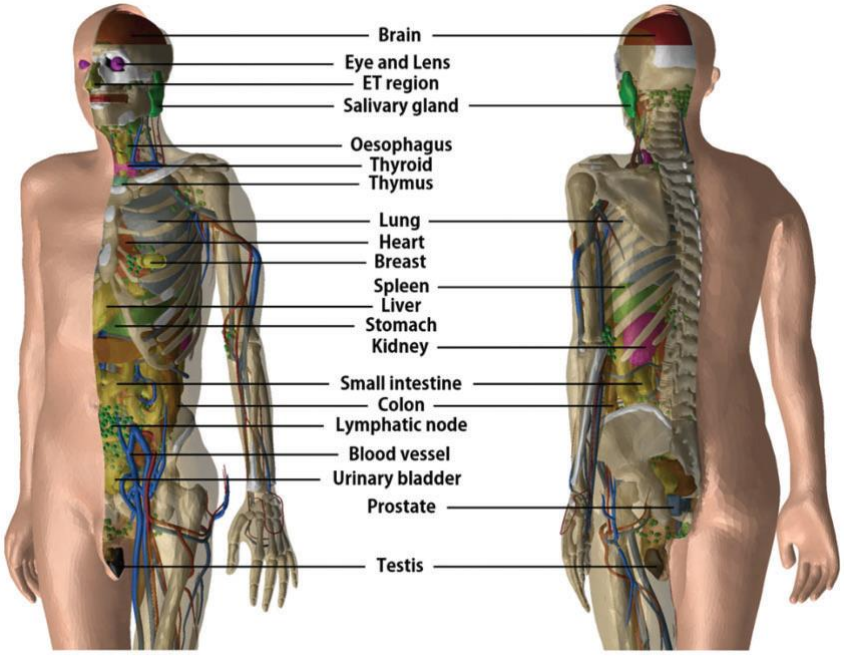

Figure 1.3: Male mesh-reference computational phantom (ICRP 145, 2020)[43]

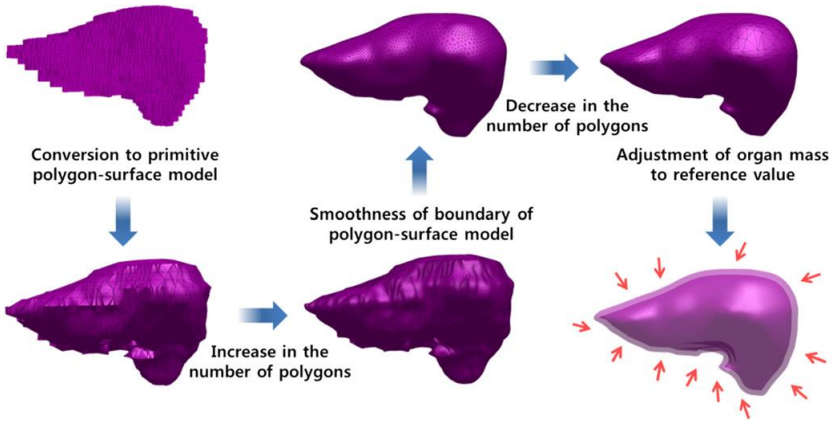

Figure 1.4: Construction Process of Liver (Yeom, 2013) [44]

One of the advantages of the new mesh phantom is the ability to simulate thin surfaces or tracts. This, in particular, allows the definition of a continuous skin layer of 50 μm thickness as target regions so that radiation dose to cells at risk in the skin can be assessed. The ICRP 145 phantoms are covered by a continuous, thin skin layer, rather than the voxel layer around the ICRP 110 phantom. Similar techniques have been used to define thin tissue structures such as the stomach, the oesophagus or the urinary bladder wall. Another major improvement with respect to the ICRP 110 phantom is the refined modelling of the major blood vessels, which were segmented in the ICRP 110 with loss of resolution, and the implementation of small blood vessels joined to the major blood vessels. However, the intra-organ vasculature is still not modelled.

1.3.3 Phantom Evolution

In order to obtain general dose estimates, simulations are conducted on computational phantoms. Human computational phantoms have developed substantially over the last 50 years as computing power has increased. Phantoms began using mathematical equations to generate solid geometric objects which could define different shapes whilst generating boundaries (ORNL, MIRD) and has been the basis for many reference dose and risk coefficients [48]. These are useful for morphing to represent paediatric models, however are very poor in representing realistic anatomy. Phantoms then developed into voxel phantoms, where the phantom was derived from a 3D array of voxels, with each voxel representing a specific organ (includes elemental composition and density). The voxels are generated through segmentation of individual image slices from a CT or MR scan, and provide a high level of realism [48]. However, the voxels are poor for morphing of body sizes, due to the alteration of voxel size and composition and morphing occurs. In order to generate accurate phantoms for different patients (adult male, adult female, child, baby) CT/MR scans would be required with each requiring segmentation. The most recent computational phantom is the hybrid or mesh phantom, as they are a combination of the realism of voxel anatomy and the flexibility of the mathematical models. These phantoms are generated using CT/MR scans, and generating a 3D rendering of the subject anatomy. The mesh phantoms are advantageous over the prior models as they have correct spatial anatomy (unlike mathematical) and have a continuous and smooth rendering in all directions (unlike voxels) [48]. 3D rendering software also allows for the ability of developers to reshape surface in the anatomy, seen in the 3D-DOCTOR, where individual regions of polygon mesh can be adjusted inwards or outwards. These phantoms are valuable for defining dose and risk coefficients, however are limited in individual patient dosimetry. As each patient will react differently to radiation (stochastic effects), and the inability to correctly morph the phantom to individual patients (down to correct organ size and mass), individual patient dosimetry is not recommended.

1.4 Geant4/GATE Monte Carlo tool

GATE (Geant4 Application for Tomographic Emission) is an implementation of the Monte Carlo simulation toolkit Geant4 [49], and was developed for the investigation of nuclear medicine SPECT and PET imaging [50]. GATE uses a macro language to define complex geometry, the particle source, and the physics of the Monte Carlo simulation, making use of the very well established and validated Geant4 C++ classes. Moreover, it can handle tetrahedral mesh geometries as well as the energy deposited within these geometries. The established nature of Geant4 physics, and the ability of GATE to generate complex geometries made the use of GATE suitable for this study.

1.5 Implementation of ICRP 145 phantom in Geant4/GATE

The aim of this project was to implement the ICRP 145 mesh-reference phantom in the Geant4/GATE Monte Carlo tool. Radiation doses to organs from the distributions of Holmium-166, Lutetium-177 and Yttrium-90 in a spherical hepatic lesion have been compared with radiation doses estimated using the voxelised ICRP 110 phantom. These radionuclides have been chosen to investigate their impact on radiation dose to healthy surrounding organs when used in hepatic radioembolization using microspheres. The S-values, a measure of the mean absorbed dose to the kidneys, pancreas and lungs, per unit of cumulated activity in the liver, have been determined for these radionuclides. These results allow for comparison between the two phantoms for internal dosimetry measurements, as well as the three radionuclides for their use in nuclear medicine.

1.6 Comparison of radiation dose to neighbouring organs from TARE

Table 1.1 shows the physical characteristics of the three radionuclides investigated in this project. These radionuclides are suitable for TARE, as they are primarily beta emitters (^{166}Ho and ^{177}Lu have low energy gamma emission) and have a short range in tissue [51], [52], [53]. As shown in Table 1.2, ^{166}Ho and ^{177}Lu have low energy gamma emissions which has the advantage of being utilised for SPECT imaging [16]. These radionuclides can be injected as loaded microspheres (see Chapter 2.3.3), and have a homogenous distribution throughout the tumour.

Radionuclide	Half-life ($t_{1/2}$)	$E_{\beta Max}$ (MeV, %)	E_{γ}(keV, %)	Maximum Tissue Penetration Range (mm)
^{90}Y	64.1 h	2.284 (99.9)	Nil	11
^{166}Ho	26.8 h	1.854 (48.8) 1.774 (49.9)	81 (6.6)	8.7
^{177}Lu	6.716 days	0.497 (78.6)	113 (6.6) 208 (11)	2.2

Table 1.2: Properties of three common radionuclides for TARE [16]

Chapter 2

Physics Principles

2.1 Radiation Dose

Radiation dose (or absorbed dose), D is the mean energy of ionising radiation ($d\tilde{\epsilon}$) deposited in an absorber per mass (dm). Radiation dose has units of J kg^{-1}, or gray (Gy). This measurement does not take into account the type of ionising radiation.

$$D = \frac{d\tilde{\epsilon}}{dm} \tag{2.1}$$

Equivalent dose, indicated by H_T takes into account relative biological damage caused by radiation interacting with a particular tissue or organ [4]. The biological damage caused to different organs is due to the different level of sensitivity in organs, due to density. The equivalent dose depends on the type and the energy of the radiation. It's unit of measurement is the sievert (Sv) and is given by;

$$H_T = \Sigma_R D_{T,R} \times w_R \tag{2.2}$$

where D_T is the averaged absorbed dose in tissue T, and w_R is the radiation weighting factor. Table 2.2 shows different weighting values for different radiation types.

Type of Radiation	Radiation Weighting Factor (w_R)
x-rays	1
γ-rays	1
Electrons, Positrons	1
Neutrons	Continuous function of neutron energy (see below)
Protons >2MeV	2
α particles, fission fragments, heavy ions	20

Table 2.1: Radiation weighting factors [4]

For neutron radiation weighting factors, the weighting factor depends on the neutron energy.

The effective dose, E is the sum of all the organ equivalent doses. This differs from the whole body dose as the effective dose characterises the non-uniformity of

$E_n < 1MeV$	$2.5 + 18.2e^{-[ln(E_n]^2/6}$
$1MeV \leq E_n \leq 50MeV$	$5.0 + 17.0e^{-[ln(2E_n]^2/6}$
$E_n > 50MeV$	$2.5 + 3.25e^{-[ln(0.04E_n]^2/6}$

Table 2.2: Neutron Radiation Weighting Factors [4]

organ dose distribution. This results in a single value which takes the non-uniformity and dosage to each organ. This was originally used to estimate radiation risk to workers, but is now utilised in nuclear medicine studies. Effective dose has units of sieverts and is calculated by;

$$E = \Sigma_T w_T \times D_T \times w_R = \Sigma_T w_T \times H_T \tag{2.3}$$

where D_T is the average absorbed dose in organ T, w_T is the tissue weighted factor for organ T and w_R is the radiation weighting factor depending on the type of radiation. The only downside to the effective dose measurement is that the calculations are based on the average human. The tissue weighting factor was defined in the ICRP Publication 60 [54] as the ratio of the whole-body dose, which would cause a certain probability of cancer induction to the absorbed dose in that organ [55]. This was superseded by the ICRP 103 Publication [35]. It is also important to note that tissue radio-sensitivity is age dependent, so despite reference phantoms being available for practitioners, this must be considered.

2.2 Radionuclides and Radiopharmaceuticals

A radiopharmaceutical is a pharmaceutical substance with a radioactive isotope attached which can be used for diagnostic or therapeutic purposes. These radio-labelled drugs are designed based on specificity, selectivity and affinity (the chemical forces that cause the drug to associate with the receptor/enzyme) for specific targets [56], [4]. These in conjunction with the pharmokinetics, metabolic profile and the physico-chemical properties of the radionuclide determine a radiopharmaceutical's efficacy [57]. Appendix B outlines the full requirements for the use of radiopharmaceuticals clinically.

Radiopharmaceuticals require specific considerations for different applications. This includes the type and energy of emissions, which determine the availability of useful photons or gamma-rays for counting. Energies of 50-600 keV are useful for external detection as energies below this are highly likely to be absorbed in the body and won't be detected. This also increases dose to patients without providing useful information to practitioners. Finally, the physical half life of the radionuclide needs to be within the range of seconds to days (preferably minutes to hours), to allow for preparation, injection, biodistribution and imaging of the radiopharmaceutical. It is important that the half life is not extensively long, as a large part of the radiation dose will be deposited to the patient after the imaging procedure has been carried out.

2.2.1 Lutetium 177 DOTA-TATE and Lutetium 177 PSMA

Lutetium 177 has a half life of 6.716 days and decays via β^- and γ radiation. As seen in Figure 2.1, $E_{\beta(max)}$ is 497 keV and has a probability of occurring for 78.6% of decays. Beta emissions also occur at 384 keV (9.1%) and 176 keV (12.2%), whilst low-energy gamma photons are emitted at 113 keV (6.6%) and 208 keV (11%) [58]. The beta particles have a mean penetration range of 670 μm, making it ideal for small tumour volumes and for sparing healthy surrounding tissue [11].

Lutetium 177 (^{177}Lu) is a therapeutic radionuclide which is used primarily for the treatment of Somatostatin Receptor (SSTR) expressing neuroendocrine tumours that metastasise amongst the liver. Lutetium-177 when used in conjunction with the pharmaceutical, DOTA-octreotate (DOTA-TATE), to treat these SSTR neuroendocrine tumours [51]. This use of Lutetium-177 in peptide receptor-targeted radionuclide therapy (PRRT) with DOTA-TATE has also allowed for treatment of inoperable neuroendocrine tumours (NETs). Lutetium-177 has more recently been used with prostate-specific membrane antigen (PSMA) which appears in mainly the prostate, as well as in the kidney, lacrimal-, parotid- and sub-mandibular-glands [11]. The radionuclide undergoes β emission for a short range, useful for treatment, while the γ emissions making it useful for imaging.

Lutetium attached to PSMA is a viable option for treatment of metastatic prostate cancer following initial chemotherapy or radiotherapy. PSMA is a glycoprotein which is found in low levels in the prostate, however is largely found in prostate cancers (increased by up to 1000%) [11]. PSMA receptors have a process in which proteins bind to the cell, allowing for uptake of PSMA labelled radioisotopes in the tumour volume. However there are PSMA receptors present in other organs (small intestine, renal tubules) which results in some uptake in healthy tissue.

By the injection of Lutetium-177 labelled radiopharmaceuticals through the right or left hepatic artery, there is an increased uptake by the metastases in the liver. ^{177}Lu radiopharmaceuticals have preferable physical attributes when compared to similar radioisotopes such as Yttrium-90 (^{90}Y) . Yttrium-90 is discussed in depth in Section 2.2.3, however, Yttrium-90 has a larger $E_{\beta(max)}$ of 2.28 MeV and therefore an increased range (12 mm) when compared to Lutetium-177 [11]. Therefore, the dose deposited is more localised, making it valuable for receptor-targeted radionuclide therapy [58], [59].

2.2.2 Holmium 166

Holmium 166 (^{166}Ho) is a radionuclide that can be utilised in the treatment and imaging of liver cancer and liver metastases. Holmium 166 has a half-life of approximately 26.8 hours, and emits beta and gamma radiation. The most attractive component of holmium is that the high energy beta emissions are useful for therapeutic requirements, while the gamma radiation is useful for nuclear medicine imaging (SPECT), as well as Magnetic Resonance Imaging (MRI) due to its paramagnetic

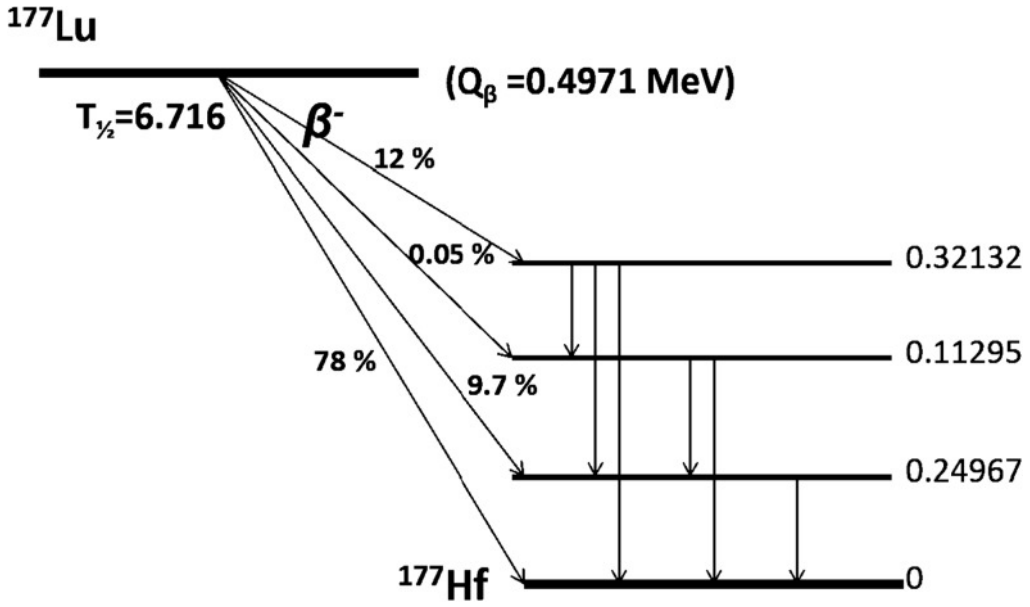

Figure 2.1: Lutetium-177 decay scheme [60]

nature.

Holmium-166 can be produced by two methods, the first is through the neutron activation of ^{165}Ho in a nuclear reactor, Holmium-164 has a natural abundance of 100%, and can be activated by a neutron to form a highly pure ^{166}Ho isotope [15]. However, a part by-product (7×10^6 smaller by product) is the metastable ^{166m}Ho. The metastable Holmium has a half life of 1200 years and similarly emits beta and gamma radiation. The production of the unstable holmium however is far more likely, as the cross section for thermal neutron activated holmium-166 (^{165}Ho$(n,\gamma)^{166}$Ho) is 64 barn compared to 3.4 barn for the production of the metastable holmium-166 (^{165}Ho$(n,\gamma)^{166m}$Ho) [61].

The second production method is through the neutron activation of dysprosium-164. Similarly to the previous method, ^{164}Dy is activated by two neutrons $(2n,\gamma)$ to form the ^{166}Dy isotope [62]. The radionuclide undergoes beta decay with a half-life of 81.5 hours to produce ^{166}Ho. The main benefit to this method is the carrier-free production of Holmium-166, having no metastable holmium production.

Figure 2.2 shows the the two methods for the production of ^{166}Ho, as well as its decay scheme. It emits 1774 and 1854 keV (49.9% and 48.8% yields respectively) beta particles as well as 80 and 1379 keV (6.7% and 0.9% yields respectively) gamma rays. One major advantage Holmium-166 has is its 26.8 hour half life [15], means that more than 90% of the dose will be deposited in the first 4 hours, giving practitioners enough time to image or treat the patient, and the dose is kept to a minimum. This half life compared to a similar alternative, Yttrium-90 (^{90}Y) with a half-life of 64.6 hours, will deposit dose for a longer time.

Holmium has applications for imaging and treatment in the liver using selective internal radiotherapy (SIRT) [63]. Holmium labelled micro-spheres (30 μm diameter) are administered through the hepatic artery and are carried to the target lesion

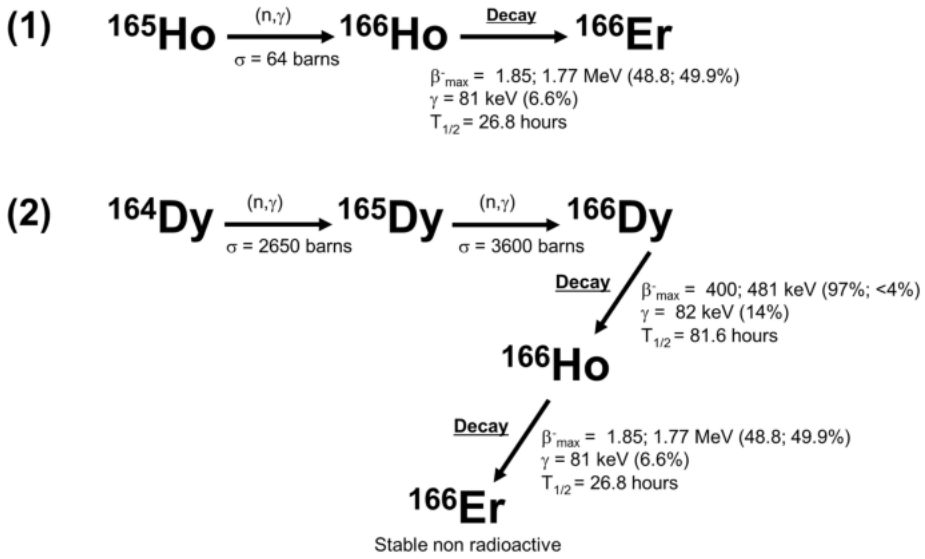

Figure 2.2: Production and decay of ^{166}Ho [15]

[61]. Liver tumours are dependent upon the hepatic artery for blood supply, meaning the micro-spheres are carried directly to the tumour, sparing healthy liver tissue (supplied by the portal vein) [8].

2.2.3 Yttrium-90

Yttrium 90 (^{90}Y) is a therapeutic radioisotope which emits predominantly high energy beta particles, and is commonly used in the treatment of liver metastases. Yttrium 90 possesses a half life of 64.042 hours [64] and decays to Zirconium 90 (Zr-90) in a stable ground state, Figure 2.3. The maximum particle energy emitted from Y-90 is a 2.28 MeV beta particle with a 99.983% probability. The maximum particle energy as well as the 0.94 MeV average energy, generates a high dose deposition in patients from the radionuclide. When comparing the maximum energy of ^{177}Lu and ^{166}Ho, ^{90}Y has the largest maximum particle energy and average energy, therefore will deposit the highest dose per Becquerel of activity. This increased energy also allows the particles to travel further in soft tissue, with the range of beta particles ranging from 2.5mm to 11mm [53].

Ytrrium-90 is most commonly used in radioembolisation for primary and metastatic cancers of the liver (see Section 1.2.1).

2.3 Internal Radiation Dosimetry

Internal radiation dosimetry refers to the analysis of radiation energy deposited in organs by internal radionuclides. Figure 2.4 demonstrates how different forms of radiation can travel; photons have a longer path length compared to electrons, and so we expect to see dose in organs further from the lesion. This compared to electrons which deposit their energy along a short path and so are less likely to deposit dose in organs outside the source. It is important to note that radiation will not be entirely confined to the source for electrons. To ensure the patient is safe and dose

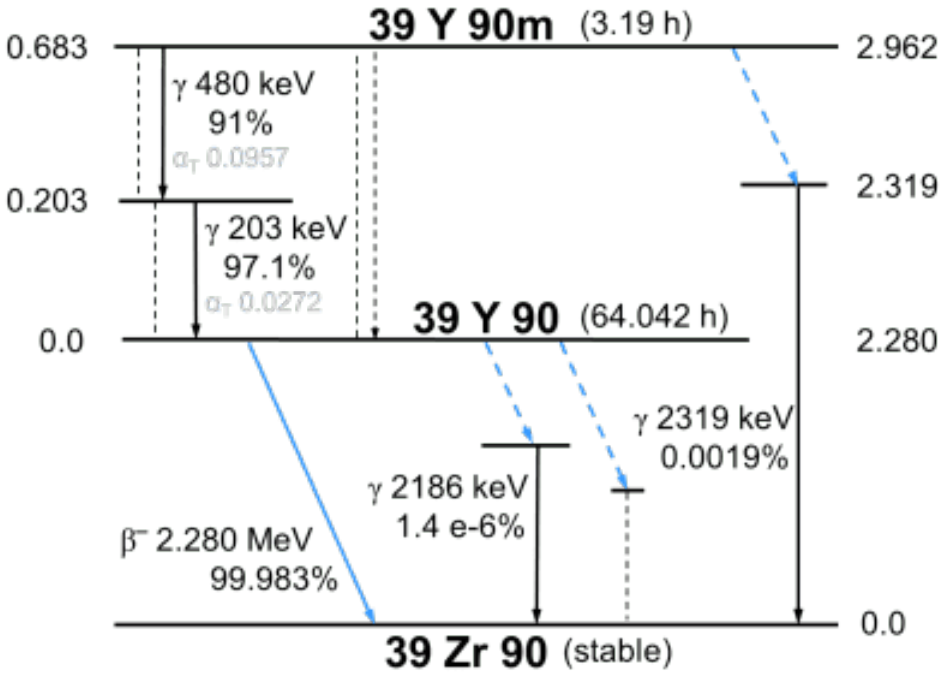

Figure 2.3: Decay of ^{90}Y [65]

to healthy organs is minimised, phantoms studies of internal dosimetry is vital to nuclear medicine and patient safety.

In nuclear medicine, the delivery of radiopharmaceuticals, the activity administered to the patient, the radionuclide itself, pharmokinetics and the disease of the patient all play a role in dose calculations. The calculation of internal dosimetric values can be achieved using the MIRD scheme (from the Medical Internal Radiation Dose Committee of the Society of Nuclear Medicine). The MIRD scheme has received a larger acceptance within the nuclear medicine community for performing these internal dosimetry measurements [4]. This method takes into account the activity of the radionuclide, the energy emission and intensity of these emissions, and the dose which is absorbed dose measured.

The internal dosimetry calculations rely upon the physical, biological and effective half-lives of the radiopharmaceutical. The physical half-life (T_p) refers to the time taken for half of the atoms in the unstable nuclei to become stable. The biological half-life (T_b) is the time to eliminate, by natural processes, half the amount of material. The effective half-life (T_c) is the quantity which includes both the physical, and biological half-lives:

$$\frac{1}{T_c} = \frac{1}{T_b} + \frac{1}{T_p} \tag{2.4}$$

In the MIRD scheme, a source organ is an organ which has radioactive source uptake, and a target organ has dose incident onto it from the source organs. However, a major contributor to dose is the self-dose, which describes radiation dose to an organ which is from the radionuclide within the organ. In order to determine the radiation dose from a source to a target organ the amount of activity in the source

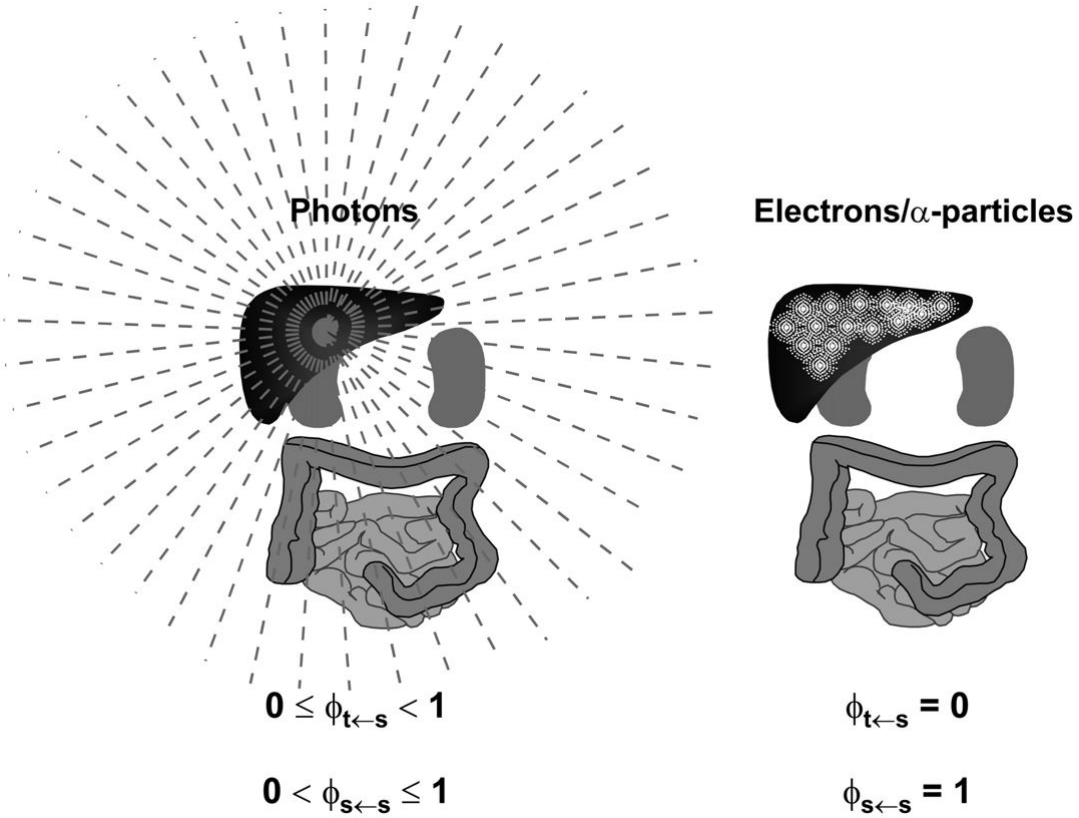

Figure 2.4: Absorbed Fractions for different emissions [23]

and all the relevant half-lives must be taken into account [4]. The self-dose, and the emission of radiation from the target to source also depends on the type of emission as seen in Figure 2.4.

The time integrated activity, $\tilde{A}$ is a product of the amount of radiation activity in the source organ and the length of time the activity is present. It has units of Becquerel seconds (Bq $\cdot sec$) and we can describe the time integrated activity as a time activity curve;

$$\tilde{A}(r_s, T_D) = \int_0^{T_D} A(r_s, t)dt \tag{2.5}$$

In equation 3.2, r_s is the position where source s of activity A is located, while T_D is the time period to integrate over [23].

2.3.1 MIRD Formalisation

The MIRD formalisation was established by a committee subset of the Society of Nuclear Medicine. The group aimed to provide a guideline for assessment of absorbed dose to whole organs, tissue sub-regions, voxelised tissue structures and individual cellular compartments used in diagnostic and therapeutic nuclear medicine [23]. MIRD Pamphlet 21 adopts the dosimetric quantities of equivalent dose and effective dose in evaluations of risk associated with stochastic and tissue effects.

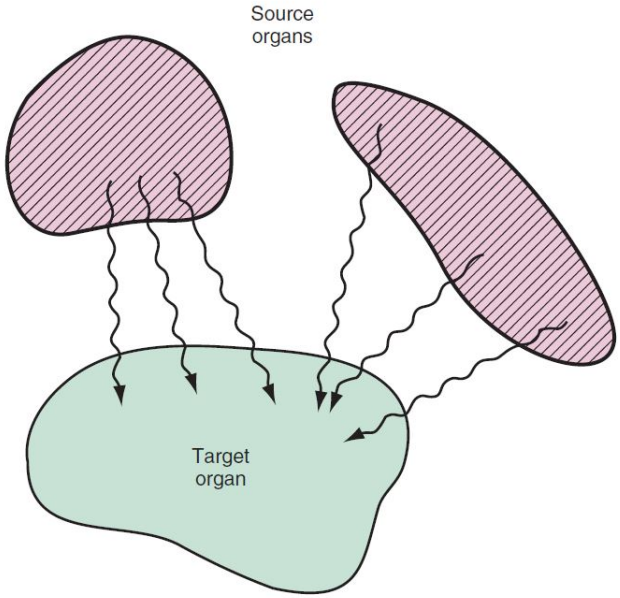

Figure 2.5: Absorbed dose delivered from source to target [4]

Absorbed Dose

Absorbed Dose $D(r_T)$ is defined as the mean energy imparted on a target region r_T per unit mass of that region [66]. The time-dependent dose rate, $\dot{D}$ is given by

$$\dot{D}(r_T, t) = \sum_{r_S} A(r_S, t) S(r_{TS}, t) \tag{2.6}$$

where $A(r_S, t)$ is the time integrated activity of a radiopharmaceutical in the source tissue, r_S. The value $S(r_T \leftarrow r_S, t)$, also known as the S-value, is a radionuclide-specific quantity for the mean absorbed dose delivered to the target organ, r_T at time t per unit activity present in source organ, r_S [23]. For computation phantoms, the S-value is dependent upon the radionuclide in use, as well as the age and sex of the anatomical model selected for use. We can also determine the mean absorbed dose $D(r_T, T_D)$ to target tissue r_T over a defined dose-integration period T_D by

$$\begin{aligned} D(r_T, T_D) &= \int_0^{T_D} \dot{D}(r_T, t) dt \\ &= \sum_{r_s} \int_0^{T_D} \tilde{A}(r_S, t) S(r_{TS}, t) dt \end{aligned} \tag{2.7}$$

where T_D is commonly taken to be infinite, as radionuclides used in nuclear medicine often have a short physical half-life.

2.3.2 S-values

The S-value is the mean absorbed dose to the target organ r_T per unit of cumulated activity in the source region r_S (also known as mean dose per cumulated activity)

[67]. It has units of mGy/MBq · sec. The S-value, is specific to the radionuclide and the computational phantom in use. This is due to the computational phantom defining the spatial geometry and tissue compositions of r_S and r_T. S is given by

$$S(r_T \leftarrow r_S, t) = \frac{1}{M(r_T, t)} \sum_i E_i Y_i \Phi(r_T \leftarrow r_S, E_i, t) \tag{2.8}$$
$$= \frac{1}{M(r_T, t)} \sum_i \Delta\Phi(r_T \leftarrow r_S, E_i, t) = \sum_i \Delta_i \Phi_i$$

where E_i is the mean or individual energy of the i^{th} nuclear transition, Y_i is number of i^{th} nuclear transitions per nuclear transformation, Δ_i is their product, $\phi(r_T \leftarrow r_S, E_i, t)$ is the absorbed fraction, and $M(r_T, t)$ is the time dependent mass of the target tissue r_T [68].

The specific absorbed fraction $\Phi(r_T \leftarrow r_S, E_i, t)$ is defined as the ratio of the absorbed fraction and the target mass. The absorbed fraction is affected by the distance between the source and target organs as the bodies materials attenuate the radiation [14]. For complete dosimetry measurements, the absorbed fraction must be determined for each type of emission and for each source-target pair.

2.4 Monte Carlo in Internal Radiation Dosimetry

2.4.1 The Monte Carlo Method

The Monte Carlo method was proposed by Metropolis and Ulam in 1949 as a method of dealing with a class of problems in mathematical physics [69]. The approach relies on "a statistical approach to the study of differential equations, or more generally, of integro-differential equations that occur in various branches of the natural sciences" [69]. Monte Carlo is distinctive in that it depends on random samples to approximate deterministic quantities. As Monte Carlo is a numerical method for solving mathematical problems, physics problems must be formulated in mathematical terms [70]. The biggest advantage of Monte Carlo comes when the complexity of problems increase, specifically when a problem is 5 dimensions or higher [71]. This is demonstrated in Figure 2.6, where as the complexity of a problem increases (dimensions), the time to solve the problem becomes linear compared to an exponential increase for analytic/deterministic approach. In radiation physics, problems are generally six dimensions or higher [71] making the Monte Carlo method a useful simulation tool for medical physicists. As Monte Carlo relies on statistical methods including sampling and due to the complexity of radiation physics, radiation transport and the stochastic nature of radioactive decay suits the simulation.

2.4.2 Transport of Charged Particles

In radiation transport codes such as that utilising the Monte Carlo method, charged particles play an important role. These include electrons, protons, positrons and

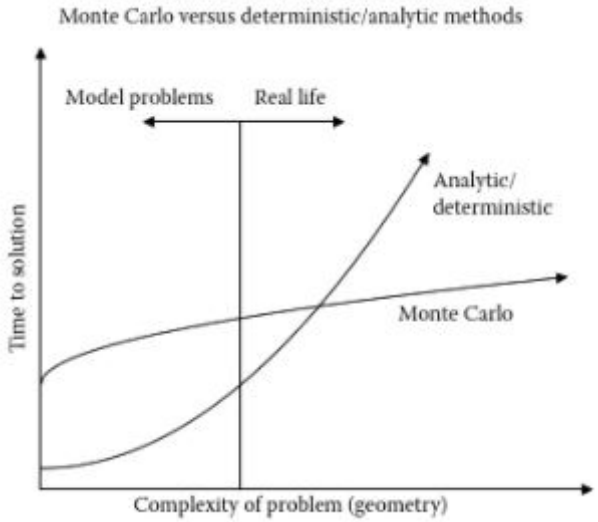

Figure 2.6: Time to solve problem using Monte Carlo against analytic/deterministic approaches [71]

some heavy ions including carbon ions. In Geant4 the transport of these particles through the environment is a result of "Geant4 kernel's Stepping Manager class and the actions of processes which it invokes–physics processes and the Transportation 'process' which identifies the next volume boundary and also the geometrical volume that lies behind it, when the track has reached it" [72]. Geant4 is utilised in this study as GATEs physics processes utilised Geant4, due to being suitable in low energy physics seen in nuclear medicine. An expected length for interaction occurrence is determined through polling the processes which apply to that step, then where the particle interacts is determined [73]. To do this the length of interaction or the Mean Free Path needs to be determined. In order to do this, the number of atoms per volume needs to be determined for interaction probability;

$$n = \frac{N\rho}{A} \tag{2.9}$$

Where N is Avogadro's number, ρ the density of the medium, and A is the mass of a mole. This physics is available in simple materials (body materials included). This formula can be used for materials made of multiple elements by;

$$n_i = \frac{N\rho w_i}{A_i} \tag{2.10}$$

where w_i is the proportion by mass of the i^{th} element. This value, n is the number of atoms per unit volume and is used to determine the mean free path of a process (or interaction length) given by;

$$\lambda(E) = (\sum_i [n_i \cdot \sigma(Z_i, E)])^{-1} \tag{2.11}$$

where $\sigma(Z_i, E)$ is the total cross section per atom of the process and $\sum_i$ runs for all elements which make up the material. The components which make up the bracket is called the macroscopic cross section, with the inverse of this being the mean free path.

Charged particles vary to photons in that they experience a large amount of collisions along their path, depositing energy, before they come to their rest. These interactions often have a minimal change in energy and direction, making it possible to group each small interaction into a single interaction, creating a condensed history simulation [74].

2.4.3 The Monte Carlo Method in Internal Radiation Dosimetry [EGSnrc, Geant4, MCNP]

Monte Carlo in medical physics aims to model nature through simulations that are based on the dynamics and physical principles that exist in the system. The common Monte Carlo simulation platform, Geant4, which is utilised by GATE, has excellent validation in relation to its physics modelling [75]. These have been validated by a comparison between the physics modelling in Geant4 with the real experimental data, whether at a microscopic level (thin target) or macroscopic (thick target) [74]. The use of the Monte Carlo method has seen a drastic growth in the area of medical physics [70]. The number of papers published in the medical physics field utilising Monte Carlo has doubled every five years between 1967 and 2000 [76]. This covers a wide range of fields within medical physics, including testing of silicon micro-dosimeters [77] and hadronic models in carbon ion therapy [78].

There are various Monte Carlo codes which are available to use in medical physics, and more specifically internal radiation dosimetry. These codes and their differences are explored in Pacilio et al., which observes the differences in MCNP4C, EGSnrc, and GEANT4 codes through calculating S-values for voxel dosimetry. The study, observed differences in S-values from beta emissions of radionuclides with MIRD calculations (utilised EGS4 code) [79]. For voxel S-values, differences were noticeable in bremsstrahlung tails or when there is a large contribution from electrons less than 500 keV [79]. Pacilio observed divergence in the bremsstrahlung region (up to about 90% in terms of voxel S-values using EGS4 code) and further photon, electron and the transport of these particles [79]. The code's newest release, MNCP6, has improvements in physics (decay emission treatment) and sources (spontaneous decay). This is important for internal radiation dosimetry, as electrons are a large contributor to dose. The next code is the electron-gamma-shower (EGSnrc), another Monte Carlo toolkit for ionising radiation transport, spanning from low keV energies to GeV energies. Originally EGS, EGSnrc improves on charged particle transport as well as low energy cross sections and geometries.

Geant4 (geometry and tracking), is a general purpose Monte Carlo toolkit which simulates different particle types for a large range of energies [79]. Geant4 was created originally for high energy physics scenarios, however developments have allowed for various applications, including internal dosimetry. Geant4's physics processes to simulate the radiation dosimetry scenarios. However, Geant4 has various

physics packages (shown in Figure 2.7) available to simulate different particle energy ranges. However, the correct physics package for the correct energy range must be selected in order to obtain accurate results. Thus, for the application in nuclear medicine the Low Energy Electromagnetic Physics (Livermore) package is selected. This physics process, developed in 2006 makes use of atomic shell cross section data, as the structure of the shell is more important at lower energies compared to higher energies. The Livermore model includes the photo-electric effect, Compton scattering, Rayleigh scattering, gamma conversion, bremsstrahlung and ionisation [72]. These energy ranges can be defined down to energies smaller than 1 keV, making it valuable for low energy applications.

Phantoms and their development and their place in internal dosimetry (discussed in Section 1.3). However, as the phantoms generated become more complex, then the ability to compute them and physics processes occurring within the phantom, needs to expand. Monte Carlo codes are excellent in simulating high energy physics, however are poor for handling of nuclear medicine or phantom geometries [75].

Physics process	Process class	Model class	Recommended low enery applicability limit of model (*)	High enery applicability limit of model
gamma				
Photo-electric effect	G4PhotoElectricEffect	G4LivermorePhotoElectricModel	250 eV	100 GeV
Polarized photo-electric effect	G4PhotoElectricEffect	G4LivermorePolarizedPhotoElectricModel	250 eV	100 GeV
Compton scattering	G4ComptonScattering	G4LivermoreComptonModel	250 eV	100 GeV
Polarized Compton scattering	G4ComptonScattering	G4LivermorePolarizedComptonModel	250 eV	100 GeV
Rayleigh scattering	G4RayleighScattering	G4LivermoreRayleighModel	250 eV	100 GeV
Polarized Rayleigh scattering	G4RayleighScattering	G4LivermorePolarizedRayleighModel	250 eV	100 GeV
Conversion	G4GammaConversion	G4LivermoreGammaConversionModel	1.022 MeV	100 GeV
Polarized conversion	G4GammaConversion	G4LivermorePolarizedGammaConversionModel	1.022 MeV	100 GeV
e-				
Ionisation	G4eIonisation	G4LivermoreIonisationModel	10 eV	100 GeV
Bremsstrahlung	G4eBremsstrahlung	G4LivermoreBremsstrahlungModel	10 eV	100 GeV

Figure 2.7: Available Physics Processes and Models in Geant4 [72]

2.4.4 GATE

GATE, the Geant4 Application for Tomographic Emission, utilises the Geant4 libraries to "achieve a modular, versatile, scripted simulation toolkit adapted to the field of nuclear medicine" [75]. The novelty of GATE is that the application allows Geant4 (which is a pre-requisite for GATE) to manage the kernel and the physics of the simulation, but allows GATE to create the environment in a user-friendly way. GATE is the only open source Monte Carlo program with user-friendly simulations for dosimetry, imaging and radiotherapy [50]. The development of GATE has come in conjunction with demand for increased demand for accurate, fast and high quality imaging in nuclear medicine, whilst the availability of computer clusters have increased.

GATE was designed with user friendliness in mind, with no knowledge of C++ required to design programs. Secondly, as most nuclear medicine modalities share similar geometries and physics principles, software components can be shared from one context to another. Finally, GATE is modular and is able to develop and evolve

for new applications [75].

Figure 2.8 shows the layered structure of GATE software. At the centre of GATE is Geant4 and its physics processes to simulate experiments. The core and application layer make up the developer layer of GATE. The core layer is made up of the various available classes which form the basis of the GATE program. The classes define to developers what tools are accessible for use, and how they can utilise these tools for their development. These include the mandatory Geant4 tools to generate geometries, the physics classes required to run simulations, generation of interaction events and potential visualisation scenes [50]. Finally, the core layer includes classes exclusive to GATE, mainly the GATE virtual clock which similarly to its use in Geant4, is responsible for time management during simulations, and recording when hits occur. The second component of the development layer is the application layer. This component builds on the core layer, and is responsible for the modelling of specific objects and processes. For example, the core layer defines the base class of the volumes, then the application layer contains the classes which allow for modelling of certain volumes (eg boxes, cylinders) [75]. The classes present in this layer of the application are also extensions of the movement base class, and can create specified movements of translation, rotation and oscillations. This layer is open to expansion, with the potential for the development of new specific volumes and their movement. The final layer is the user layer, which utilises scripts to allow for users with no coding experience to run simulations. This is possible through the inner layers of GATE, with the development layer classes establishing all the C++ coding required [80]. So when the user wishes to create a geometry or source, all that is required is to generate it using a tree like scenario. First, the user calls GATE, and then the subset class for example the geometry or source. Each subset class will contain commands which are installed in the development layer, whether it be setting the length of the world or attaching an actor to a phantom to measure dose. The scripts, also known as macros, are ASCII text files (.mac files). Lines containing # are comments, however male and female components are commented out depending on which gender is selected. The macros are executed in a LINUX machine or through a GATE virtual machine, calling **GATE** followed by the name of the macros file.

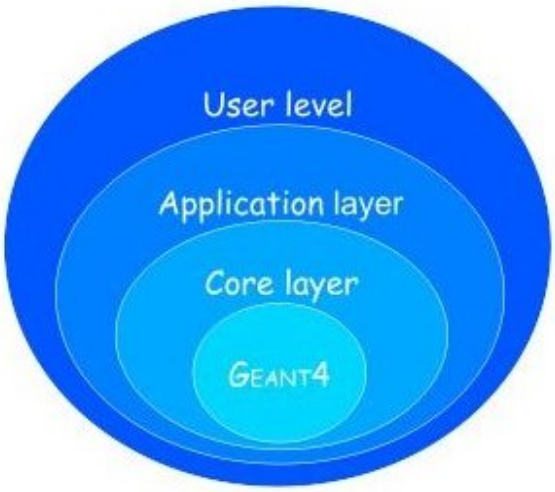

Figure 2.8: Structure of Gate [80]

Chapter 3

Method and Materials

3.1 Adult Voxel Reference Computational Phantoms

The ICRP since their 2007 publication, ICRP 103 [35], have been promoting the use of a voxel computational phantom for dosimetric reference data. This need for an updated reference computational male and female for voxel phantoms came as a result of the ICRP 89 publication, which updated the 'Basic Anatomical and Physiological Data for Use in Radiological Protection Reference Values' [36]. Publication 89 aimed to unify new information on reference anatomy and physiology which were last updated in 1975 [81]. At the time, the best methodology was the use of three-dimensional volume pixels (voxels) to define organs and tissues. The voxel phantoms were generated based on CT images of a male and female patients with physical characteristics similar to the reference male and female listed in ICRP 89 [36]. The CT images were adapted to fit the reference values given in the previous publication, which were then released as voxel phantoms in ICRP's 2009 publication (ICRP 110, 2009) [33]. Table 3.1 defines the computational and physical properties of both male and female phantoms. The ICRP 110 phantoms contain an additional slice of skin on the top and bottom of the phantom to ensure the phantom is wrapped in skin [33] (this is denoted in Table 3.1 by the additional two slices*). These skin voxels are included in this study, totalling 140 different organ tissues. The make up of these organ tissues are detailed in the ICRP 110 publication, including the mass, density and chemical makeup [33].

Scripts were developed in R statistical voxelised tool [82] to convert the ICRP 110 files into a MHD format image file and a material file to be inputted in GATE, Figure 3.1. To do this, the number of rows, columns and slices were defined from the annals. The matrix elements were filled with the organ tissue ID from the AF/AM.dat file (see Section 3.3), detailing where organ tissues sit in the matrix (on a voxel basis). Each organ is then generated from the organs.dat file, with the make up of each organ described in the media.dat file.

Properties	Male (AM)	Female (AF)
Height (cm)	176	163
Mass (kg)	73.0	60.0
Number of tissue voxels	1 946 375	3 886 020
Slice thickness (voxel height, mm)	8.0	4.84
Voxel in-plane resolution (mm)	2.137	1.775
Voxel volume (mm^3)	36.54	15.25
Number of columns (X)	254	299
Number of rows (Y)	127	137
Number of slices (Z)	220 (+2)*	346 (+2)*

Table 3.1: Main Characteristics of male and female reference computational phantoms [33]

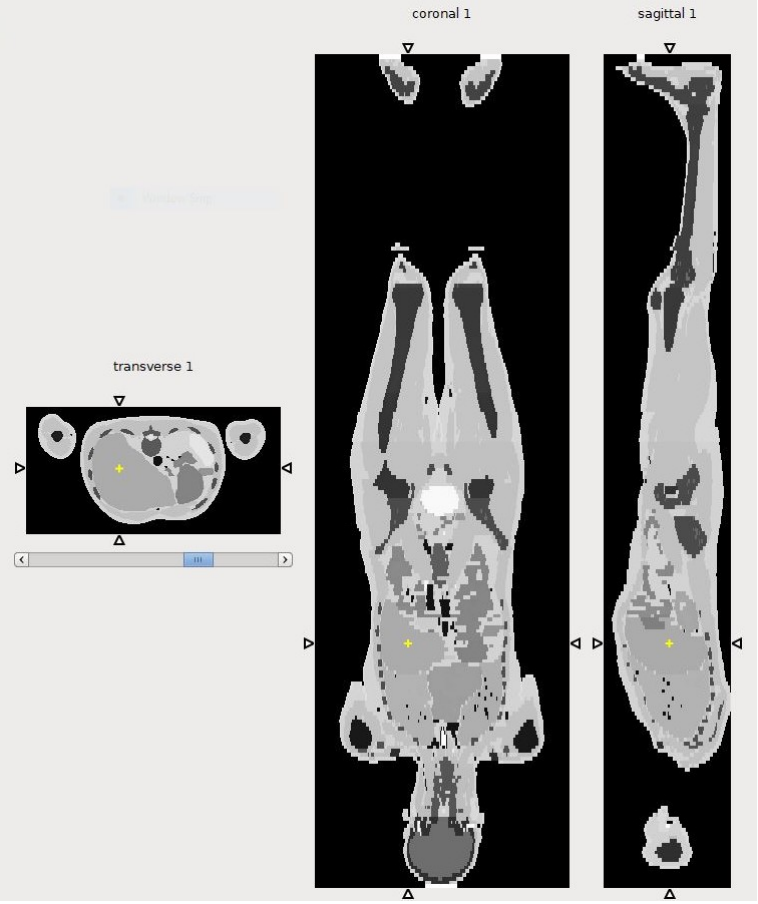

Figure 3.1: MHD image file of the AM ICRP 110 phantom with fiducial marker in liver as visualised using AMIDE [83]

3.2 Adult Mesh-type Reference Computational Phantoms

The development of the mesh reference phantoms is discussed in Section 1.3, with the ICRP 145 phantom visualisation observed in Figure 3.2 and Figure 3.3. To implement the phantom into GATE, first, the material databases had to be generated

for male and female phantoms. The chemical makeup of organs differ between male and female phantoms, and require separate databases. The additional file required to be generated is the RegionAttibuteTable, which labels each regionID as well as their colour (ratio of red, green and blue or rgb) for visualisation. The phantom requires no pre-processing and was constructed in GATE by calling the input files through macros.

In order to implement the ICRP 145 Mesh-type reference computational phantoms, various file formats were required. ICRP 145 utilises polygon mesh (PM) and tetrahedral mesh (TM) modelling developed from the previous voxelised reference phantom [43]. All files used were of the ASCII form, and the two used for the mesh phantom are the .node and .ele file extensions. The .node files contain the list of 3D points which are used to construct the polygons and tetrahedral shapes for the phantom construction. Each point described in the node has an x, y and z coordinate and is prescribed a boundary marker (either a vertex, edge or face). The next format is an .ele file which contains a list of tetrahedra to construct the phantom [40].

The tetrahedra call upon the material definitions (.mtl) file, a data directory required to construct the phantom. The .mtl file defines the colour of a material using three definitions. The K_a defines the ambient colour of the material, the K_b defines the diffuse colour and K_s defines the specular colour. These three definitions are made up of a ratio of red, green and blue (rgb), and define the colour of a material. For this project, ambient colour was chosen to represent the phantom illuminated by ambient light rather than direct light [40].

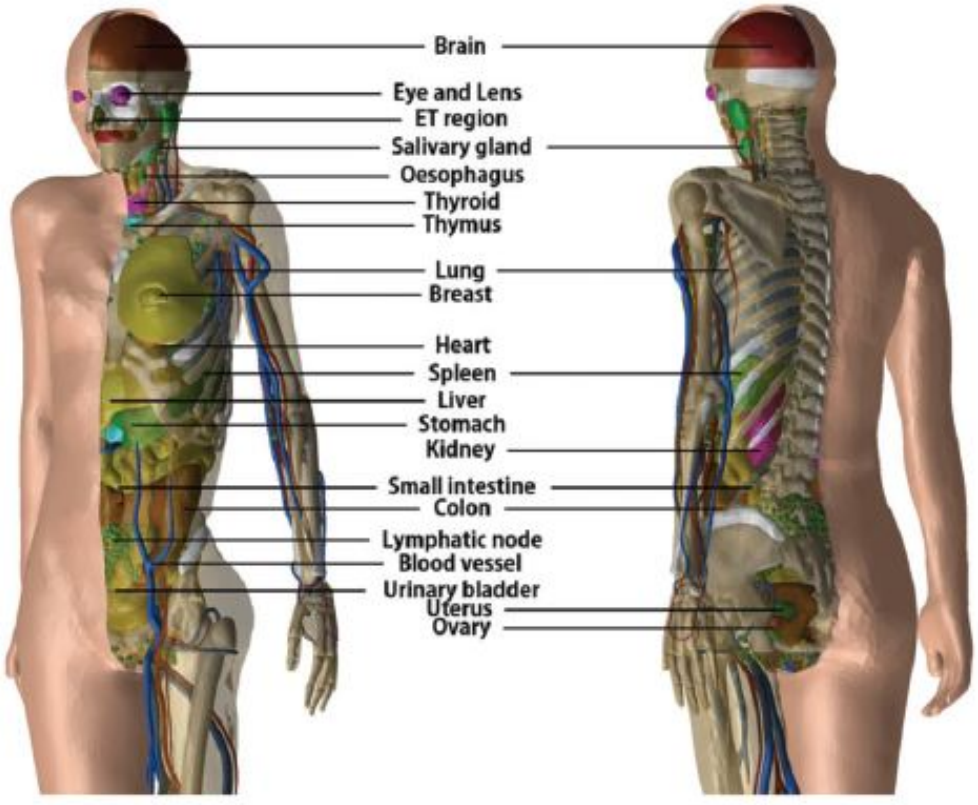

Figure 3.2: Adult Female Mesh-type Reference Computational Phantom [43]

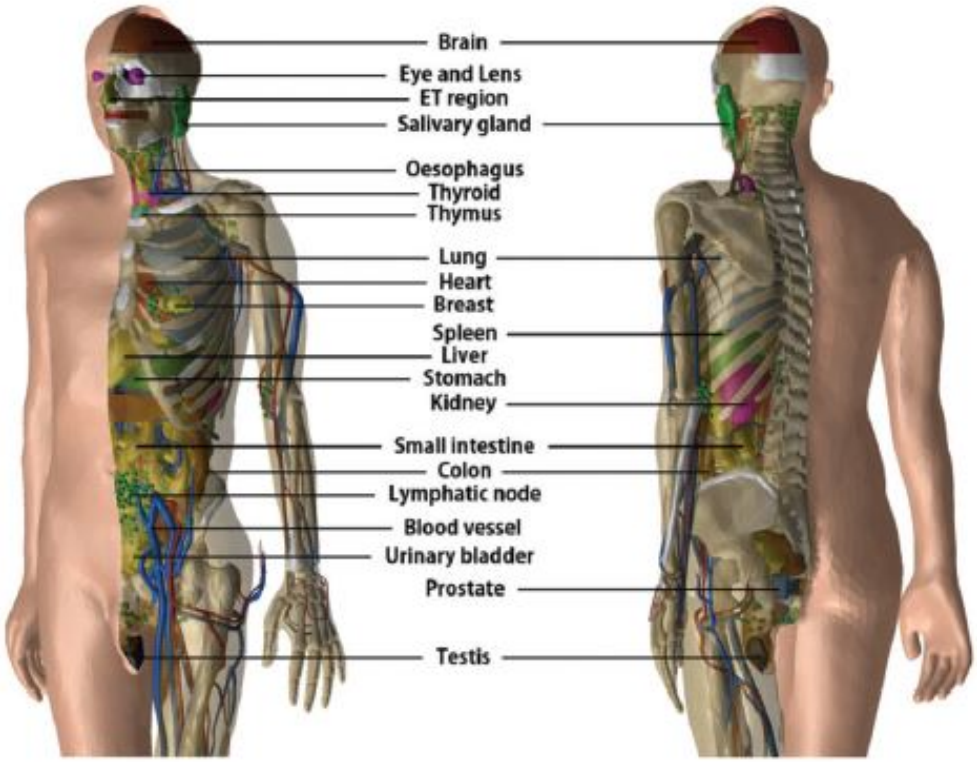

Figure 3.3: Adult Male Mesh-type Reference Computational Phantom [43]

3.3 Implementation of voxel phantom in GATE

ICRP 110 has attached supplemental material including;

- List of media and their elemental compositions (AF/AM_media.dat)
- List of skeleton sub-segmentation with composition of red bone marrow (RBM), yellow bone marrow (YBM) and bone (AF/AM_spongiosa.dat)
- List of Organs and tissues of the computational phantom, and associated organ ID/tissue number (AF/AM_organs.dat)
- List of Blood ratios within each media (AF/AM_blood.dat)
- File defining where each medium sits (matrix) (AF/AM.dat)

These files have been used to generate a materials database which GATE calls upon when generating the geometry. The database **ICRP110_materials.db** was generated using an Rscript and is generated from the above files . This material database was called in the world macros, and defines the chemical composition of any material used in the world as well as size ($9m^3$) (including phantom). Next, a phantom macro file was called, generating the phantom in the world. In order to utilise this method, a metaimage format was used (header.mhd and rawimage.raw). These files are generated using an Rscript, which takes the phantom data from the supplementary ICRP 110 files and generates the geometry files. The Geant4 nested

parametised method was used to create the navigation volume in Geant4. This method was utilised due to its efficiency in storing data [80]. The negative of using this method is the increased time required to run particles, as particles are required to stop at boundaries of parallelepipeds [75], causing the generation of a supplementary step [80]. Finally, the phantom had to be orientated within the world. The centre of the phantom was set to the centre of the world and was orientated along the Z axis (patient supine with superior components in positive Z direction). The Geant4 physics process utilised was the Emlivermore package, due to its accuracy at low energies (as discussed in the previous Section 2.4). For gamma's and electrons, the range cuts were set to 0.1mm within the phantom. A **detectors.mac** file contains all the relevant actors which collect data from the simulation runs. The **DoseByRegions** actor was used to collect the relevant data from the simulations. The **DoseByRegions** actor requires a second input in order to identify and define regions to collect information. By inputting the ICRP110_GATEgeometry.mhd file, the actor can identify each region and store the information. The actor outputs results as a text file and includes:

- ID number
- Volume (mm^3)
- Energy Deposited (MeV) in each region
- Standard Deviation of the Energy Deposited (MeV)
- Square root of the Energy Deposited
- Dose (Gy)
- Standard Deviation of the Dose (Gy)
- Square root of the Dose
- Number of hits in the region (each time primary or secondary particle makes a step, whether energy deposition occurs or not)
- Number of event hits in the region

The source was implemented in separate source macros for different radionuclides. Each source macros contained a histogram and describes the energy and frequency of emissions, as well as the intensity of different emission types. The source was defined as 'Volume' to generate a homogeneous and isotropic emission. The entire decay scheme was simulated. Auger electron's were not included in this simulation. There was no minimum threshold applied for X-ray/photon emission. The energy histograms were taken from the ICRP 107 annals, which contains the nuclear decay data for dosimetric calculations [31]. In this publication the energies and yields of radioisotopes are published and organised into separate files for different decay methods. The ICRP-07.BET file was used for information on beta emitters and the ICRP-07.RAD file was used for all other decay methods, mainly emission of photons. This includes the entire decay chain for beta and gamma emission. The source was classified as a GEANT4 general particle source (GPS), with its energy, shape, dimension and position begin defined in the macro. Finally, the entire world

was visualised (using either DAWN or OpenGL visualisation tools). DAWN was included in the GATE installation, however to use OpenGL it must be included in the Geant4 installation.

3.4 Implementation of mesh phantom in GATE

The ICRP 145 publication are supported with the following supplementary materials for both male and female mesh phantoms [43]. The data files for the tetrahedral mesh (TM) MRCPs are defined in data files of NODE and ELE format files. The NODE-formatted files have the list of nodes which the TM phantoms are composed of. This is accompanied by the ELE-formatted files which have the list of tetrahedrons. These files work in unison, as each tetrahedron is described by four node IDs listed in the NODE-format file [43]. The following files accompany the NODE and ELE files of the ICRP 145 publication which describe the material of the phantom:

- Lists of the media, elemental compositions and densities (media.dat)
- The mass ratios of bone constituents in the bone sites (bone.dat)
- The mass ratios of blood in various body tissues (blood.dat)
- PDF for visualisation

A similar methodology is followed to generate the mesh phantom in GATE: the material database was used as per the ICRP 110 phantom was to create the world and define the materials which are used to implement the phantom. To create the phantom in the world, the .ele file and RegionAttributeTable (includes region number, name of material, and rgb discussed in Section 3.2) are used. The phantom is again set to the centre of the world and is orientated along the Z axis (patient supine with superior components in positive Z direction). For data collection in tetrahedral mesh geometries, the **TetMeshDose** actor was used. This actor records:

- Tetrahedron-ID
- Volume (cm^3)
- Density of Tetrahedron material (g cm^{-3}
- Region Marker
- Relative Uncertainty
- Dose (Gy)

Similarly to **ICRP110.mac**, the **ICRP145.mac** can be broken down into all its separate components.

3.5 GATE run parameters

Initial simulations of low particle counts were run on an Intel i7-6700 CPU operating at 3.40GHz to ensure geometries (phantom and source) were correct. GATE version 9.1 with Geant4 version 10.6.3 were utilised. 10 million particles were simulated using the Geant4 Emlivermore physics package for each scenario. These are for the three radionuclides used; Holmium-166, Lutetium-177 and Yttrium-90, for the four phantoms; ICRP 110 (male and female) and ICRP 145 (male and female), and the four spherical lesion diameters; 0.1cm, 0.5cm, 1cm and 3cm.

3.6 Determination of S-values for ICRP 110 and ICRP 145 phantoms

The voxel and mesh phantoms were generated in GATE as described above. The phantoms were placed in the centre of the world volume, with the phantoms laying supine along the Z axis (superior anatomy in positive Z direction). The ICRP 145 Adult Female (AF) phantom is shown in Figure 3.4, with the positioning within the world used for all phantoms. The red sphere within the patient is a 3cm diameter Ho-166 sphere, located within the liver. The positioning of the lesion was determined using the ICRP 110 geometry image, generated for the construction of the ICRP 110 phantom within GATE. Preliminary runs were conducted with 3 million particles to confirm the placement of the source in the phantoms. As the range of beta emission for Holmium-166 is a maximum of 8.7mm, the largest amount of energy deposited was within the source organ, confirming the placement of the lesion. The simulations were repeated with 10 million particles per simulation for each scenario. S-values for the liver, pancreas, gall bladder, small intestine, left and right lung and the stomach were estimated. The simulations aimed to achieve a coefficient of variation within the source organ of less than 0.5. The coefficient of variation was determined to characterise the uncertainties in the Monte Carlo simulations run. A uniform distribution of three radionuclides: Yttrium-90, Holmium-166 and Lutetium-177 were all implemented into the male and female phantoms (voxel and mesh phantoms). Spherical sources were placed in the liver, and were simulated for four different sphere diameters; 0.1cm, 0.5cm, 1cm and 3cm. The radionuclides generated from the ICRP 107 include beta and gamma emission, hence the S-values determined include both emission methods. The centre of the lesion remained constant throughout the simulations sitting in a central position of the liver. The mass of each region was determined by multiplying the volume of a region by the density of the region. The energy deposited in each region which is recorded by the **DoseByRegion** actor, is divided by the mass calculated (J/kg), which is equivalent to the units for dose (Gy). This was used to determine the S-values, by dividing the dose by the number of particles (Gy Bq^{-1} s^{-1}). The common units for S-values are mGy MBq^{-1} s^{-1}, so unit conversion was conducted. For the ICRP 145 phantom, the **TetMeshDose** actor was utilised. The output of the file includes the tetrahedron ID, dose in each tetrahedron, uncertainties and the volume of each tetrahedron. In each tetrahedron, dose per tetrahedron was converted to energy per tetrahedron. The mass of each tetrahedron was then calculated by multiplying its volume by the density listed in the ICRP 145 annals. The dose per region was calculated by

summing each tetrahedron within a region and dividing by the mass sum of all tetrahedron within the volume. A similar calculation was conducted for the uncertainty per region. The S-values were again determined by dividing the dose in a region by the number of particles, and conducting unit conversions.

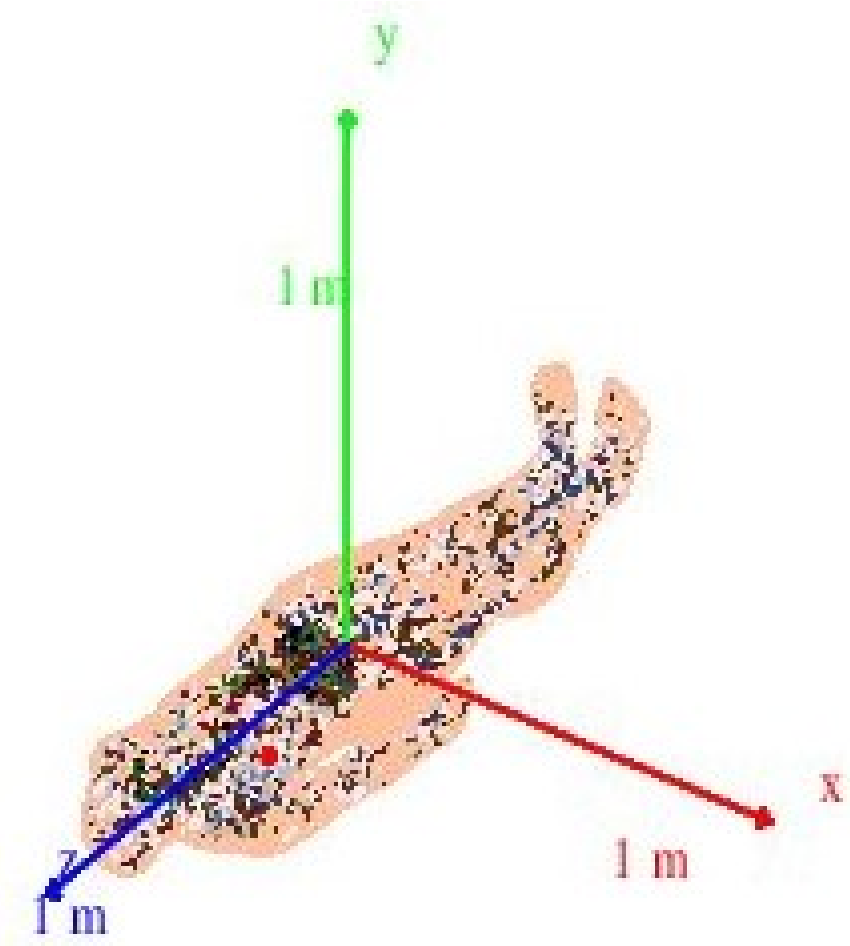

Figure 3.4: AF ICRP 145 mesh phantom world volume placement, red 3cm diameter ^{166}Ho source, visualised in DAWN. The dots in the phantom show the different materials as described in the RegionAttributeTable

S-values estimated for the ICRP 110 and ICRP 145 phantoms, for the use of Yttrium-90, Holmium-166 and Lutetium-177 in spherical sources placed in the liver are shown in the following chapter. Each plot presents the three radionuclides with four different spherical lesions (0.1, 0.5, 1 and 3cm diameter) for the ICRP 110 female, ICRP 110 male, ICRP 145 female and ICRP 145 male phantoms. The centre of the lesion remained constant throughout the simulations sitting in a central position of the liver. Using the confine function, the source remained within the liver volume. Each organ has its mass calculated from the simulation data. The volume of each voxel/tetrahedron is multiplied by the density of the region of interest to determine its mass. This increases the accuracy of the simulation, as by not using the weight of each region given in the ICRP annals the weight matches that used in the simulation exactly. The results presented for organs outside the liver have large statistical uncertainties due to the small number of particles interacting in the volume. This is due to the relative low abundance of γ-emission, when present, and to the short range of β-emission. Uncertainties on the S-values are presented in Appendix A as well as all the S-values for all simulations run. Table A.1 has all S-values for the ICRP 110 female phantom, Table A.2 the ICRP 110 male, Table A.3 the ICRP 145 female and Table A.4 the ICRP 145 male phantom. This comprehensive set of data includes the S-values as well as coefficient of variation for each lesion diameter and radionuclide, with the previous plots a visual representation of this data. This data also includes the small intestine and stomach which have not been visualised.

Chapter 4

Results

Section 4.1 show the S-values for Liver ← Lesion for the four phantoms. Each plot contains the three radionuclides and the four different lesion diameters. This estimation includes the contribution to the healthy liver volume as well as the self-contribution within the lesion volume. Section 4.2 - 4.5 show the S-values for the pancreas, gallbladder, left lung and right lung. No error bars have been included in the liver plots as error bars would not be visible. Error bars have not been included in the other organ plots and rather have been attached in Appendix A as Coefficient of Variations.

4.1 S-values for Liver ← Lesion

Figures 4.1 - 4.4 show the S-values calculated in the whole liver with a lesion within the liver. This value includes the dose recorded within the lesion, so the S-value represents the entire organ. Figures 4.1 - 4.4 show that the S-value determined within the liver was greatest for the Lutetium-177 isotope and was highest for the female reference phantoms. The S-values for Yttrium-90 are the lowest for the three radioisotopes. Its greater energy emission during beta decay allows electrons to travel further before reaching the end of their range. The S-values determined are larger in females due to the difference in organ mass. In the ICRP 145 annals, males are listed of having a liver mass of 2.36kg whilst females have a liver mass of 1.81kg. As the mass is larger in males, the dose value recorded (J/kg) will be smaller, leading to a smaller S-value. The S-values determined for the ICRP 110 phantoms are also larger, due to the ICRP 145 phantoms more accurately accounting for blood in the organ. The ICRP 110 annals have the male liver listed as 1.8kg and the female as 1.4kg, and thus will increase the dose and larger S-values will result.

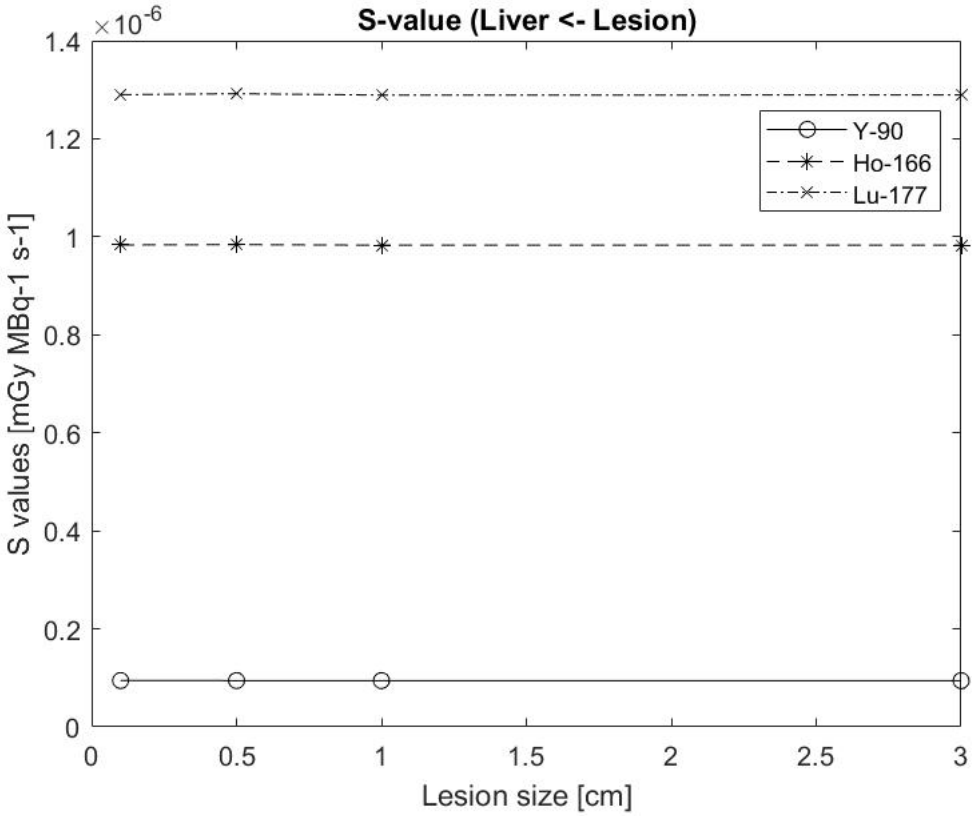

Figure 4.1: (Liver ← Lesion) S-values (mGy $MBq^{-1}s^{-1}$) for Y-90, Ho-166 and Lu-177 in the ICRP 110 Female phantom

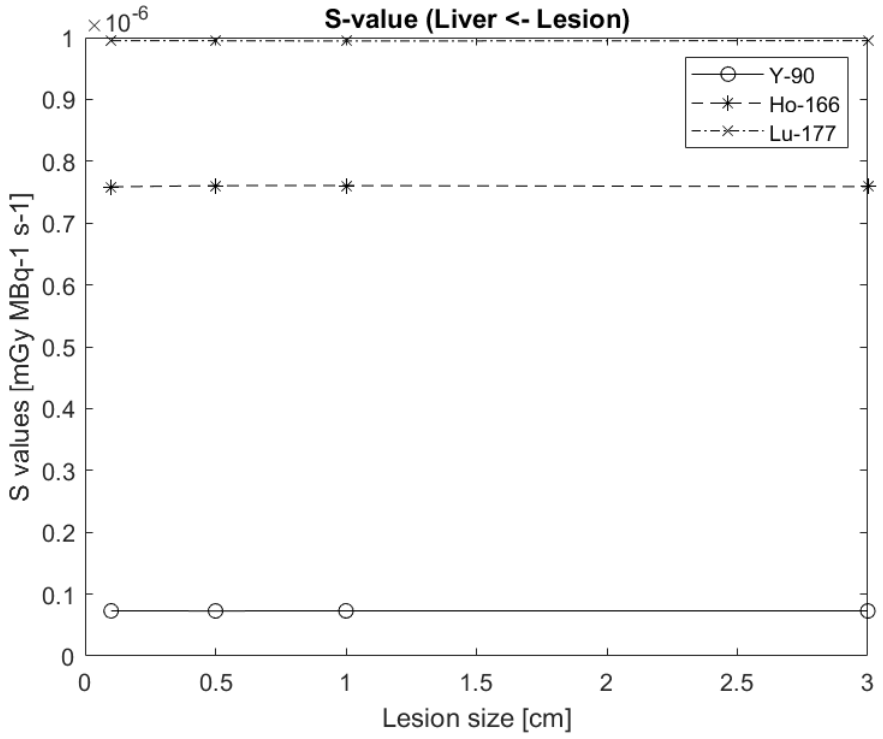

Figure 4.2: (Liver ← Lesion) S-values (mGy $MBq^{-1}s^{-1}$) for Y-90, Ho-166 and Lu-177 in the ICRP 110 Male phantom

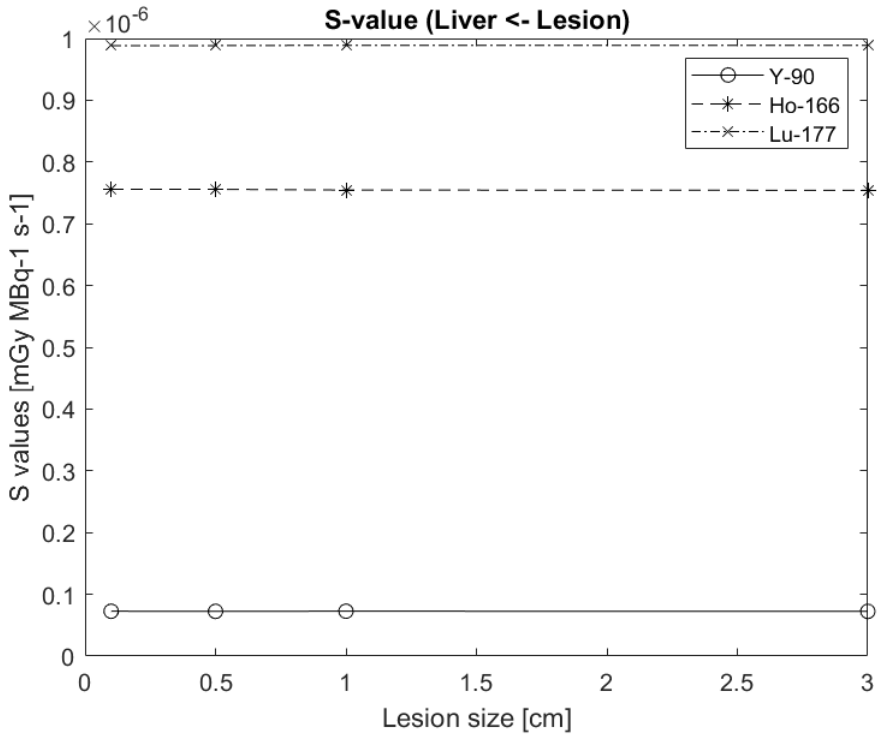

Figure 4.3: (Liver ← Lesion) S-values (mGy $MBq^{-1}s^{-1}$) for Y-90, Ho-166 and Lu-177 in the ICRP 145 Female phantom

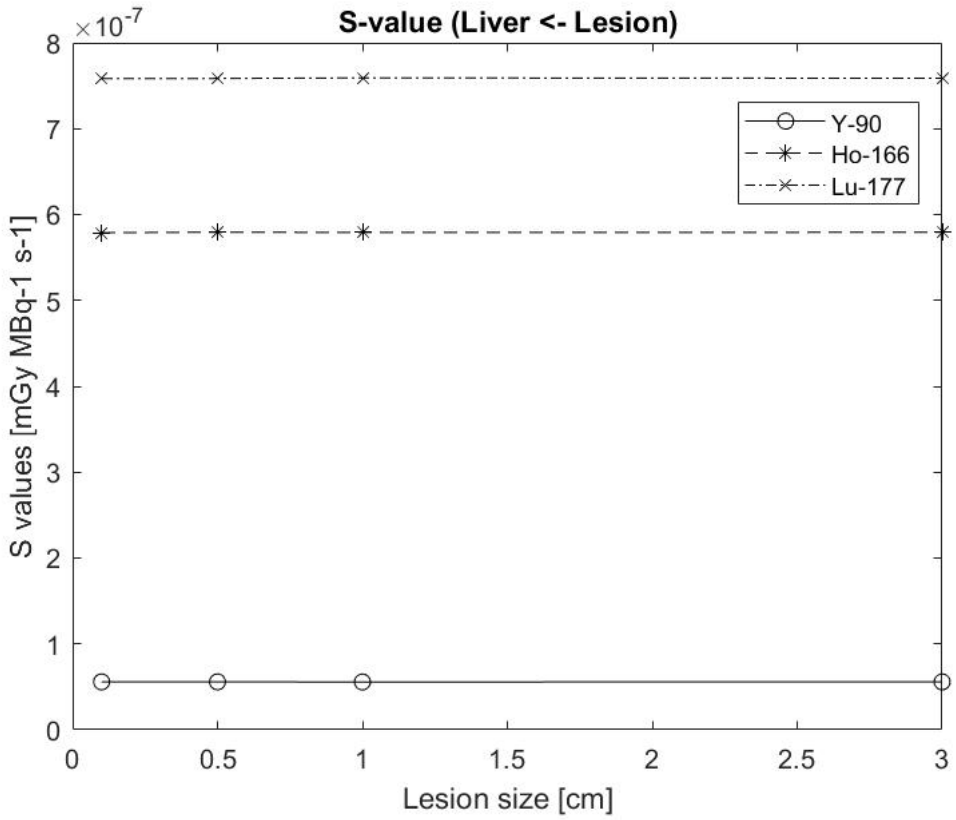

Figure 4.4: (Liver ← Lesion) S-values (mGy $MBq^{-1}s^{-1}$) for Y-90, Ho-166 and Lu-177 in the ICRP 145 Male phantom

4.2 S-values for Pancreas ← Lesion

The pancreas sits in a medially inferior position to the main lobe of the liver, with part of the small intestine sitting between the pancreas and the liver. Figures 4.5 - 4.8 show the S-values calculated for the pancreas due to activity in spherical lesions in the liver. As the lesion size increases the S-values determined in target organs in close proximity to the liver will increase. This is observed in Figures 4.6, 4.7 and 4.8, where the S-values calculated for Yttrium-90 increases significantly as for the 3cm diameter lesion. Y-90 is expected to have the largest S-values located outside the source organ due to its larger maximum and average range for beta particles. This trend is not followed in Figure 4.5, this is due to large uncertainty due to low number of hits in the target. It is also expected the S-values increase as the lesion size increases, however this is not demonstrated for the 0.5cm and 1cm diameter lesions.

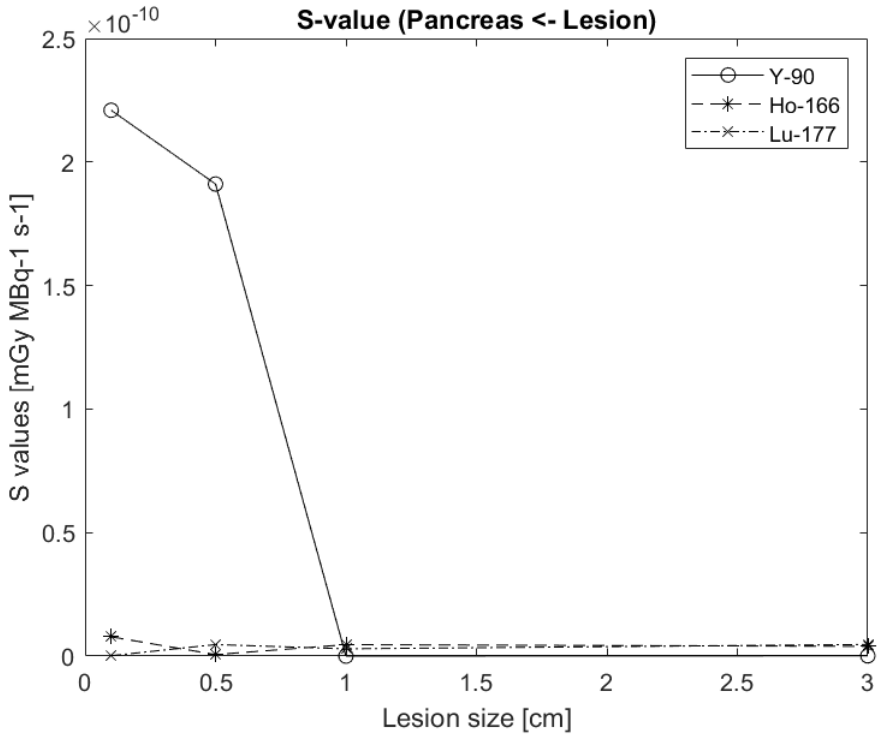

Figure 4.5: (Pancreas ← Lesion) S-values (mGy $MBq^{-1}s^{-1}$) for Y-90, Ho-166 and Lu-177 in the ICRP 110 Female phantom

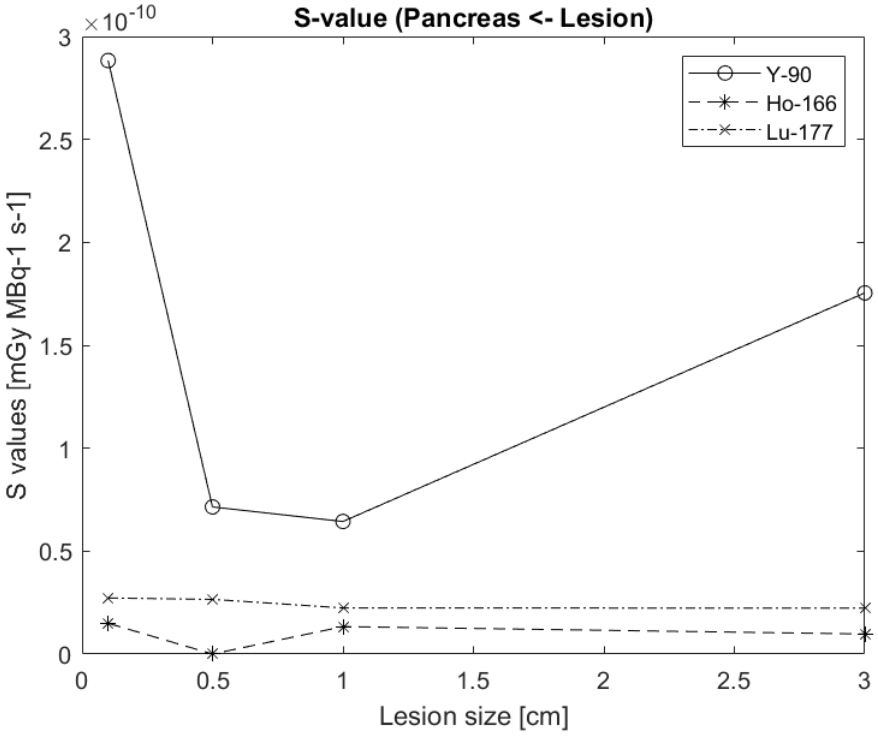

Figure 4.6: (Pancreas ← Lesion) S-values (mGy $MBq^{-1}s^{-1}$) for Y-90, Ho-166 and Lu-177 in the ICRP 110 Male phantom

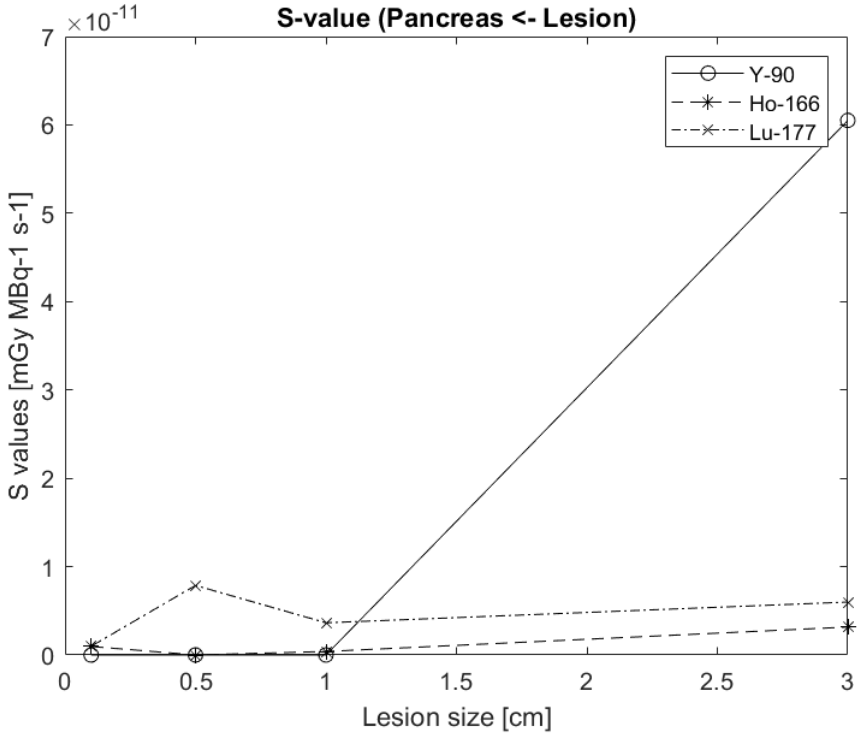

Figure 4.7: (Pancreas ← Lesion) S-values (mGy $MBq^{-1}s^{-1}$) for Y-90, Ho-166 and Lu-177 in the ICRP 145 Female phantom

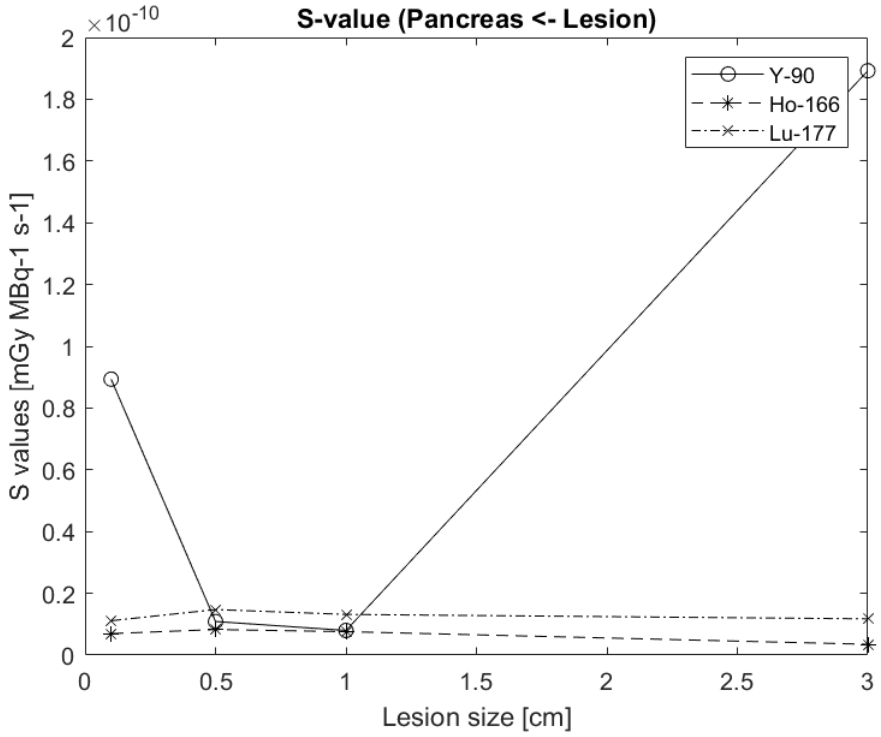

Figure 4.8: (Pancreas ← Lesion) S-values (mGy $MBq^{-1}s^{-1}$) for Y-90, Ho-166 and Lu-177 in the ICRP 145 Male phantom

4.3 S-values for Gallbladder ← Lesion

The gallbladder sits directly below the liver, flush to the surface of the liver. Figures 4.9 - 4.12 depict the S-values determined for the 3 radionuclides in the gallbladder due to the lesion within the liver. The results include the dose to the gallbladder wall, as well as its contents, as provided in the ICRP 110 and 145 annals. Due to the proximity to the liver, the gallbladder has the second largest S-value across the target organs discussed, reaching a maximum S-value of 2.588×10^{-8} (mGy $MBq^{-1}s^{-1}$) in the ICRP 110 Male phantom for Y-90. The figures also show a larger degree of variation in S-values for Ho-166 and Lu-177 compared to other target organs discussed. As the range of these radioisotopes is shorter in tissue, they will deposit a smaller amount of energy as the target is further from the lesion. Figure 4.10 shows the trend which best follows the expected behaviour of the simulations. The linear trend will continue as the lesion size grows, with the largest lesion size depositing the largest energy onto the target organ. An anomaly of these figures (4.9, 4.11 and 4.12) is the reduction of S-value for 1cm source size, easily identifiable for the Y-90 source. Low particle counts create a larger statistical uncertainty, which is further amplified in target organs outside the source organ.

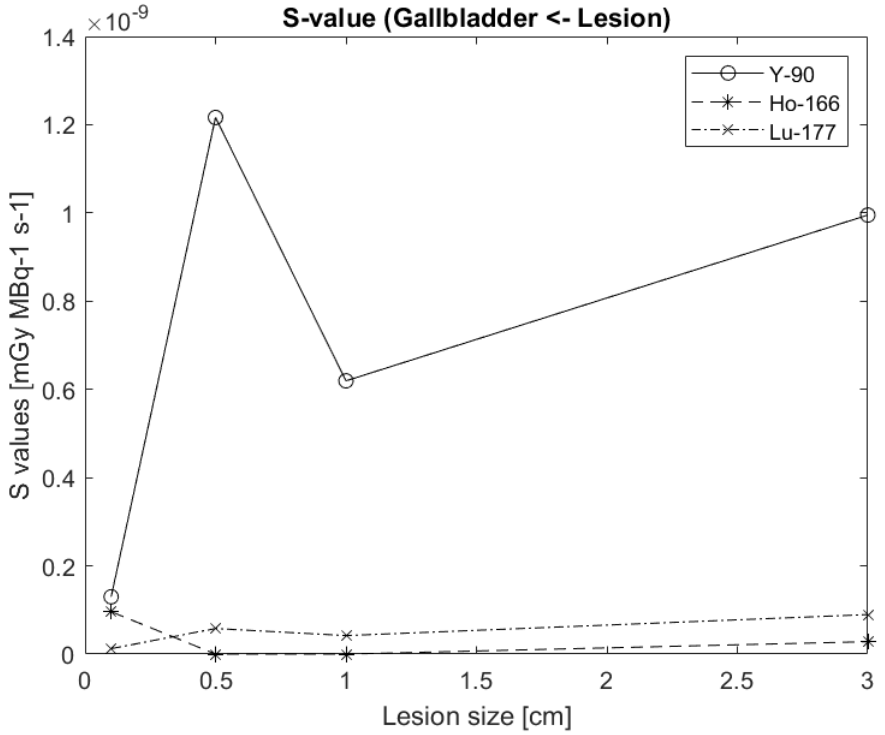

Figure 4.9: (Gallbladder ← Lesion) S-values (mGy $MBq^{-1}s^{-1}$) for Y-90, Ho-166 and Lu-177 in the ICRP 110 Female phantom

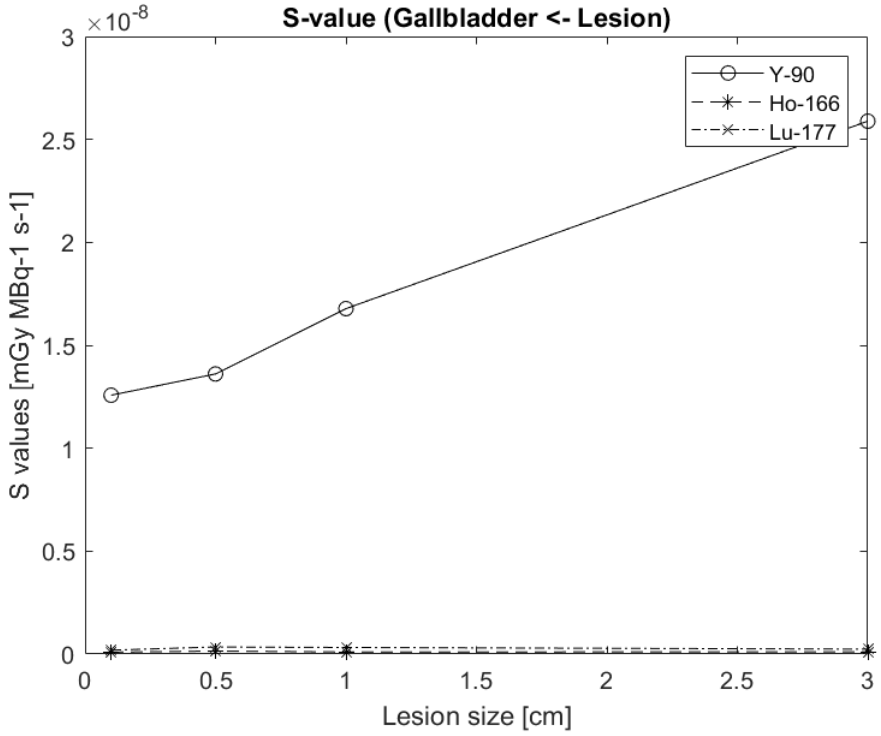

Figure 4.10: (Gallbladder ← Lesion) S-values (mGy $MBq^{-1}s^{-1}$) for Y-90, Ho-166 and Lu-177 in the ICRP 110 Male phantom

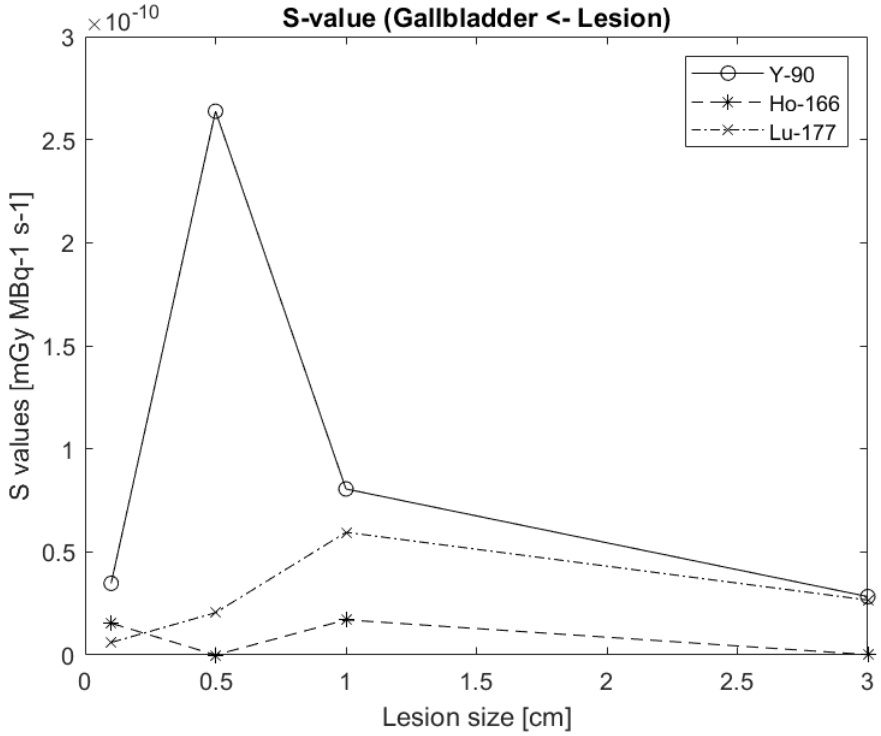

Figure 4.11: (Gallbladder ← Lesion) S-values (mGy $MBq^{-1}s^{-1}$) for Y-90, Ho-166 and Lu-177 in the ICRP 145 Female phantom

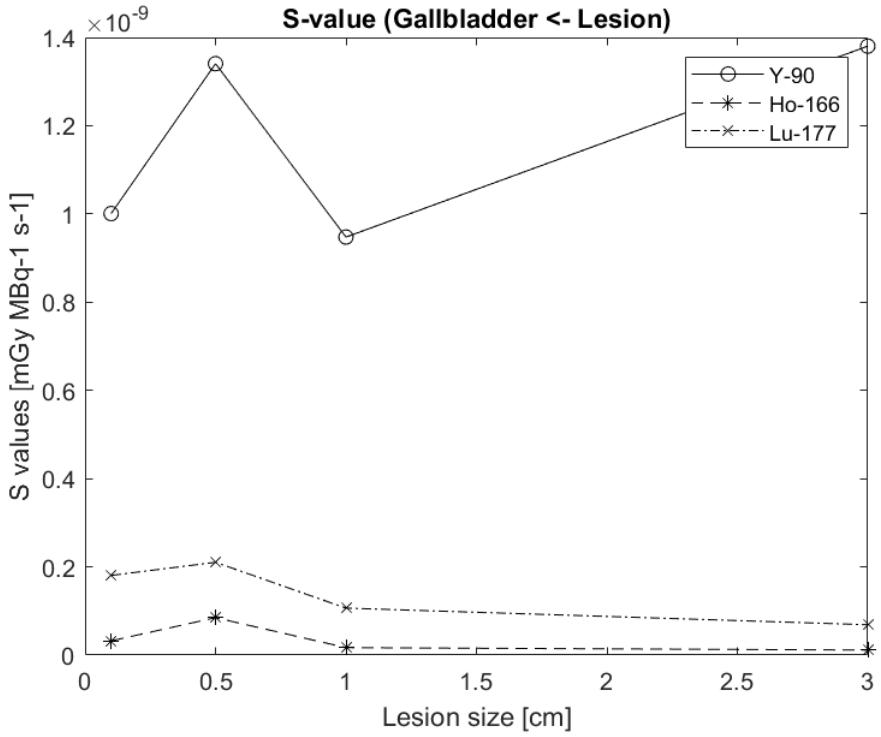

Figure 4.12: (Gallbladder ← Lesion) S-values (mGy $MBq^{-1}s^{-1}$) for Y-90, Ho-166 and Lu-177 in the ICRP 145 Male phantom

4.4 S-values for Left lung ← Lesion

The left lung sits in a superior and opposing side of the body with respect to the right lobe of the liver. Due to this increased distance from the liver lesion, the S-values calculated are smaller relative to the pancreas and gallbladder. S-values calculated had a maximum value of 4.741×10^{-11} (mGy $MBq^{-1}s^{-1}$), however all values possessed a large uncertainty (minimum coefficient of variation of 44.92). Due to these uncertainties, it is difficult to determine any trends which occur for the three radionuclides. There are small variations occurring for the Holmium-166 and Lutetium-177 sources, but are small relative to the changes in Yttrium-90. Some anomalies are present in the phantoms presented (Figure 4.13, 4.15, 4.16) which have the largest S-value for three smaller source diameters (0.1cm, 0.5cm, 1cm). There are also some simulations where zero hits were recorded in the left lung.

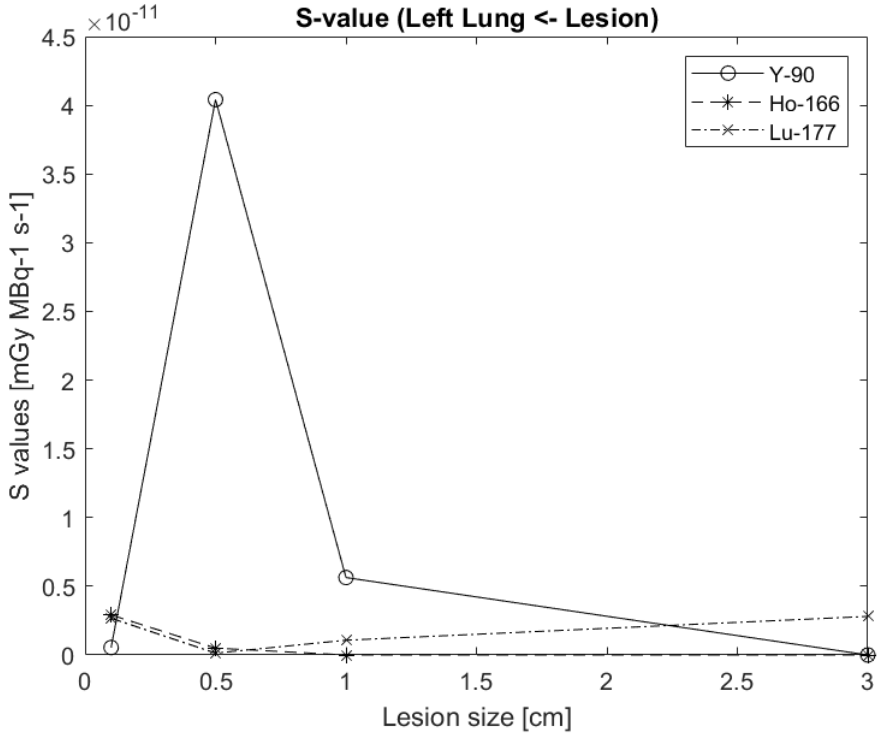

Figure 4.13: (Left lung ← Lesion) S-values (mGy $MBq^{-1}s^{-1}$) for Y-90, Ho-166 and Lu-177 in the ICRP 110 Female phantom

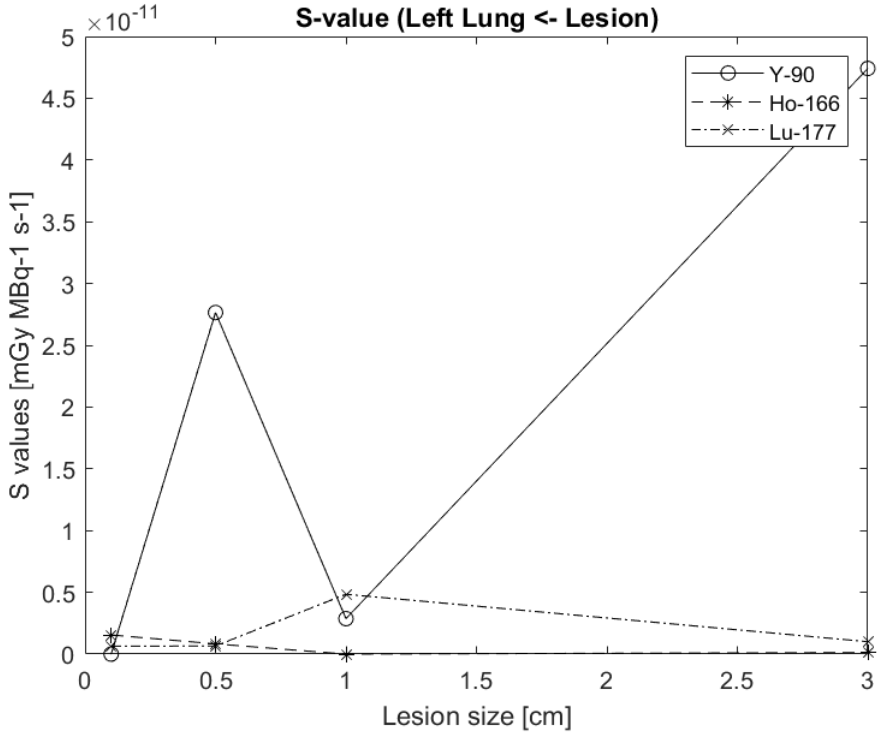

Figure 4.14: (Left lung ← Lesion) S-values (mGy $MBq^{-1}s^{-1}$) for Y-90, Ho-166 and Lu-177 in the ICRP 110 Male phantom

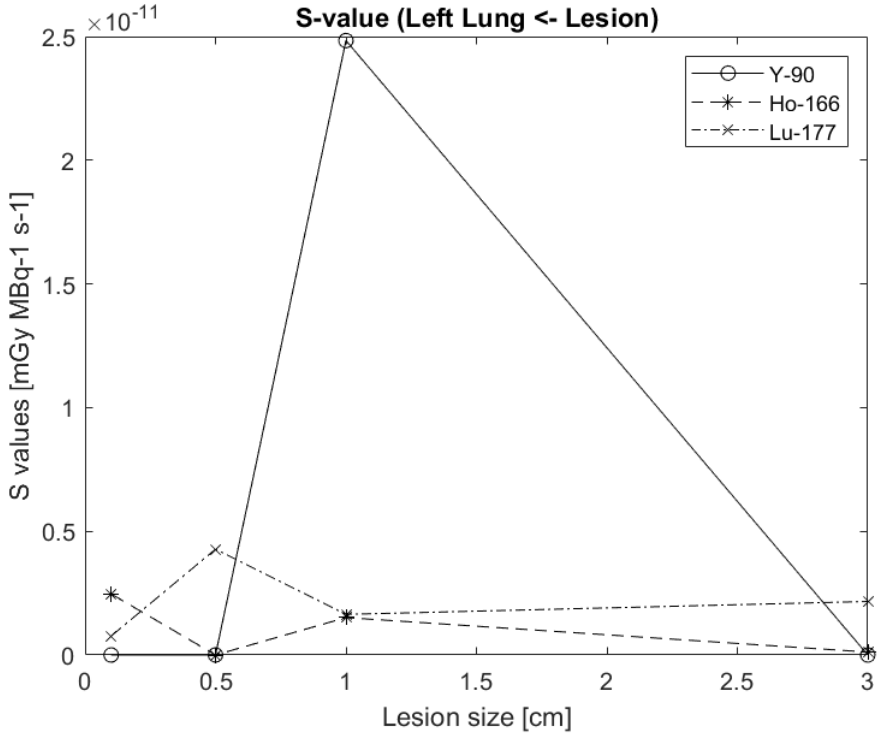

Figure 4.15: (Left lung ← Lesion) S-values (mGy $MBq^{-1}s^{-1}$) for Y-90, Ho-166 and Lu-177 in the ICRP 145 Female phantom

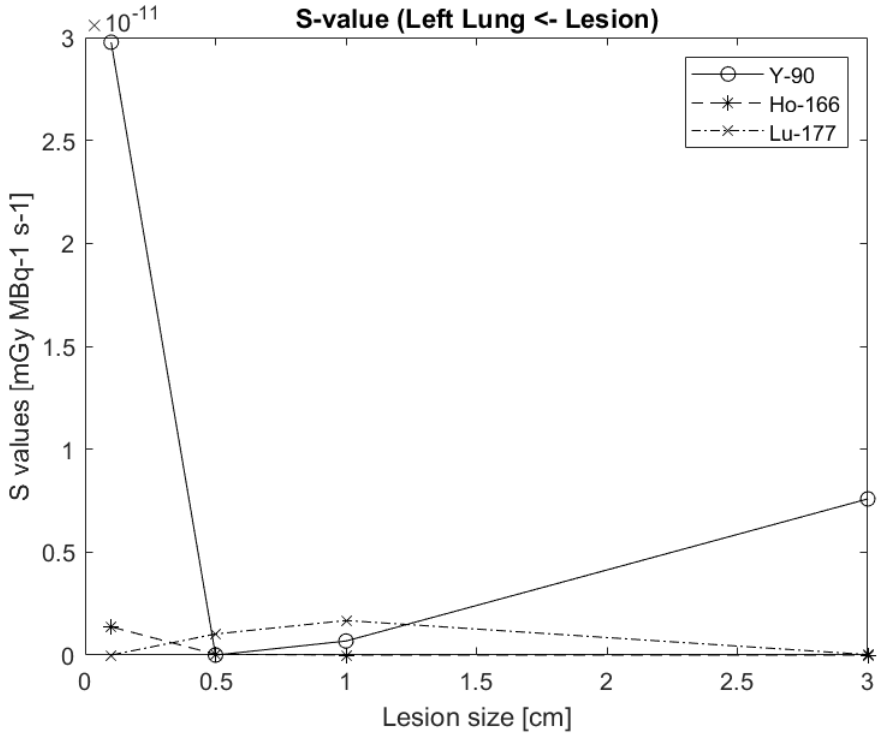

Figure 4.16: (Left lung ← Lesion) S-values (mGy $MBq^{-1}s^{-1}$) for Y-90, Ho-166 and Lu-177 in the ICRP 145 Male phantom

4.5 S-values for Right lung ← Lesion

The right lung sits superior to the right lobe of the liver and has a larger amount of energy incident on it than the left lung due to its proximity to the liver. The S-values recorded are larger on average, and has a maximum S-value of 1.295×10^{-9} (mGy $MBq^{-1}s^{-1}$) in the ICRP 110 Female phantom for Y-90. Figure 4.20 better displays the changes in S-values for Ho-166 and Lu-177, with smaller variations in S-values (less than 1×10^{-11}) observable. From this figure it is understood that overall changes in the S-value for target organs have a small change for Ho-166 and Lu-177 radionuclides. This is due to their short range in soft tissue, and identifies that lesion size has a smaller impact on S-value variation.

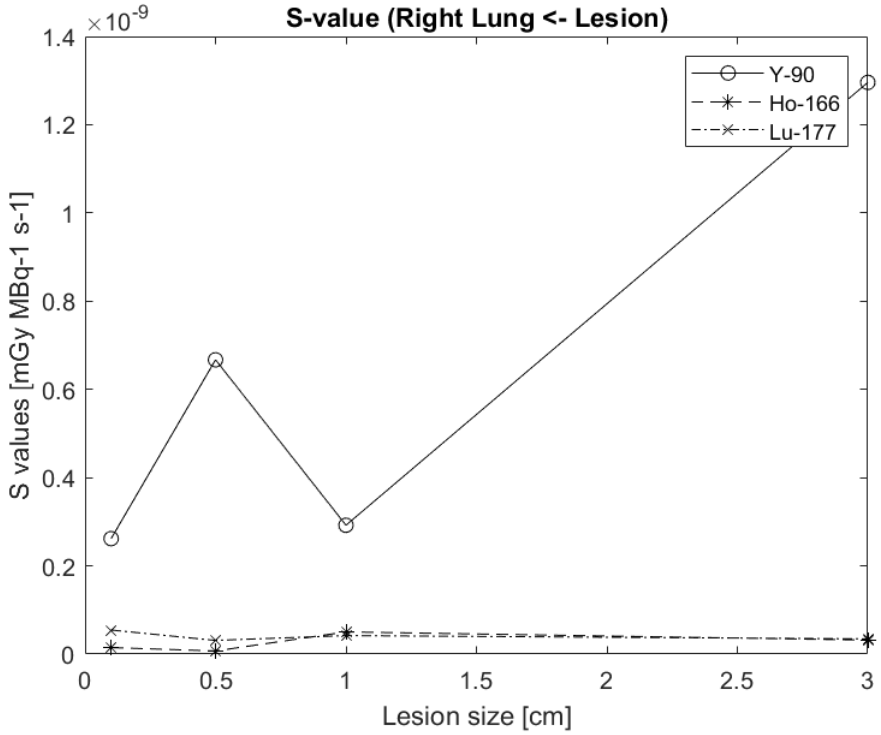

Figure 4.17: (Right lung ← Lesion) S-values (mGy $MBq^{-1}s^{-1}$) for Y-90, Ho-166 and Lu-177 in the ICRP 110 Female phantom

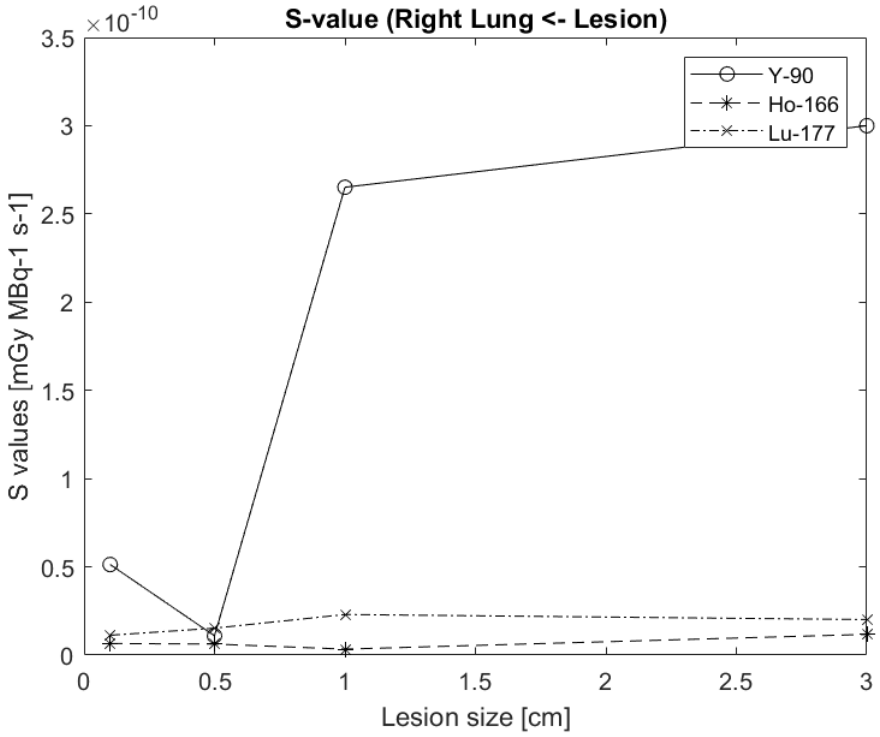

Figure 4.18: (Right lung ← Lesion) S-values (mGy $MBq^{-1}s^{-1}$) for Y-90, Ho-166 and Lu-177 in the ICRP 110 Male phantom

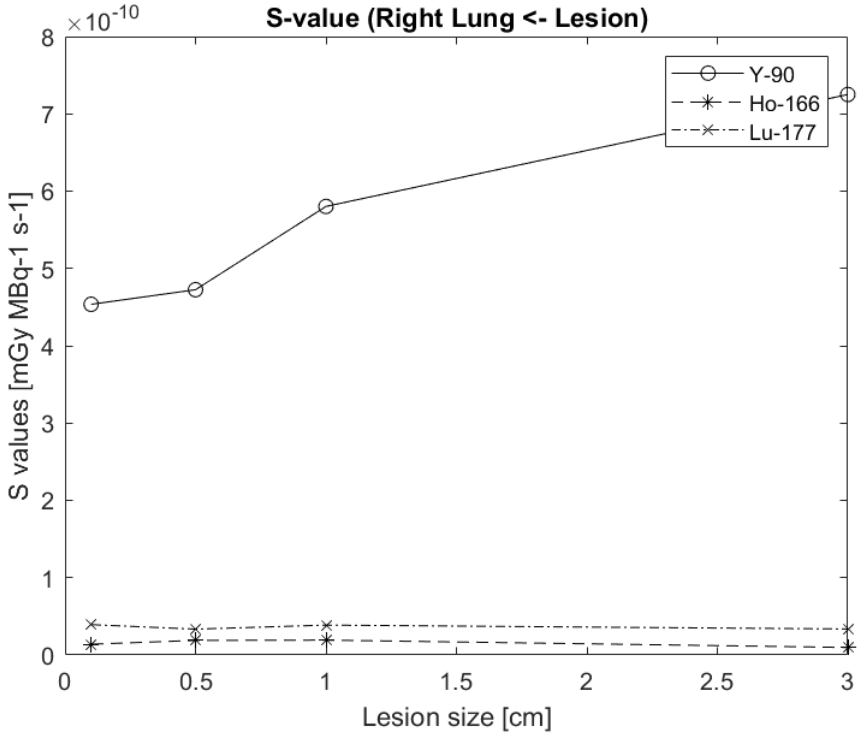

Figure 4.19: (Right lung ← Lesion) S-values (mGy $MBq^{-1}s^{-1}$) for Y-90, Ho-166 and Lu-177 in the ICRP 145 Male phantom

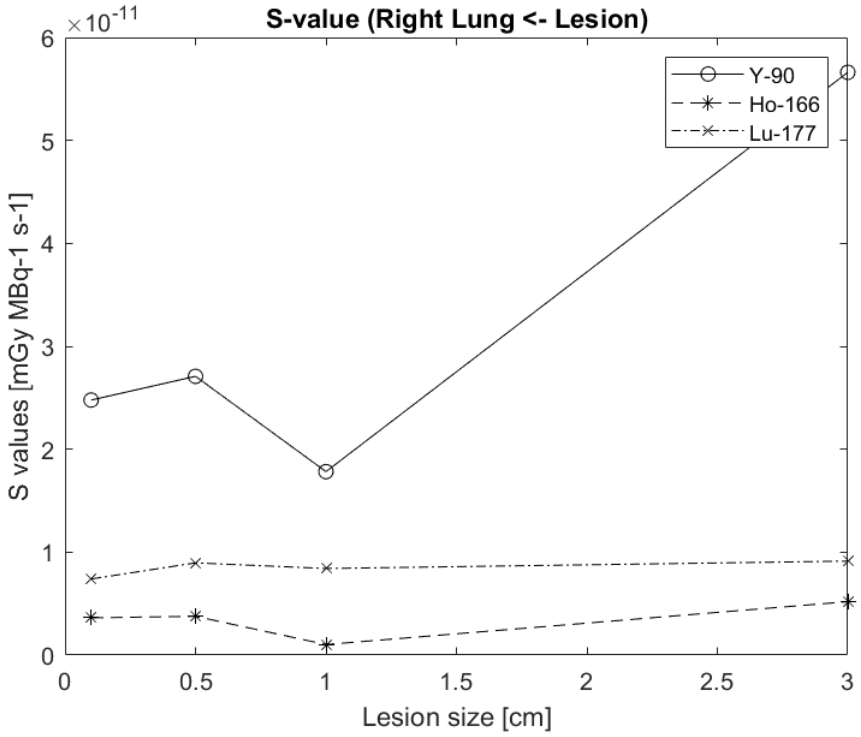

Figure 4.20: (Right lung ← Lesion) S-values (mGy $MBq^{-1}s^{-1}$) for Y-90, Ho-166 and Lu-177 in the ICRP 145 Male phantom

4.6 S-values for Left Kidney ← Lesion

The left kidney sits inferior and on the opposing side to the main liver lobe, so a smaller dose deposition in the organ is expected due to the short range of the beta emitters tested. This increased distance to the target organ and the small number of particles simulated also present the issue of poor hit counts, with some simulations having zero hits. Y-90 has the largest beta energy emitted and therefore has the largest beta emission range through soft tissue. However, when observing Figures 4.23 and 4.24 the Lutetium-177 radionuclide is depositing the largest amount of dose in the target region. This is most likely due to the poor statistics of the runs and will most likely be rectified in further runs. Figure 4.21 follows the expected trend, where Yttrium-90 deposits the largest amount of dose in the target organ, with the energy deposited increasing as the lesion size increases.

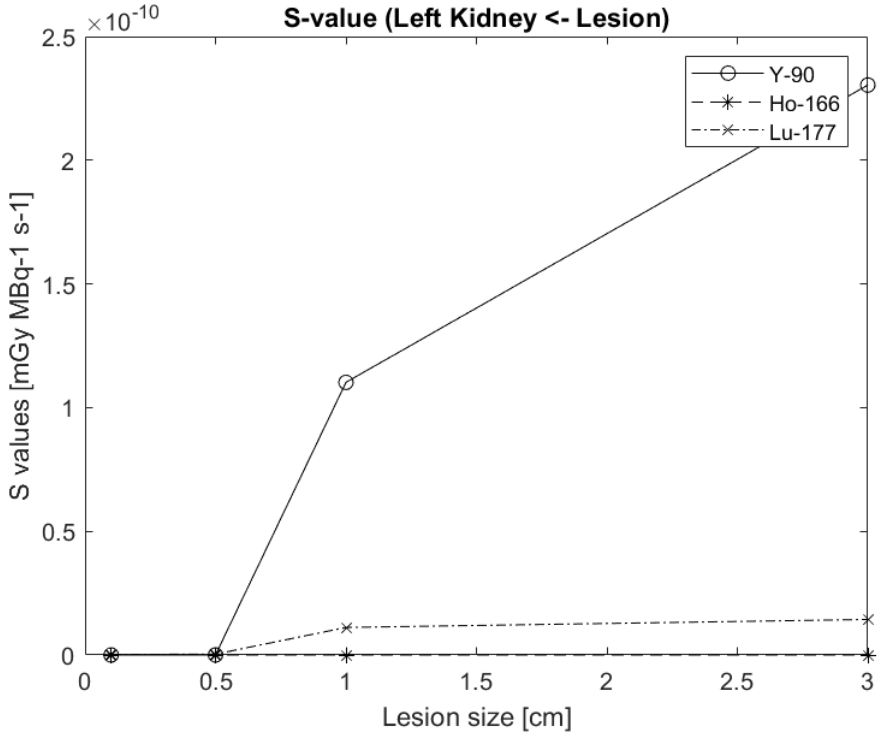

Figure 4.21: (Left Kidney ← Lesion) S-values (mGy $MBq^{-1}s^{-1}$) for Y-90, Ho-166 and Lu-177 in the ICRP 110 Female phantom

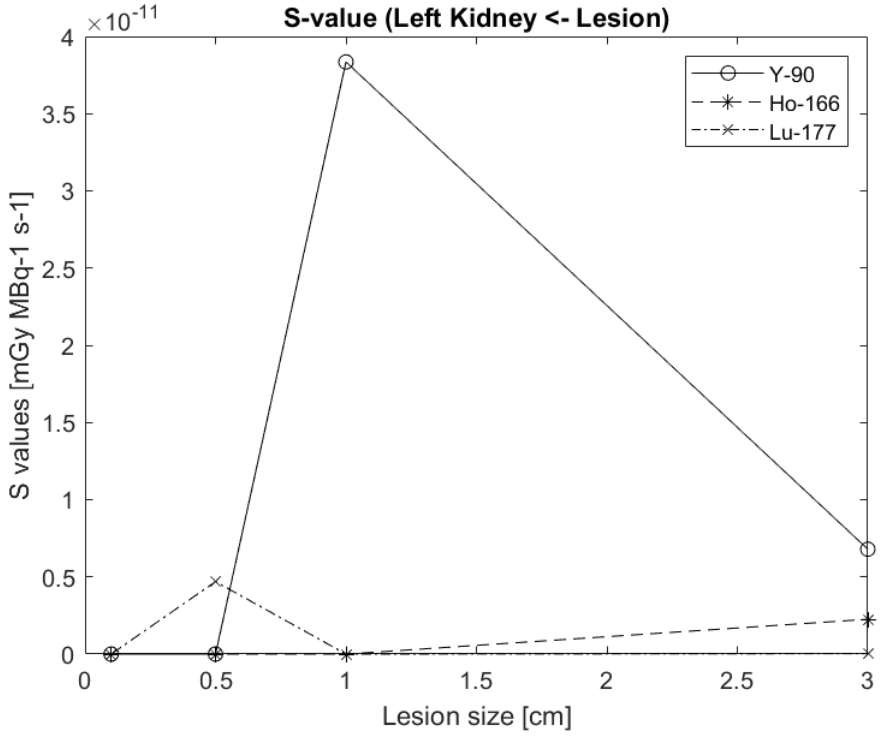

Figure 4.22: (Left Kidney ← Lesion) S-values (mGy $MBq^{-1}s^{-1}$) for Y-90, Ho-166 and Lu-177 in the ICRP 110 Male phantom

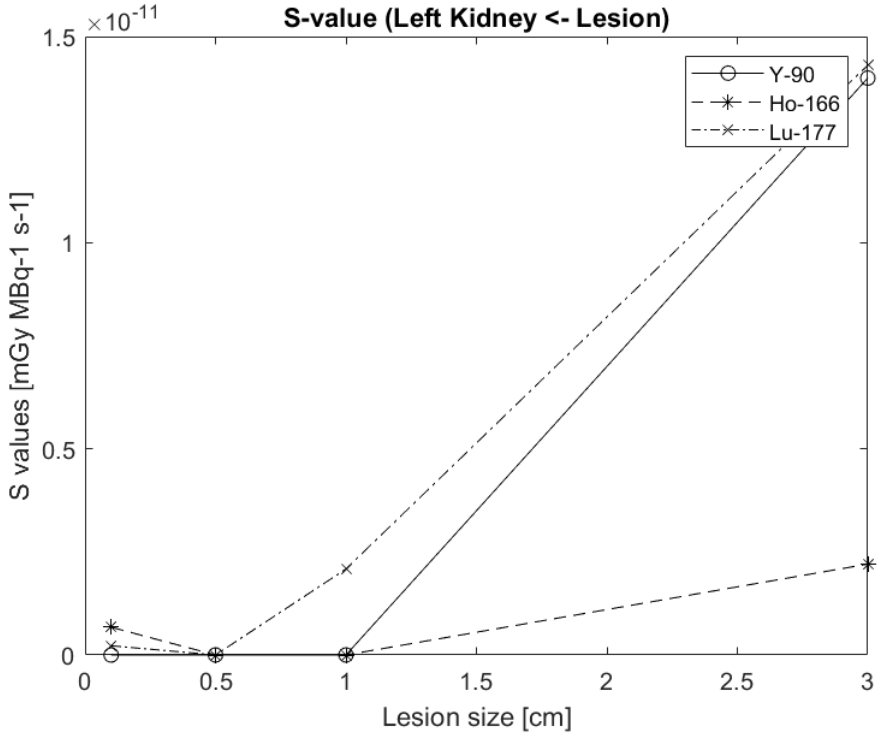

Figure 4.23: (Left Kidney ← Lesion) S-values (mGy $MBq^{-1}s^{-1}$) for Y-90, Ho-166 and Lu-177 in the ICRP 145 Male phantom

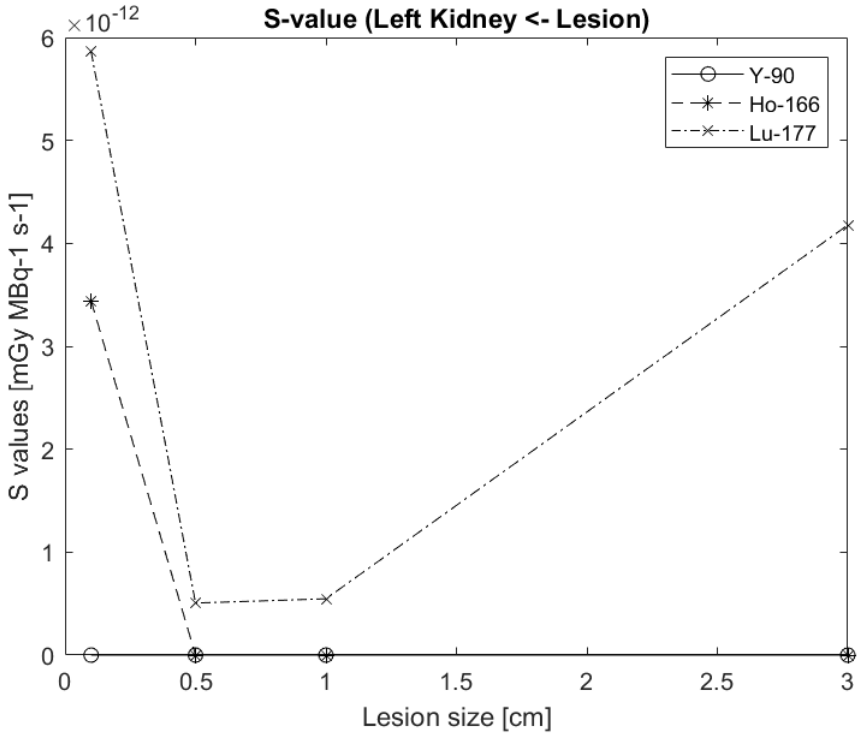

Figure 4.24: (Left Kidney ← Lesion) S-values (mGy $MBq^{-1}s^{-1}$) for Y-90, Ho-166 and Lu-177 in the ICRP 145 Male phantom

4.7 S-values for Right Kidney ← Lesion

The right kidney sits directly inferior to the main liver lobe, and will have a larger amount of energy deposited in the right kidney compared to the left kidney. It is expected the S-values will increase as the lesion size increases, however this is not apparent in any of the figures. For all Yttrium-90 plots, either the 0.1cm lesion or 0.5cm lesion had the largest S-value in all four phantoms, with the statistical uncertainty being greater in larger lesion sizes. Lutetium-177 S-values were generally greater than Holmium-166 S-values, as the average range of Lutetium-177 is larger, this is as expected.

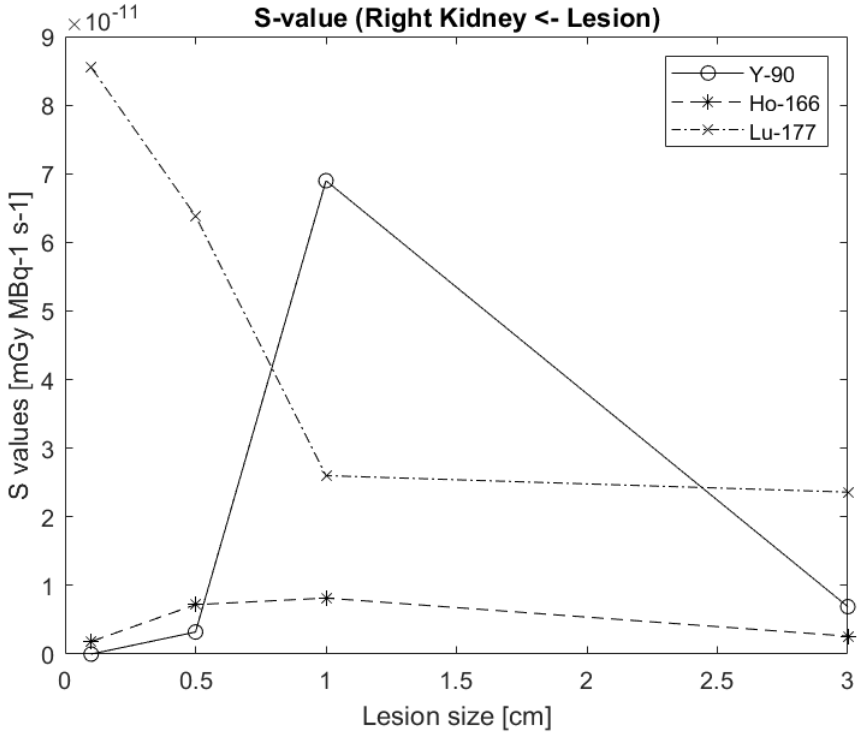

Figure 4.25: (Right Kidney ← Lesion) S-values (mGy $MBq^{-1}s^{-1}$) for Y-90, Ho-166 and Lu-177 in the ICRP 110 Female phantom

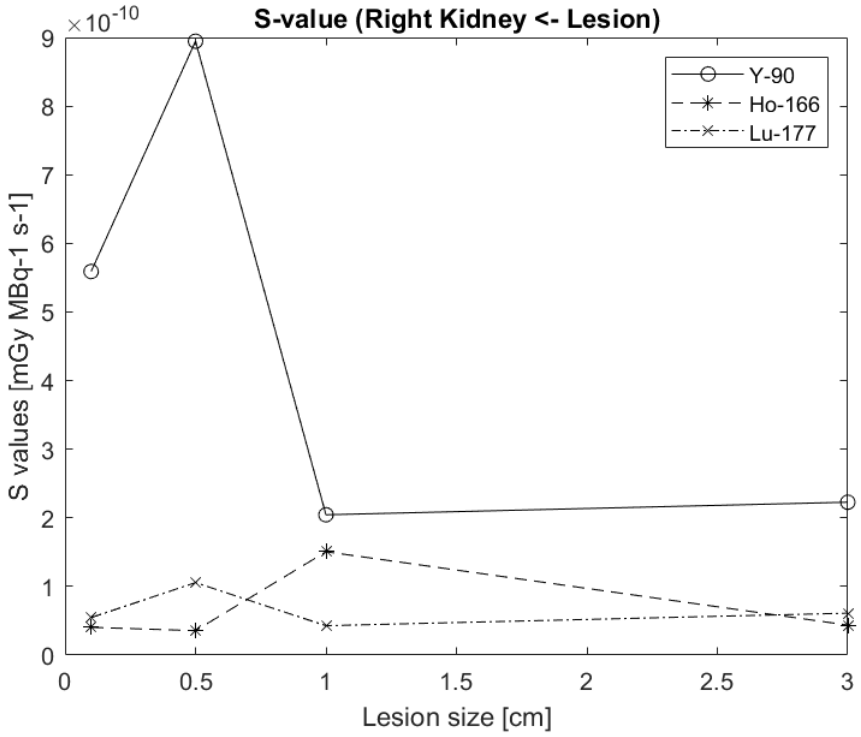

Figure 4.26: (Right Kidney ← Lesion) S-values (mGy $MBq^{-1}s^{-1}$) for Y-90, Ho-166 and Lu-177 in the ICRP 110 Male phantom

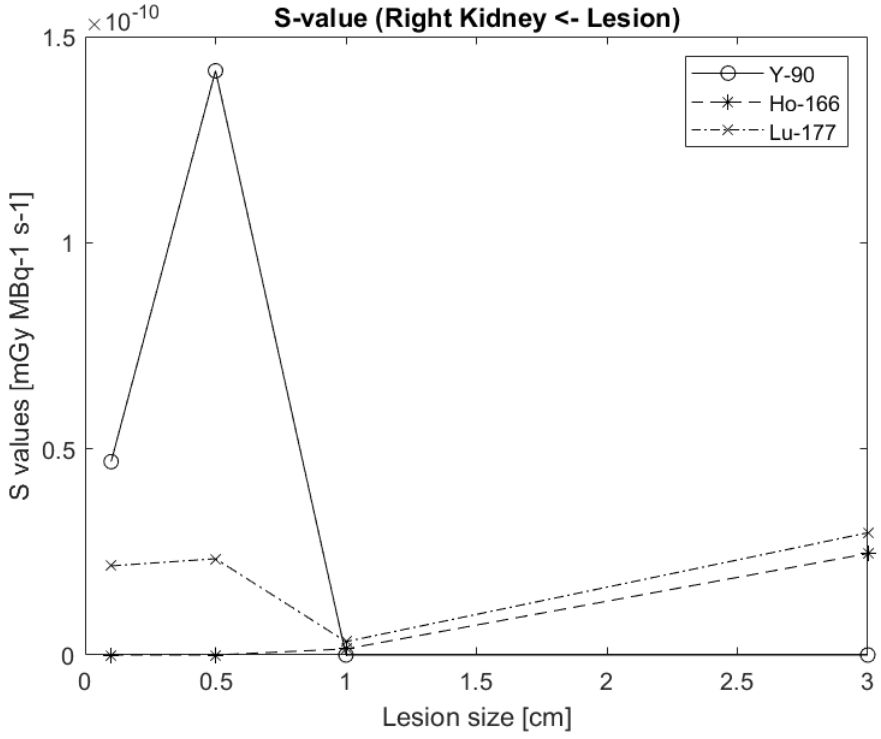

Figure 4.27: (Right Kidney ← Lesion) S-values (mGy $MBq^{-1}s^{-1}$) for Y-90, Ho-166 and Lu-177 in the ICRP 145 Male phantom

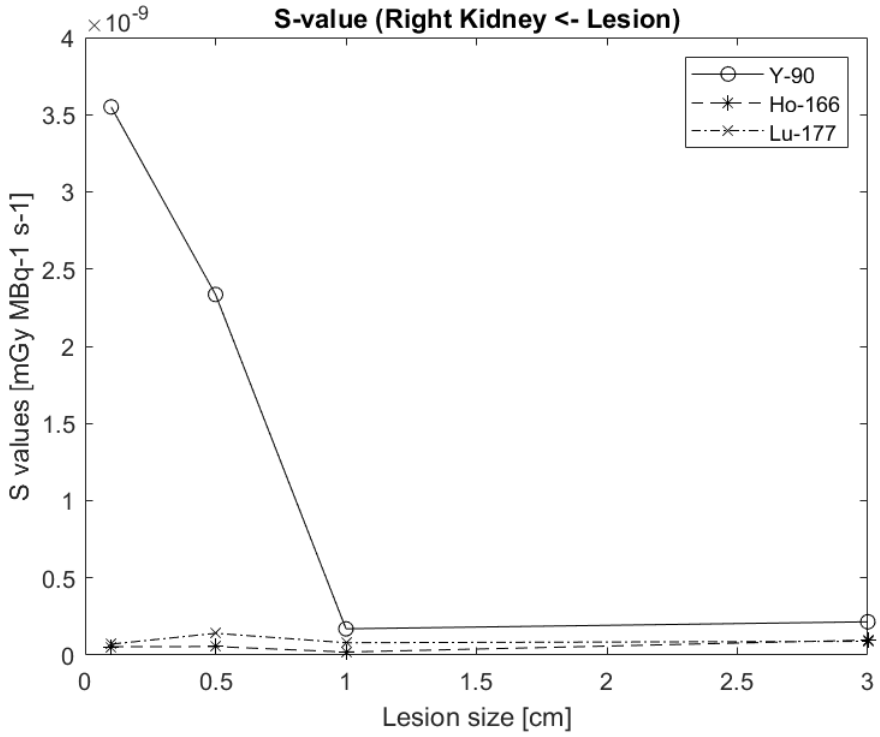

Figure 4.28: (Right Kidney ← Lesion) S-values (mGy $MBq^{-1}s^{-1}$) for Y-90, Ho-166 and Lu-177 in the ICRP 145 Male phantom

4.8 S-values for Spleen ← Lesion

The spleen is an organ that sits laterally to the stomach, sitting behind the left ribs. It is a component of the lymphatic system, and works to filter blood. It is a small organ, so the number of hits in this region is expected to be small, as well due to its anatomic location counts are expected to be smaller. In Figure 4.29, 4.30 and 4.31, Lutetium-177 has larger S-values in the Spleen than Yttrium-90, which does not agree with the theory presented. This is due to the small number of hits in the region, with large statistical uncertainties present for all data.

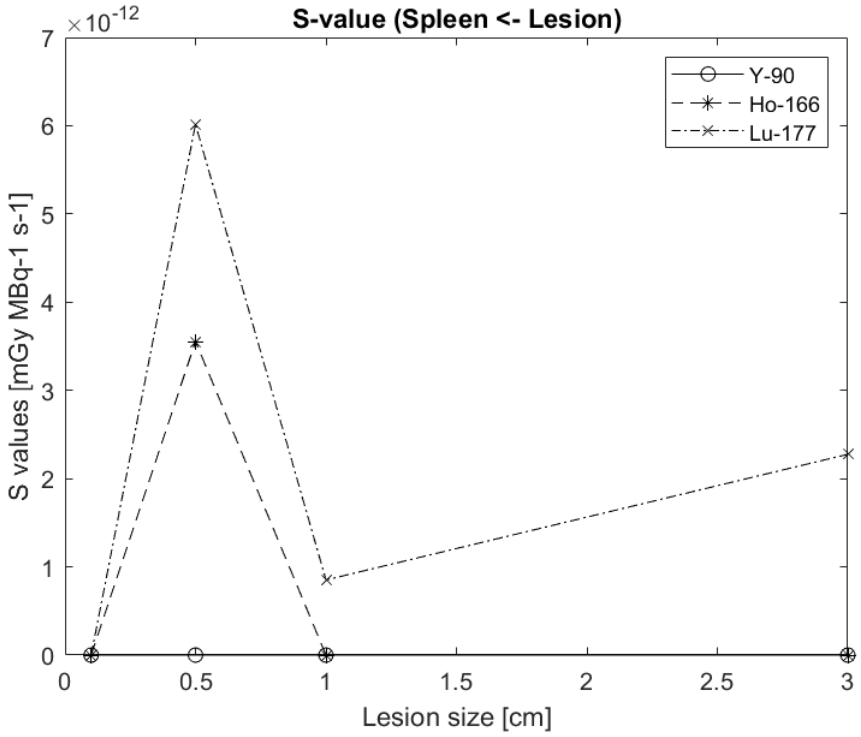

Figure 4.29: (Spleen ← Lesion) S-values (mGy $MBq^{-1}s^{-1}$) for Y-90, Ho-166 and Lu-177 in the ICRP 110 Female phantom

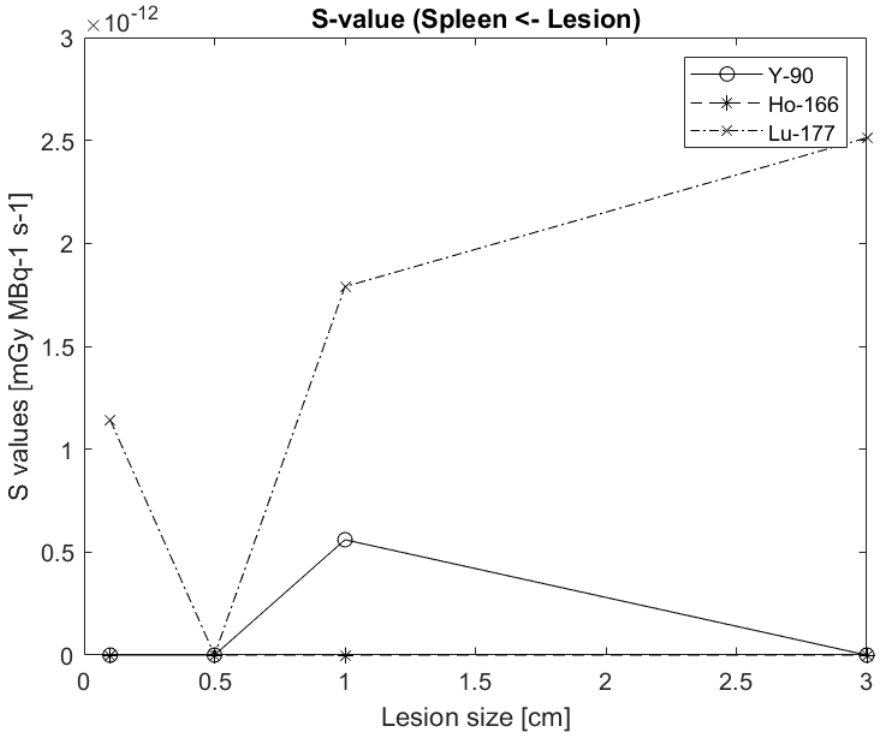

Figure 4.30: (Spleen ← Lesion) S-values (mGy $MBq^{-1}s^{-1}$) for Y-90, Ho-166 and Lu-177 in the ICRP 110 Male phantom

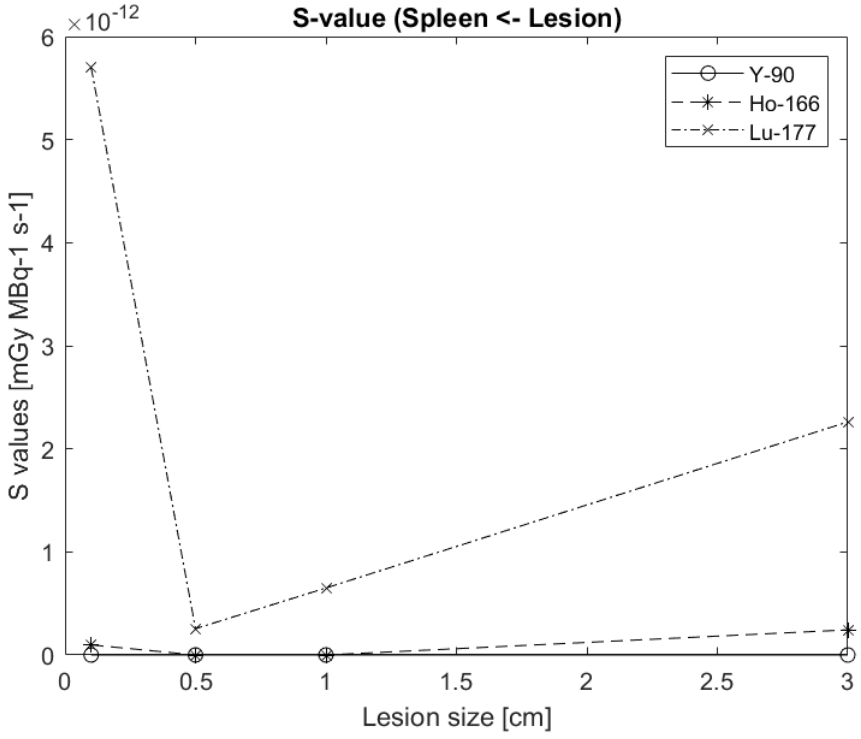

Figure 4.31: (Spleen ← Lesion) S-values (mGy $MBq^{-1}s^{-1}$) for Y-90, Ho-166 and Lu-177 in the ICRP 145 Male phantom

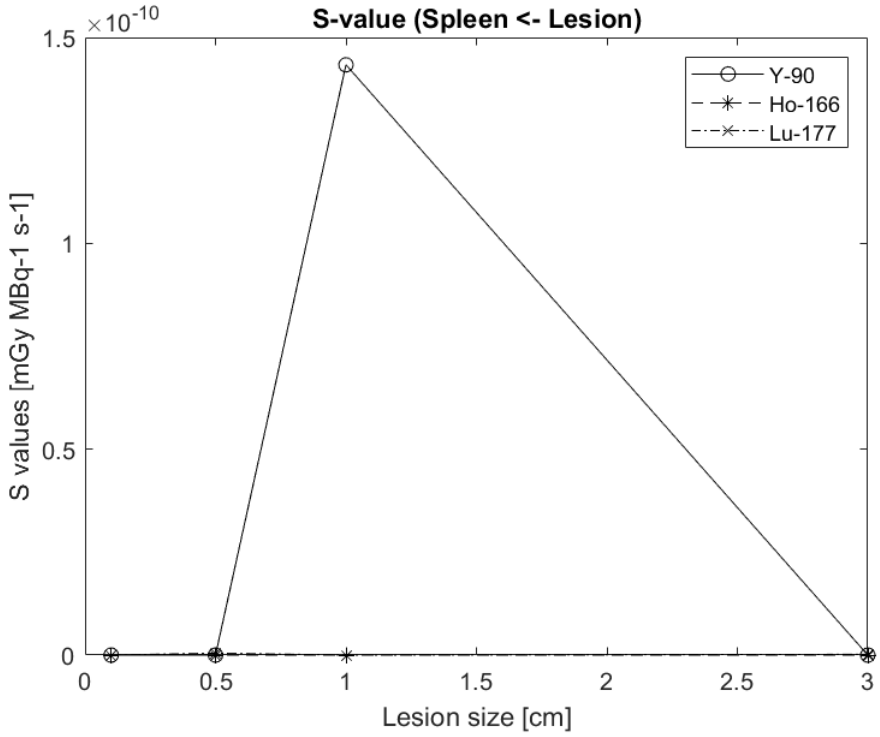

Figure 4.32: (Spleen ← Lesion) S-values (mGy $MBq^{-1}s^{-1}$) for Y-90, Ho-166 and Lu-177 in the ICRP 145 Male phantom

4.9 S-values for all organs in ICRP 145 male phantom for Ho-166, Lu-177 and Y-90 for 1cm diameter spherical source

Figures 4.33-4.35 show all non-zero S-values in the ICRP 145 male phantom for Ho-166, Lu-177 and Y-90 for 1cm diameter spherical source. The logarithmic scale was used to demonstrate the doses to organs outside the liver in a graphical manner. Due to the low hits in organs outside the liver, logarithmic values allow for this visualisation. For all radionuclides, the liver is estimated to have the largest S-value, due to the lesion sitting within the liver volume and the short range of beta emission. The S-value in the liver is largest for ^{166}Ho, at $5.793 \times 10^{-7}\ mGy\,MBq^{-1}s^{-1}$ for 1cm diameter spherical source. ^{90}Y, has the smallest estimated S-value in the liver with $5.571 \times 10^{-8}\ mGy\,MBq^{-1}s^{-1}$, a factor of 10 smaller than both Holmium-166 and Lutetium-177. It is observed the amount of organs in which hits were recorded in for the radionuclides, with Lu-177 recording hits in 56 organ IDs. Y-90 recorded hits in 37 organ IDs whilst Ho-166 hits were recorded in only 29. Amongst all three radionuclides, the gall bladder and right adrenal received relatively large dose amongst organs outside the liver. Only one phantom was selected as the results in organs outside the liver have large uncertainties , and will be explored for all phantoms in future works.

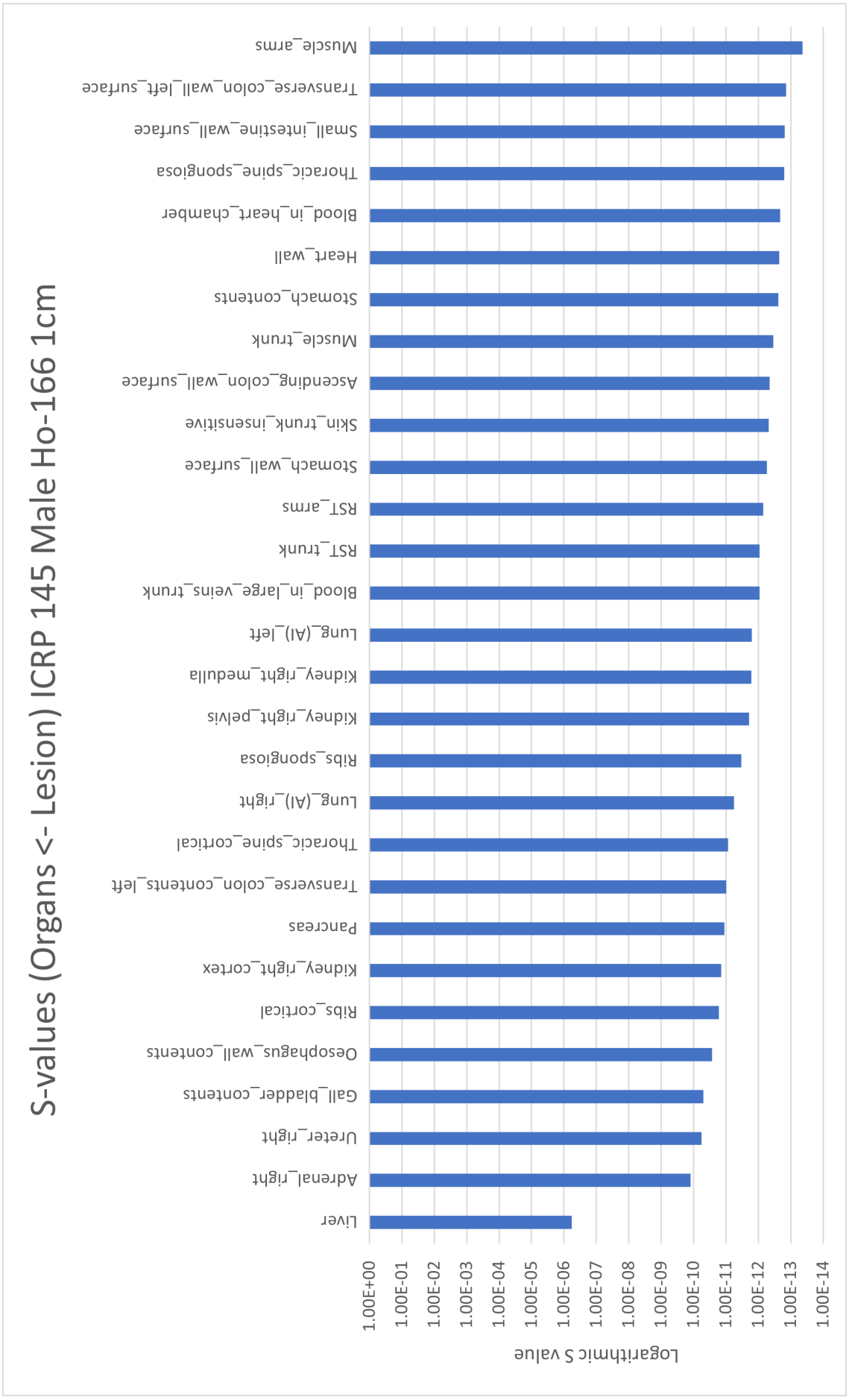

Figure 4.33: S-value (Organs ← Lesion) ICRP 145 Male Ho-166 1cm

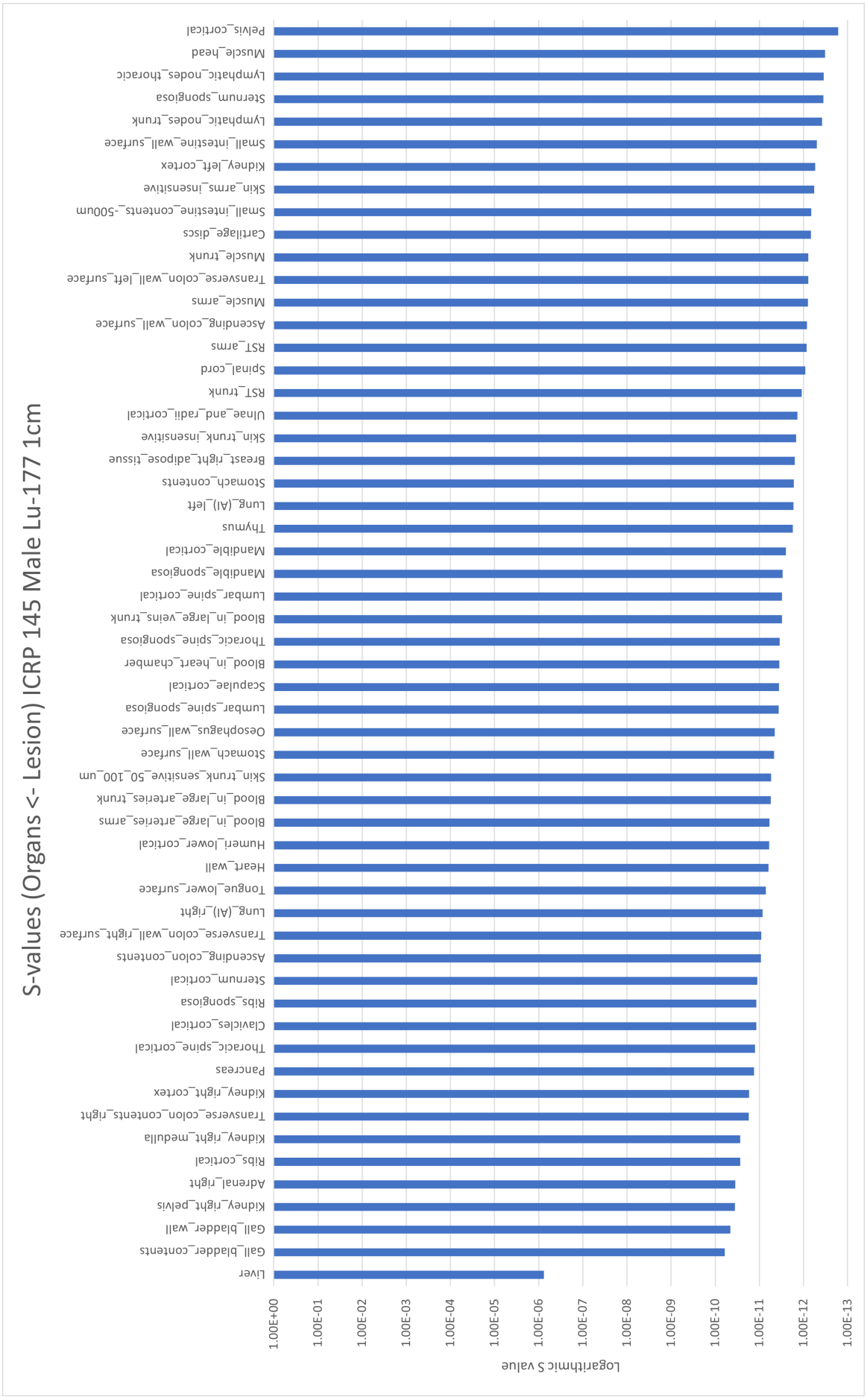

Figure 4.34: S-value (Organs ← Lesion) ICRP 145 Male Lu-177 1cm

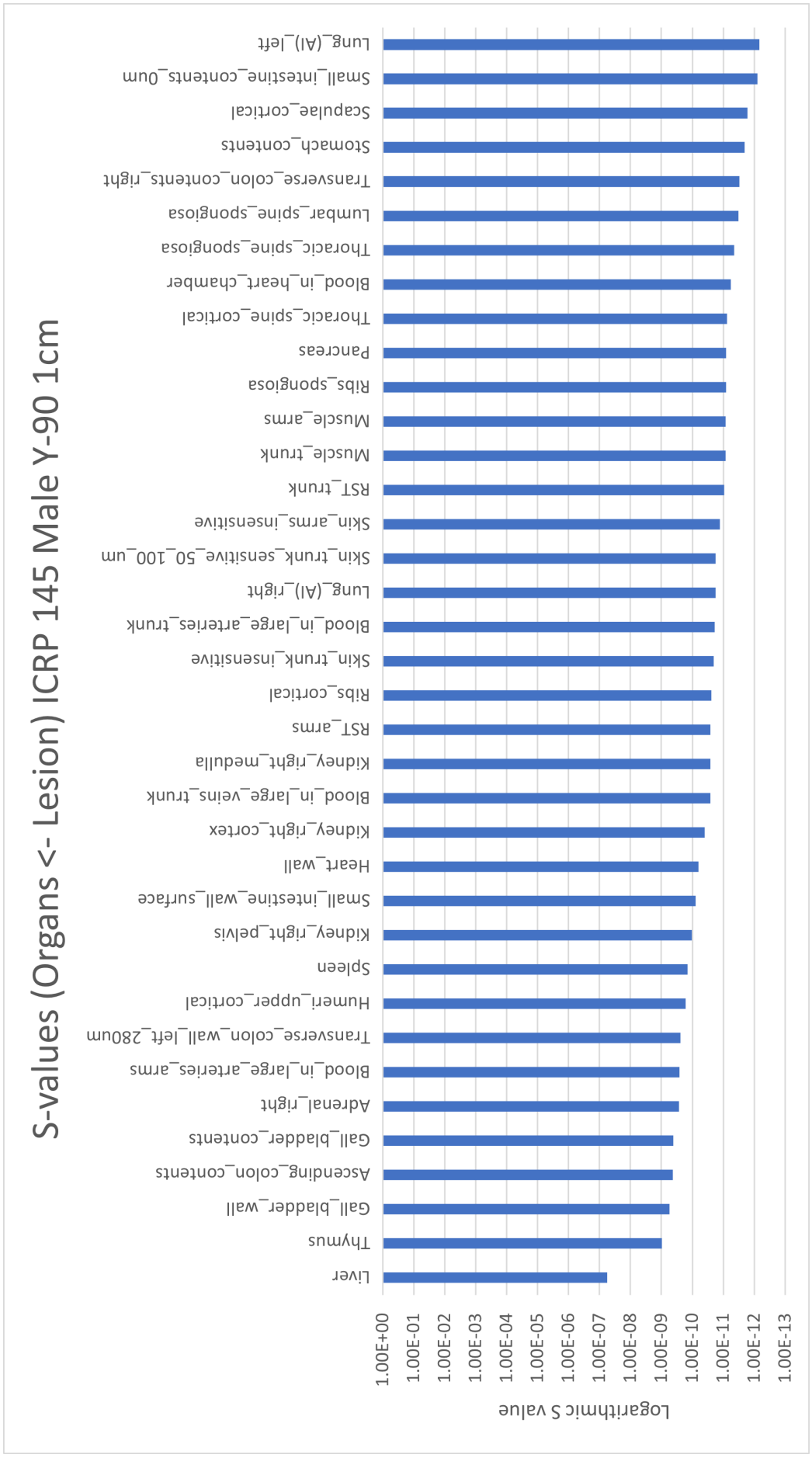

Figure 4.35: S-value (Organs ← Lesion) ICRP 145 Male Y-90 1cm

4.10 Phantom Comparison

Figures 4.36 shows the variation in S-values between each phantom: ICRP 110 male, ICRP 110 female, ICRP 145 male and ICRP 145 female, for the four spherical source sizes with Holmium-166. It is observed that the ICRP 110 Female phantom has the highest S-value recorded of $9.838 \times 10^{-7}\ mGyMBq^{-1}s^{-1}$ for the 3cm diameter spherical source, and the ICRP 145 Male phantom has the lowest S-value of $5.784 \times 10^{-7}\ mGyMBq^{-1}s^{-1}$ for the 3cm diameter spherical source. However, when considering the mass of liver for each phantom, observed in Table 4.1, the result is seen in Figure 4.37. The ICRP 110 Female phantom still has the largest S-value for no mass dependence, however the remaining three phantoms are clustered within $0.004 \times 10^{-6}\ mJMBq^{-1}s^{-1}$.

	ICRP 110		ICRP 145	
Organ	Female	Male	Female	Male
Liver Mass (g)	1400	1800	1810	2360
Liver Volume (cm^3)	1333.3	1714.3	1707.5	2226.4

Table 4.1: Liver mass and volume for ICRP 110 and 145 phantoms [33], [43]

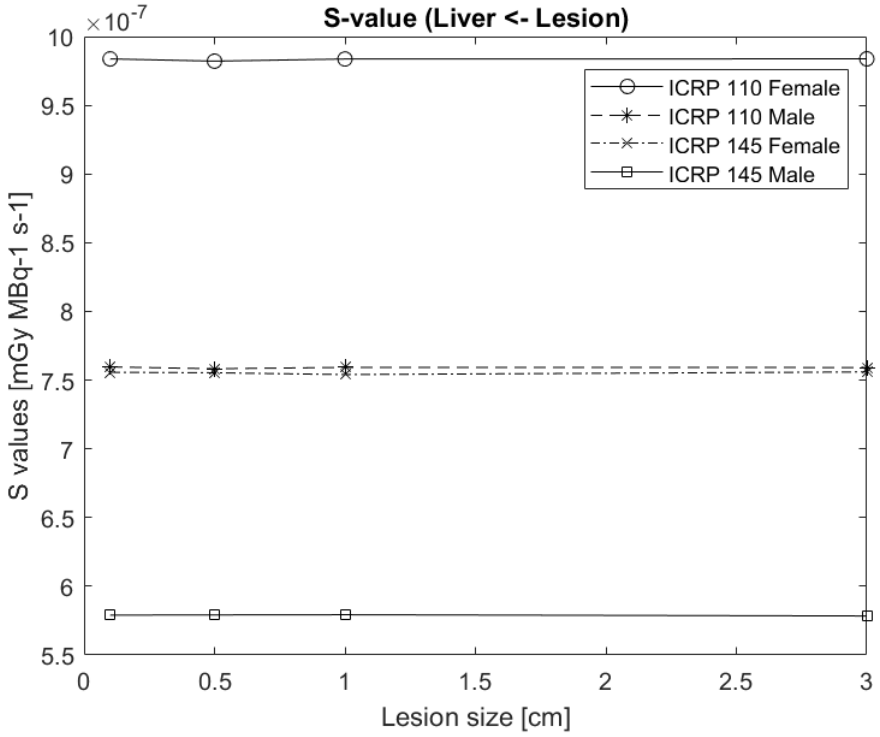

Figure 4.36: S-value (Liver ← Lesion) for ICRP 110 and 145 phantoms, using four different sized Holmium-166 spherical sources

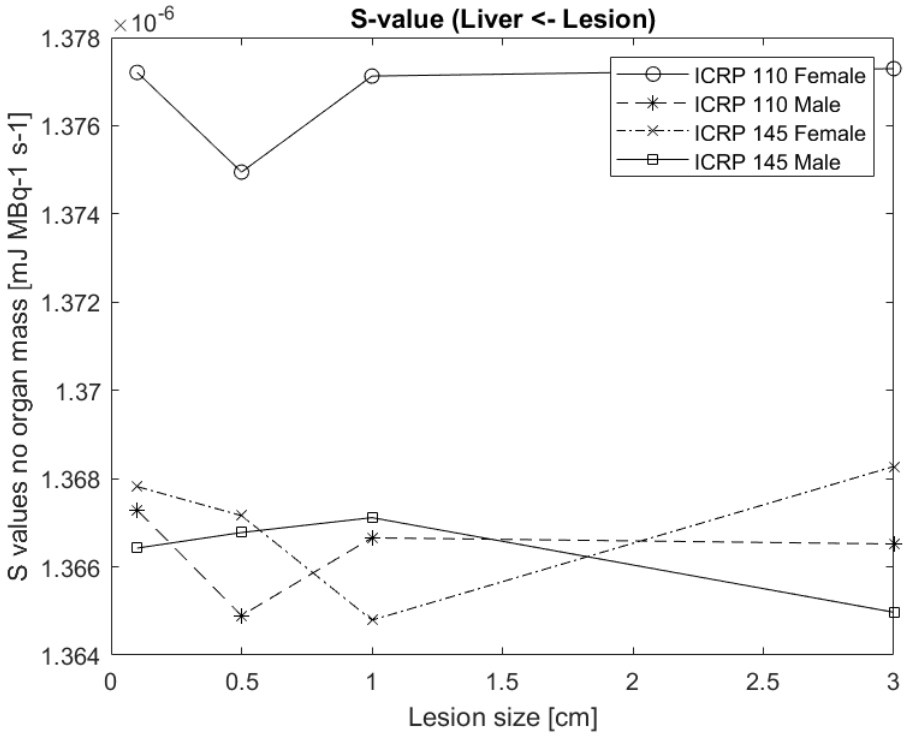

Figure 4.37: S-value (Liver ← Lesion) for ICRP 110 and 145 phantoms, using four different sized Holmium-166 spherical sources with no mass dependence

Chapter 5

Discussion

This project investigated S-values for 3 radionuclides used in targeted radionuclide therapy (Lu-177, Ho-166, Y-90) when the radiopharmaceutical is locally administered in liver lesions. The study compared S-values from spherical lesions in the liver to neighbouring organs. The S-values were calculated using the Geant4/GATE Monte Carlo tool and were conducted on the ICRP 110 voxel reference phantoms and the ICRP 145 mesh reference phantoms with 10 million particles run for each simulation.

For ICRP 110 and ICRP 145 males and females phantoms, Lutetium-177 deposited the highest S-value in liver compered to Ho-166 and Y-90. It has to be noted that the S-values for the liver include the healthy tissue as well as the lesion. For liver, the S-values ranged from 1.292×10^6 $mGy\,MBq^1s^1$ (Lu-177, sphere diameter = 0.5 cm) to 5.577×10^8 $mGy\,MBq^1s^1$ (Y-90, sphere diameter = 0.1 cm). It was found that the diameter of the lesion (from 0.1 cm to 3 cm sphere) had no significant impact on the S-values recorded within the liver, as most of the energy emitted by the radionuclides is deposited within the lesion or within the healthy liver tissue. As the Yttrium-90 lesion has the largest beta emission energy, the beta particles have a longer maximum and average path length, and therefore will escape the liver tissue more readily. This results in a smaller S-value produced within the liver, however produces a greater S-value in organs surrounding the liver (as shown in graphs 4.5 to 4.32. Yttrium-90's S-values range from 9.455×10^8 $mGy\,MBq^1s^1$ to 5.571×10^8 $mGy MBq^1s^1$, which is about 7% of the highest S-value for Lutetium-177 in the ICRP 110 Female Phantom. Holmium-166's S-value range from 9.840×10^7 $mGy\,MBq^1s^1$ to 5.788×10^8 $mGy\,MBq^1s^1$,showing a behaviour which is between Y-90 and Lu-177. As expected, Lutetium-177 will deliver the largest amount of locally deposited dose whilst depositing the lowest amount of radiation in neighbouring organs. In fact, the mean penetration range of 670 µm will result in a large amount of energy being deposited within the lesion itself. Given the short range of the beta emissions and the low abundance of the gamma emissions, when present, the liver S-values showed the lowest uncertainty. The S-values recorded outside the liver recorded a coefficient of variation greater than 5%. In some cases, the CV was as high as 100% due to the nature of the radionuclides. In Yttrium-90 (purely beta emitter), the maximum range of the beta particle is 11mm, so organs outside this (or close to) this range will expect low to no hits. When simulating 10 million

particles, one hit will cause a coefficient of variation of 100%.

Moreover, the S-values estimated for target organs outside the liver are expected to increase with the lesion size due to their proximity to the lesion. However, most plots produced in Chapter 5 had anomalies where smaller lesion sizes would produce larger S-values than larger lesion sizes. This is mainly due to an increased statistical uncertainty as the lesion is further away from the target organ. To reduce this uncertainty, and to improve the results the number of particles run will have to increase. In order to generate results with some statistical certainty, it is aimed that all S-values produced have all coefficients less than 1. In order to reduce uncertainty on the produced S-values, a higher number of particles should be run. The macros in future will be simulated and utilised on the NCI GADI supercomputer. The use of the cluster will be used to perform simulations, visualisations and calculations. Not only does GADI allow for faster simulation run times and job splitting, but utilises Geant4 version 10.7, to ensure up to date results. GADI utilises 155 thousand CPU cores, 567 Terabytes of memory and 640 GPUs to efficiently run simulations. Jobs are submitted to the NCI through pbs scripts, defining how the job is set up and the commands to be executed.

The results also showed that the female reference phantoms produced a greater S-value than their male counterparts. As the lesion sizes and central position remained constant throughout the simulations, the only variation is due to the mass of the organs. In the ICRP 145 annals [43], the male liver is 2.36 kg whilst the female is 1.81 kg. As the S-values are calculated using the dose (J/kg Number of particles simulated), the S-value will be increased for a smaller mass. From the comparison of the female and male phantoms, it was determined that the (Liver Lesion) S-values were 130% of the male phantom for the respective phantom. This ratio matches that of the weight ratios for the liver masses given in the annals. From the results it is also determined the S-values for the ICRP 110 voxel phantom are greater than that of the ICRP 145 mesh phantom. This is partly due to the weight of the organs from the ICRP 110 annals [33]. The male liver is listed as 1.8 kg whilst the female is 1.4 kg. This reduction in weight again will increase the S-values recorded. When converting the voxel phantom to the mesh phantom, some updates were included which includes the blood within the liver as weight to the organ. This has caused a change in the mass of the liver, hence a change in S-values determined. These have been noted in the ICRP133 annals [30]. The results of the (Liver Lesion) S-values found the mesh phantom was approximately 76% of the respective voxel phantom.

When observing the two ICRP phantoms, there is general limitations in the voxel model which have been rectified in the mesh phantom development. Due to the nature of the voxel phantom (limited resolution from the CT images used to generate the phantom), blood vessels and bone marrow is unable to be determined in the phantom. For this study, this has a limited impact due to the focus on soft tissue organs, however into the future, the research should utilise the mesh phantom for its higher accuracy on anatomical features. This accuracy is seen in the results presented, with a discrepancy of results between the ICRP 110 and the ICRP 145 phantoms. The main cause of disparity is due to the organ mass not including blood

in the voxel phantom whilst it does in the mesh phantom. This change of weight will alter the dose value calculated. In future calculations, it is possible to record the energy deposited on each source and target organ, and calculate the dose using a standard weight for males and females. However, this may create uncertainties for the voxel phantom, due to the nature of voxels creating a rigid surface area. This will result in a larger area (number of voxels) being considered liver tissue compared to the mesh phantom (number of tetrahedron).

The source sizes selected were chosen to represent various tumour sizes within the liver, with a maximum sphere diameter of 3cm. In future studies, it is planned to run simulations that determine the dose to healthy liver tissue by subtracting the energy deposited within the lesion from the energy deposited in the whole liver and dividing by the healthy liver mass. It is expected that the smaller lesion sizes will deposit a larger amount of dose to healthy tissue compared to larger lesion sizes, as the larger lesions will have some beta particles which escape the liver and deposit dose in other tissue.

In order to understand the nature of each radioisotope, simulations should investigate the separate contributions of the beta and the gamma emissions. This will allow for the makeup of each radionuclide's dose deposition to be observed. To apply this work in a clinical scenario, the absorbed doses can be determined for each radionuclide by looking at the effective half-life (of each radionuclide and biological half-life for microspheres) and activity administered. This can be used to generate dosimetry information for patients and nuclear medicine staff on common procedures.

Chapter 6

Conclusion

The aim of this study was to investigate dose to neighbouring organs from activities of Lutetium-177, Holmium-166 and Yttrium-90 in liver lesions. This was conducted by implementing spherical sources in the liver of the ICRP 110 and ICRP 145 phantoms in Geant4/GATE. It was shown that Lutetium-177 recorded the highest S-value (Liver $\leftarrow$ Lesion), while Yttrium-90 recorded the lowest S-value (Liver $\leftarrow$ Lesion). It was demonstrated the dose to the liver for Holmium-166 was largest for the ICRP 110 female phantom when there was no mass dependence, whilst the remaining three phantoms have similar dose deposition on the liver. Due to the small number of particles simulated (10^7), the statistical uncertainty outside of the source organ was significant and future work will aim to increase the number of particles simulated to provide S-values for all target organs within the body with reasonable statistics. A further investigation may have the liver volume and mass to be matched for all models to determine dose. This work will improve understanding of radiation dose to neighbouring organs from trans-arterial radioembolisation using Lutetium-177, Holmium-166 and Yttrium-90.

Bibliography

[1]Australian Institute of Health and Welfare 2021, *Cancer data in Australia*, Canberra: AIHW.

[2]Australian Institute of Health and Welfare 2021, *Cancer data in Australia*, Canberra: AIHW.

[3]P. Metcalfe, T. Kron, and P. Hoban, *The Physics of Radiotherapy X-rays and Electrons* (2007).

[4]S. Cherry, J. Sorensen, and M. Phelps, *Physics in Nuclear Medicine* (Elsevier/Saunders).

[5]R. Baskar, K. Lee, R. Yeo, and K. Yeoh, "Cancer and radiation therapy: current advances and future directions", International Journal of Medical Sciences **9(3)**, 193–199 (2012) https://doi.org/10.7150/ijms.3635.

[6]J. A. Marrero, L. M. Kulik, C. B. Sirlin, A. X. Zhu, R. S. Finn, M. M. Abecassis, L. R. Roberts, and J. K. Heimbach, "Diagnosis, staging, and management of hepatocellular carcinoma: 2018 practice guidance by the american association for the study of liver diseases", Hepatology **68**, 723–750 (2018) https://doi.org/10.1002/hep.29913.

[7]C. Kratochwil, R. López-Benítez, W. Mier, S. Haufe, B. Isermann, H.-U. Kauczor, P. L. Choyke, U. Haberkorn, and F. L. Giesel, "Hepatic arterial infusion enhances dotatoc radiopeptide therapy in patients with neuroendocrine liver metastases", Endocrine-Related Cancer **18**, 595–602 (2011) 10.1530/ERC-11-0144.

[8]J. Lubel, S. Roberts, S. Strasser, and A. Thompson, "Australian recommendations for the management of hepatocellular carcinoma: a consensus statement", The Medical Journal of Australia **214(10)**, 475–483 (2021) 10.5694/mja2.50885.

[9]T. Meyer, R. Fox, and Y. Ma, "Sorafenib in combination with transarterial chemoembolisation in patients with unresectable hepatocellular carcinoma (TACE 2): a randomised placebo-controlled, double-blind, phase 3 trial", The Lancet Gastroenterology and Hepatology **2**, 565–575 (2017).

[10]European Association for the Study of the Liver, "Easl clinical practice guidelines: management of hepatocellular carcinoma", Journal of Hepatology **69**, 182–236 (2018) https://doi.org/10.1016/j.jhep.2018.03.019.

[11]L. Emmett, K. Willowson, and J. Violet, "Lutetium177 psma radionuclide therapy for men with prostate cancer: a review of the current literature and discussion of practical aspects of therapy", Journal of Medical Radiation Sciences **64(1)**, 52–60 (2017) 10.1002/jmrs.227.

[12]S. St. James, B. Bednarz, and S. Benedict, "Current status of radiopharmaceutical therapy", International Journal of Radiation Oncology Biology Physics **109(4)**, 891–901 (2021) https://doi.org/10.1016/j.ijrobp.2020.08.035.

[13]N. Mehrotra, M. Gupta, A. Kovar, and B. Meibohm, "The role of pharmacokinetics and pharmacodynamics in phosphodiesterase-5 inhibitor therapy", International Jurnal of Impotence Research **19**, 253–264 (2007) https://doi.org/10.1038/sj.ijir.3901522.

[14]J. Bushberg, J. Seibert, and E. Lediholdt, *The Essential Physics of Medical Imaging*, Vol. 3rd Edition (2012), pp. 705–746.

[15]N. Klaassen, M. Arntz, A. Arranja, J. Roosen, and J. Nijsen, "The various therapeutic applications of the medical isotope holmium-166: a narrative review", EJNMMI Radiopharmacy and Chemistry **4(1)**, https://doi.org/10.1186/s41181-019-0066-3 (2019) https://doi.org/10.1186/s41181-019-0066-3.

[16]C. Bouvry, X. Palard, and J. Edeline, "Transarterial radioembolization (tare) agents beyond 90y-microspheres", BioMed Research International **1435302**, 10.1155/2018/1435302 (2018) 10.1155/2018/1435302.

[17]H. Kim, "Radioembolization for the treatment of hepatocellular carcinoma", Clinical and Molecular Hepatology **23(2)**, 109–114 (2017) 10.3350/cmh.2017.0004.

[18]K. Memon, R. Lewandowski, L. Kulik, A. Riaz, M. Mulcahy, and R. Salem, "Radioembolization for primary and metastatic liver cancer", Seminars in Radiation Oncology **21(4)**, 294–302 (2011) 10.1016/j.semradonc.2011.05.004.

[19]U. Elboga, "Yttrium-90 selective internal radiation therapy for liver tumors", in *Radionuclide treatments*, edited by C. Soydal (IntechOpen, Rijeka, 2017) Chap. 5, 10.5772/intechopen.69328.

[20]B. Sangro, R. Salem, A. Kennedy, D. Coldwell, and H. Wasan, "Radioembolization for hepatocellular carcinoma: a review of the evidence and treatment recommendations", American Journal of clinical oncology **34(4)**, 422–431 (2011) 10.1097/COC.0b013e3181df0a50.

[21]R. Sacco, V. Mismas, S. Marceglia, A. Romano, and L. Giacomelli, "Transarterial radioembolization for hepatocellular carcinoma: An update and perspectives", World Journal of Gastroeneterology **21(21)**, 6518–6525 (2015) 10.3748/wjg.v21.i21.6518.

[22]X. Xu, "An exponential growth of computational phantom research in radiation protection, imaging, and radiotherapy: a review of the fifty-year history", Physics in Medicine and Biology **59(18)**, R233–R302 (2014) 10.1088/0031-9155/59/18/R233.

[23]W. E. Bolch, K. F. Eckerman, G. Sgouros, and S. R. Thomas, "MIRD Pamphlet No. 21: A Generalized Schema for Radiopharmaceutical Dosimetry—Standardization of Nomenclature", Journal of Nuclear Medicine **50(3)**, 477–484 (2009) 10.2967/jnumed.108.056036.

[24]Y. Dewarja, E. Frey, G. Sgouros, A. Bertrand Brill, P. Roberson, P. Zanzonico, and M. Ljungberg, "MIRD pamphlet No. 23: quantitative SPECT for patient-specific 3-dimensional dosimetry in internal radionuclide therapy", Journal of Nuclear Medicine **53(8)**, 1310–1325 (2012) 10.2967/jnumed.111.100123..

[25]L. Strigari, M. Konijnenberg, C. Chiesa, M. Bardies, Y. Du, K. Sjogreen-Glesiner, M. Lassmann, and G. Flux, "The evidence base for the use of internal dosimetry in the clinical practice of molecular radiotherapy", European Journal of Nuclear Medicine and Molecular Imaging **41**, 1976–1988 (2014) https://doi.org/10.1007/s00259-014-2824-5.

[26]M. Ljungberg, A. Cellar, M. Konijnenberg, K. Eckerman, y. Dewaraja, and K. Sjogreen-Gleisner, "MIRD Pamphlet No. 26: Joint EANM/MIRD Guidelines for Quantitative 177Lu SPECT Applied for Dosimetry of Radiopharmaceutical Therapy", Journal of Nuclear Medicine **57(1)**, 151–162 (2016) 10.2967/jnumed.115.159012.

[27]C. Uribe, A. Peterson, B. Van, R. Fedrigo, J. Carlson, J. Sunderland, E. Frey, and Y. Dewaraja, "An International Study of Factors Affecting Variability of Dosimetry Calculations, Part 1: Design and Early Results of the SNMMI Dosimetry Challenge", Journal of Nuclear Medicine **62**, 36S–47S (2021) https://doi.org/10.2967/jnumed.121.262748.

[28]S. Mattsson, "Patient Dosimetry in Nuclear Medicine", Radiation Protection Dosimetry **165(1-4)**, 416–423 (2015) 10.1093/rpd/ncv061.

[29]U. Eberlein, "Biokinetics and dosimetry of commonly used radiopharmaceuticals in diagnostic nuclear medicine - a review", European Journal of Nuclear Medicine and Molecular Imaging **38(12)**, 2269–2281 (2011) 10.1007/s00259-011-1904-z.

[30]W. Bolch, D. Jokisch, M. Zankl, K. Eckerman, T. Fell, R. Manger, A. Endo, J. Hunt, K. Kim, and N. Petoussi-Henss, "The ICRP computational framework for internal dose assessment for reference adults: specific absorbed fractions. ICRP Publication 133", Annals of the ICRP **45(2)**, 5–73 (2016) 10.1177/0146645316661077.

[31]K. Eckerman and A. Endo, "Nuclear decay data for dosimetric calculations. ICRP Publication 107", Annals of the ICRP **38(3)**, 7–96 (2008) {10.1016/j.icrp.2008.10.004}.

[32]M. Andersson, L. Johansson, K. Eckerman, and S. Mattsson, "IDAC-Dose 2.1, an internal dosimetry program for diagnostic nuclear medicine based on the ICRP adult reference voxel phantoms", European Journal of Nuclear Medicine and Medical Imaging **7(1)**, 10.1186/s13550-017-0339-3. (2017) 10.1186/s13550-017-0339-3..

[33]H. Menzel, C. Clement, and P. DeLuca, "ICRP Publication 110. Realistic reference phantoms: an ICRP/ICRU joint effort. A report of adult reference computational phantoms", Annals of the ICRP **39(2)**, 1–164 (2009).

[34]C. Kim, Y. Yeom, T. Nguyen, Z. Wang, H. Kim, M. Han, J. Lee, M. Zankl, N. Petoussi-Henss, W. Bolch, C. Lee, and B. Chung, "The reference phantoms: voxel vs polygon", Annals of the ICRP **45(1 Suppl)**, 188–201 (2016) 10.1177/0146645315626036.

[35]"The 2007 Recommendations of the International Commission on Radiological Protection. ICRP Publication 103", Annals of the ICRP **37(2-4)**, edited by J. Valentin, 1–332 (2007) 10.1016/j.icrp.2007.10.003.

[36]"Basic Anatomical and Physiological Data for Use in Radiological Protection: Reference Values. ICRP Publication 89", Annals of the ICRP **32(3-4)**, edited by J. Valentin, 1–277 (2002) 10.1016/S0146-6453(03)00002-2.

[37]M. Zankl and A. Wittmann, "The adult male voxel model "Golem" segmented from whole-body CT patient data", Radiation and environmental biophysics **40(2)**, 153–162 (2001) https://doi.org/10.1007/s004110100094.

[38]M. Zankl, J. Becker, and U. Fill, "GSF male and female adult voxel models representing ICRP Reference Man – the present status", American Nuclear Society (2005).

[39]Y. S. Yeom, J. H. Jeong, M. C. Han, and C. H. Kim, "Tetrahedral-mesh-based computational human phantom for fast Monte Carlo dose calculations", Physics in Medicine and Biology **59(12)**, 3173–3185 (2014) https://doi.org/10.1088/0031-9155/59/12/3173.

[40]H. Si, "Tetgen, a delaunay-based quality tetrahedral mesh generator", ACM Transactions on Mathematical Software **41(2)**, http://doi.acm.org/10.1145/2629697 (2015) http://doi.acm.org/10.1145/2629697.

[41]Able Software Corp., *3D-Doctor User's Manual: 3D imaging, Modeling and Measurement Software*, 2012.

[42]C. H. Kim, Y. S. Yeom, T. T. Nguyen, M. C. Han, C. Choi, H. Lee, H. Han, B. Shin, J. K. Lee, H. S. Kim, M. Zankl, N. Petoussi-Henss, W. E. Bolch, C. Lee, B. S. Chung, R. Qiu, and K. Eckerman, "New mesh-type phantoms and their dosimetric applications, including emergencies", Annals of the ICRP **47(3-4)**, 45–62 (2018) https://doi.org/10.1177/0146645318756231.

[43]C. Kim, Y. Yeom, N. Petoussi-Henns, M. Zankl, W. Bolch, C. Lee, C. Choi, T. Nguyen, K. Eckerman, H. Kim, M. Han, R. Qiu, B. Chung, H. Han, and B. Shin, "Adult mesh-type reference computational phantoms. ICRP Publication 145", Annals of the ICRP **49(3)**, 10.1177/0146645319893605 (2020) 10.1177/0146645319893605.

[44]Y. S. Yeom, M. C. Han, C. H. Kim, and J. H. Jeong, "Conversion of ICRP male reference phantom to polygon-surface phantom", Physics in Medicine and Biology **58(19)**, 6985–7007 (2013) https://doi.org/10.1088/0031-9155/58/19/6985.

[45]C. Lee, D. Lodwick D.and Hasenauer, J. L. Williams, C. Lee, and W. E. Bolch, "Hybrid computational phantoms of the male and female newborn patient: NURBS-based whole-body models", Physics in Medicine and Biology **52(12)**, 3309–3333 (2007) https://doi.org/10.1088/0031-9155/52/12/001.

[46]T. Liu, X. Du, and L. Su, "ARCHER-CT, an extremely fast Monte Carlo code for patient-specific CT dose calculations using Nvidia GPU and Intel coprocessor technologies: Part I—software development and testing", Physics in Medicine and Biology (2014).

[47]L. Su, Y. Yang, B. Bednarx, E. Syerpin, X. Du, and T. Liu, " ARCHER—A photon-electron coupled Monte Carlo dose computing engine for GPU: software development and application to helical tomotherapy", (2014).

[48]W. Bolch, C. Lee, M. Wayson, and P. Johnson, "Hybrid computational phantoms for medical dose reconstruction", Radiation and Environmental Biophysics **49(2)**, 155–168 (2010) 10.1007/s00411-009-0260-x.

[49]J. Allison, K. Amako, J. Apostolakis, H. Araujo, P. Dubois, M. Asai, G. Barrand, R. Capra, S. Chauvie, R. Chytracek, G. Cirrone, G. Cooperman, G. Cosmo, G. Cuttone, G. Daquino, M. Donszelmann, M. Dressel, G. Folger, F. Foppiano, J. Generowicz, V. Grichine, S. Guatelli, P. Gumplinger, A. Heikkinen, I. Hrivnacova, A. Howard, S. Incerti, V. Ivanchenko, T. Johnson, F. Jones, T. Koi, R. Kokoulin, M. Kossov, H. Kurashige, V. Lara, S. Larsson, F. Lei, O. Link, F. Longo, M. Maire, A. Mantero, B. Mascialino, I. McLaren, P. Lorenzo, K. Minamimoto, K. Murakami, P. Nieminen, L. Pandola, S. Parlati, L. Peralta, J. Perl, A. Pfeiffer, M. Pia, A. Ribon, P. Rodrigues, G. Russo, S. Sadilov, G. Santin, T. Sasaki, D. Smith, N. Starkov, S. Tanaka, E. Tcherniaev, B. Tome, A. Trindade, P. Truscott,

L. Urban, M. Verderi, A. Walkden, J. Wellisch, D. Williams, D. Wright, and H. Yoshida, "Geant4 developments and applications", IEEE transactions on nuclear science **53**, 270–278 (2006).

[50]D. Sarrut, M. Bardiès, N. Boussion, N. Freud, S. Jan, J. Létang, G. Loudos, L. Maigne, S. Marcatili, T. Mauxion, P. Papadimitroulas, Y. Perrot, U. Pietrzyk, C. Robert, D. Schaart, D. Visvikis, and I. Buvat, "A review of the use and potential of the GATE Monte Carlo simulation code for radiation therapy and dosimetry applications", Medical physics **41(6)**, 064301 (2014) 10.1118/1.4871617.

[51]S. Ebbers, A. Braat, and A. Moelker, "Intra-arterial versus standard intravenous administration of lutetium-177-DOTA-octreotate in patients with NET liver metastases: study protocol for a multicenter, randomized controlled trial (LUTIA trial)", Trials **21**, 141 (2020) https://doi.org/10.1186/s13063-019-3888-0.

[52]L. Johnson and J. Yanch, "Absorbed dose profiles for radionuclides of frequent use in radiation synovectomy", Arthritis and Rheumatology **12**, 1521–1530 (1991) 10.1002/art.1780341208.

[53]C. Wright, J. Zhang, M. Tweedle, M. Knpp, and N. Hall, "Theranostic Imaging of Yttrium-90", BioMed Research International **481279**, 10.1155/2015/481279 (2015) 10.1155/2015/481279.

[54]"1990 Recommendations of the International Commission on Radiological Protection. ICRP Publication 60", Annals of the ICRP **21(1-3)**, edited by H. Smith, 1–211 (1991) 10.1177.

[55]Saha, G.B., "Internal Radiation Dosimetry", in *Physics and Radiobiology of Nuclear Medicine* (Springer, New York, NY, 2006), pp. 208–225, {10.1007/978-0-387-36281-6_14}.

[56]M. J. Welch and C. S. Redvanly, *Handbook of radiopharmaceuticals : Radiochemistry and applications* (J. Wiley, New York, 2003).

[57]J.-V. Kratz and K. H. Lieser, *Nuclear and Radiochemistry: Fundamentals and Applications*, 3rd ed. (John Wiley Sons, Incorporated, Weinheim, 2013).

[58]W. Bakker, W. Breeman, and D. Kwekkeboom, "Practical aspects of peptide receptor radionuclide therapy with [177lu][dota0, tyr3]octreotate", The Quarterly Journal of Nuclear Medicing and Molecular Imaging **50(4)**, 265–271 (2006).

[59]K. Kim and S. Kim, "Lu-177-based peptide receptor radionuclide therapy for advanced neuroendocrine tumors", Nuclear Medicine and Molecular Imaging **52(3)**, 208–215 (2018) 10.1007/s13139-017-0505-6.

[60]A. Dash, M. Pillai, and F. Knapp Jr, "Production of 177lu for targeted radionuclide therapy: available options", Nuclear Medicine and Molecular Imaging **49(2)**, 85–107 (2015) 10.1007/s13139-014-0315-z.

[61]J. Nijsen, B. Zonnenberg, J. Woittiez, and D. Rook, "Holmium-166 poly lactic acid microspheres applicable for intra-arterial radionuclide therapy of hepatic malignancies: effects of preparation and neutron activation techniques", European Journal of Nuclear Medicine **7**, 699–704 (1999) 10.1007/s002590050440.

[62]J. Nijsen and G. Krijger, "The Bright Future of Radionuclides for Cancer Therapy", Anti-Cancer Agents in Medicinal Chemistry **7(3)**, 271–290 (2007) 10.2174/187152007780618207.

[63]M. L. Smits, J. F. Nijsen, M. A. van den Bosch, M. G. Lam, M. A. Vente, W. P. Mali, A. D. van het Schip, and B. A. Zonnenberg, "Holmium-166 radioembolisation in patients with unresectable, chemorefractory liver metastases (hepar trial): a phase 1, dose-escalation study", The Lancet Oncology **13(10)**, 1025–1034 (2012) https://doi.org/10.1016/S1470-2045(12)70334-0.

[64]K. Kossert and H. Schrader, "Activity standardization by liquid scintillation counting and half-life measurements of 90Y", Applied radiation and isotopes : including data, instrumentation and methods for use in agriculture, industry and medicine **60(5)**, 741–749 (2004) https://doi.org/10.1016/j.apradiso.2003.12.009.

[65]Laboratoire National Henri Becquerel, *Y-90m tables*, http://www.nucleide.org/DDEP_WG/Nuclides/Y-90m_tables.pdf.

[66]International Commission on Radiation Units and Measurements (ICRU), "Fundamental Quantities and Units for Ionizing Radiation. Report 60", ICRU (1998).

[67]R. Asl, A. Parach, S. Nasseri, and M. Momennezhad, "Specific Absorbed Fractions of Internal Photon and Electron Emitters in a Human Voxel-based Phantom: A Monte Carlo Study", World Journal of Nuclear Medicine **16(2)**, 114–121 (2017) 10.4103/1450-1147.203065.

[68]M. Zankl, H. Schlattl, N. Petoussi-Henss, and C. Hoeschen, "Electron specific absorbed fractions for the adult male and female ICRP/ICRU reference computational phantoms", Physics in Medicine and Biology **57(14)**, 4501–4526 (2012) 10.1088/0031-9155/57/14/4501.

[69]N. Metropolis and S. Ulam, "The Monte Carlo Method", Journal of the American Statistical Association **44(247)**, 335–341 (1949).

[70]O. N. Vassiliev, *Monte Carlo Methods for Radiation Transport : Fundamentals and Advanced Topics* (Springer International Publishing AG, 2016), 10.1007/978-3-319-44141-2_1.

[71]J. Seco and F. Verhaegen, eds., *Monte Carlo Techniques in Radiation Therapy*, Imaging in medical diagnosis and therapy (CRC/Taylor Francis, Boca Raton, 2013).

[72]CERN, "Physics Reference Manual Documentation: Geant4 Collaboration Rev 5.0", (2017).

[73]M. Fippel, "Basics of Monte Carlo Simulations", in *Monte Carlo Techniques in Radiation Therapy* (CRC/Taylor Francis, 2013), 17–29.

[74]A. Kling, F. J. Barao, and M. Nakagawa, *Advanced Monte Carlo for Radiation Physics, Particle Transport Simulation and Applications, Proceedings of the monte carlo 2000 conference, lisbon, 23–26 october 2000* (Springer, Berlin, Heidelberg, 2001), pp. LII, 1192, https://doi.org/10.1007/978-3-642-18211-2.

[75]S. Jan, G. Santin, D. Strul, and S. Staelens, "GATE: a simulation toolkit for PET and SPECT", Physics in medicine and biology **49(19)**, 4543–4561 (2004) 10.1088/0031-9155/49/19/007.

[76]D. Rogers, "Fifty years of Monte Carlo simulations for medical physics", Physics in Medicine and Biology **51(13)**, R287–R301 (2006) 10.1088/0031-9155/51/13/r17.

[77]D. Bolst, *Silicon microdosimetry in hadron therapy using Geant4*, 2019.

[78]M. Vanstalle, I. Mattei, A. Sarti, F. Bellini, F. Bini, F. Collamati, E. D. Lucia, M. Durante, R. Faccini, F. Ferroni, C. Finck, S. Fiore, M. Marafini, V. Patera, L. Piersanti, M. Rovituso, C. Schuy, A. Sciubba, G. Traini, C. Voena, and C. L. Tessa, "Benchmarking Geant4 hadronic models for prompt- monitoring in carbon ion therapy", Medical physics (Lancaster) **44(8)**, 4276–4286 (2017) 10.1002/mp.12348.

[79]M. Pacilio, N. Lanconelli, M. Lo, M. Betti, L. Montani, A. Torres, and P. Coca, "Differences among Monte Carlo codes in the calculations of voxel S values for radionuclide targeted therapy and analysis of their impact on absorbed dose evaluations", Journal of Medical Physics **36(5)**, 1543–1552 (2009) 10.1118/1.3103401.

[80]OpenGate Collaboration, *GATE Users Guide V9.0*.

[81]"Report on the Task Group on Reference Man. ICRP Publication 23", Annals of the ICRP **4(3-4)**, edited by W. Snyder, 1–500 (1975) 10.1016/0146-6453(80)90047-0.

[82]R Core Team, "R: a language and environment for statistical computing", (2017).

[83]A. M. Loening and S. S. Gambhir, "Amide: a free software tool for multimodality medical image analysis", Molecular Imaging **2(3)**, 131–137 https://doi.org/10.1162/153535003322556877.

[84]T. J. Tewson and K. A. Krohn, "PET radiopharmaceuticals: state-of-the-art and future prospects", Seminars in nuclear medicine **28(3)**, 221–234 (1998) 10.1016/s0001-2998(98)80028-7.

Appendix A

Table of S values and Coefficients of variation

Table A.1 - A.4 present the S values (mGy $MBq^{-1}s^{-1}$) and the associated coefficient of variation for organs surrounding and including the liver. The four tables show these S values for the four phantoms; ICRP 110 female, ICRP 110 male, ICRP 145 female and ICRP 145 male in order. 10 million particles were simulated for each Monte Carlo simulation, with the coefficient of variation less than 1 for S values within the source organ a desirable result. The coefficient of variations are expressed as a real number, which when multiplied to the S value obtained, results in the error for the S value.

	0.1cm		0.5cm		1cm		3cm	
Liver	S [mGy $MBq^{-1}s^{-1}$]	Coefficient of Variation	S [mGy $MBq^{-1}s^{-1}$]	Coefficient of Variation	S [mGy $MBq^{-1}s^{-1}$]	Coefficient of Variation	S [mGy $MBq^{-1}s^{-1}$]	Coefficient of Variation
Y-90	9.455E-08	0.166	9.446E-08	0.149	9.437E-08	0.163	9.423E-08	0.146
Ho-166	9.833E-07	0.183	9.839E-07	0.182	9.828E-07	0.183	9.829E-07	0.182
Lu-177	1.289E-06	0.142	1.292E-06	0.189	1.289E-06	0.059	1.289E-06	0.059
Pancreas								
Y-90	2.209E-10	92.647	1.911E-10	88.771	0	0	1.139E-13	100
Ho-166	7.788E-12	100	6.184E-13	100	4.626E-12	100	3.941E-12	100
Lu-177	1.641E-13	100	4.662E-12	100	2.951E-12	77.928	4.691E-12	66.498
Gall bladder total								
Y-90	1.298E-10	51.002	1.216E-09	95.178	6.193E-10	76.793	9.951E-10	82.704
Ho-166	9.605E-11	100	0	0	0	0	2.811E-11	83.391
Lu-177	1.235E-11	90.727	5.794E-11	100	4.194E-11	38.232	8.955E-11	49.657
Small Intestine Total								
Y-90	1.468E-10	87.011	6.607E-11	99.285	0	0	7.237E-11	57.020
Ho-166	0	0	1.085E-12	98.889	0	0	8.035E-13	100
Lu-177	5.519E-13	100	2.019E-12	92.821	5.536E-12	49.533	3.330E-12	62.266
Lung Left								
Y-90	5.435E-13	100	4.040E-11	100	5.633E-12	63.627	0	0
Ho-166	2.912E-12	100	4.985E-13	100	0	0	0	0
Lu-177	2.672E-12	100	1.348E-13	100	1.073E-12	79.851	2.806E-12	93.814
Lung Right								
Y-90	2.617E-10	21.932	6.671E-10	60.625	2.921E-10	15.032	1.295E-09	50.627
Ho-166	1.469E-11	73.520	7.043E-12	79.705	5.022E-11	69.877	3.170E-11	65.503
Lu-177	5.443E-11	42.733	3.102E-11	53.587	4.189E-11	30.953	3.445E-11	16.702
Stomach Total								
Y-90	0	0	9.369E-11	100	3.502E-12	100	0	0
Ho-166	1.831E-12	100	2.237E-12	100	7.643E-12	100	0	0
Lu-177	1.428E-13	100	9.343E-14	100	5.324E-12	75.120	6.564E-12	59.676

Table A.1: ICRP 110 Female (AF) S values and Coefficient of variations. For a spherical lesion located in the liver ranging in diameter from 0.1cm to 3cm.

	0.1cm		0.5cm		1cm		3cm	
Liver	S [mGy $MBq^{-1}s^{-1}$]	Coefficient of Variation	S [mGy $MBq^{-1}s^{-1}$]	Coefficient of Variation	S [mGy $MBq^{-1}s^{-1}$]	Coefficient of Variation	S [mGy $MBq^{-1}s^{-1}$]	Coefficient of Variation
Y-90	7.295E-08	0.166	7.279E-08	0.154	7.296E-08	0.163	7.284E-08	0.169
Ho-166	7.585E-07	0.183	7.605E-07	0.182	7.606E-07	0.182	7.589E-07	0.182
Lu-177	9.948E-07	0.084	9.947E-07	0.085	9.943E-07	0.059	9.950E-07	0.059
Pancreas								
Y-90	2.883E-10	82.425	7.146E-11	36.225	6.440E-11	17.162	1.754E-10	51.270
Ho-166	1.495E-11	97.193	3.640E-14	100	1.335E-11	70.004	9.757E-12	100
Lu-177	2.725E-11	34.008	2.656E-11	39.258	2.242E-11	29.157	2.229E-11	29.675
Gall bladder total								
Y-90	1.257E-08	4.254	1.361E-08	7.015	1.678E-08	15.463	2.588E-08	2.975
Ho-166	9.469E-11	76.501	1.446E-10	73.168	1.019E-10	81.647	1.111E-10	81.387
Lu-177	1.905E-10	39.637	3.441E-10	33.505	3.214E-10	24.563	2.394E-10	23.064
Small Intestine Total								
Y-90	4.918E-11	72.586	9.855E-11	64.176	5.762E-12	55.125	3.514E-11	97.011
Ho-166	3.034E-12	100	2.529E-12	100	7.104E-13	100	4.109E-12	86.886
Lu-177	2.837E-12	74.517	8.688E-12	63.092	5.047E-12	38.477	4.161E-12	57.461
Lung Left								
Y-90	0	0	2.765E-11	76.863	2.869E-12	100	4.741E-11	100
Ho-166	1.546E-12	100	8.246E-13	100	0	0	1.297E-13	100
Lu-177	6.374E-13	100	6.596E-13	73.240	4.843E-12	96.612	1.004E-12	79.303
Lung Right								
Y-90	5.131E-11	75.762	1.091E-11	53.399	2.651E-10	75.315	3.000E-10	86.903
Ho-166	6.569E-12	91.638	6.243E-12	63.115	3.384E-12	74.163	1.173E-11	87.063
Lu-177	1.124E-11	28.921	1.526E-11	61.124	2.299E-11	37.729	2.013E-11	44.957
Stomach Total								
Y-90	9.453E-12	99.447	0	0	2.470-11	100	4.840E-12	76.635
Ho-166	9.181E-13	100	7.170E-13	100	3.806E-12	100	1.906E-12	100
Lu-177	5.902E-12	97.995	1.589E-11	60.027	8.040E-12	50.843	7.196E-12	60.966

Table A.2: ICRP 110 Male (AM) S values and Coefficient of variations. For a spherical lesion located in the liver ranging in diameter from 0.1cm to 3cm.

	0.1cm		0.5cm		1cm		3cm	
Liver	S [mGy $MBq^{-1}s^{-1}$]	Coefficient of Variation	S [mGy $MBq^{-1}s^{-1}$]	Coefficient of Variation	S [mGy $MBq^{-1}s^{-1}$]	Coefficient of Variation	S [mGy $MBq^{-1}s^{-1}$]	Coefficient of Variation
Y90	7.262E-08	0.147	7.244E-08	0.146	7.265E-08	0.153	7.239E-08	0.1512
Ho166	7.558E-07	0.181	7.557E-07	0.188	7.546E-07	0.152	7.541E-07	0.193
Lu177	9.883E-07	0.084	9.884E-07	0.167	9.888E-07	0.062	9.887E-07	0.063
Pancreas								
Y90	0	0	0	0	0	0	6.050E-11	67.816
Ho166	9.615E-13	81.388	0	0	3.969E-13	0.073	3.162E-12	100
Lu177	9.876E-13	60.528	7.871E-12	100	3.641E-12	75.861	5.987E-12	65.180
Gall bladder total								
Y90	3.475E-11	100	2.637E-10	79.155	8.052E-11	65.368	2.832E-11	44.071
Ho166	1.540E-11	100	0	0	1.703E-11	80.910	1.739E-13	100
Lu177	6.082E-12	64.777	2.045E-11	80.792	5.951E-11	88.059	2.664E-11	46.580
Small Intestine Total								
Y90	1.224E-10	57.751	1.218E-12	100	2.134E-11	56.987	5.229E-11	41.306
Ho166	3.925E-14	100	0	0	7.728E-14	0.1	2.738E-14	100
Lu177	9.266E-13	72.866	2.104E-12	100	4.604E-13	89.366	0	0
Lung Left								
Y90	0	0	0	0	2.483E-11	81.570	0	0
Ho166	2.466E-12	71.028	0	0	1.511E-12	98.131	1.181E-13	100
Lu177	7.651E-13	44.923	4.276E-12	84.802	1.641E-12	65.112	2.162E-12	52.409
Lung Right								
Y90	4.536E-10	5.906	4.725E-10	9.182	5.802E-10	7.301	7.250E-10	5.673
Ho166	1.393E-11	44.612	1.884E-11	43.810	1.920E-11	38.712	9.738E-12	58.277
Lu177	3.924E-11	16.430	3.342E-11	34.094	3.864E-11	10.681	3.360E-11	11.316
Stomach Total								
Y90	6.277E-11	90.505	0	0	1.963E-12	100	0	0
Ho166	8.168E-13	100	4.174E-14	100	3.284E-12	0.1	4.764E-13	92.548
Lu177	4.688E-12	64.466	1.394E-12	100	3.072E-10	98.832	7.940E-12	57.072

Table A.3: ICRP 145 Female (AF) S values and Coefficient of variations. For a spherical lesion located in the liver ranging in diameter from 0.1cm to 3cm.

	0.1cm		0.5cm		1cm		3cm	
Liver	S [mGy $MBq^{-1}s^{-1}$]	Coefficient of Variation	S [mGy $MBq^{-1}s^{-1}$]	Coefficient of Variation	S [mGy $MBq^{-1}s^{-1}$]	Coefficient of Variation	S [mGy $MBq^{-1}s^{-1}$]	Coefficient of Variation
Y90	5.581E-08	0.151	5.577E-08	0.147	5.571E-08	0.148	5.580E-08	0.151
Ho166	5.788E-07	0.186	5.794E-07	0.188	5.791E-07	0.190	5.793E-07	0.192
Lu177	7.583E-07	0.085	7.584E-07	0.087	7.591E-07	0.062	7.587E-07	0.062
Pancreas								
Y90	8.934E-11	77.626	1.087E-11	37.713	7.980E-12	44.348	1.892E-10	48.111
Ho166	6.956E-12	89.326	8.270E-12	57.964	7.587E-12	91.828	3.496E-12	92.307
Lu177	1.112E-11	58.244	1.474E-11	39.926	1.317E-11	35.427	1.173E-11	33.735
Gall bladder total								
Y90	1.000E-09	26.396	1.340E-09	28.415	9.475E-10	16.838	1.380E-09	14.037
Ho166	3.221E-11	78.460	8.479E-11	88.479	1.692E-11	69.471	1.137E-11	92.380
Lu177	1.805E-10	53.419	2.103E-10	45.980	1.064E-10	40.405	6.879E-11	28.516
Small Intestine Total								
Y90	1.735E-11	80.148	8.581E-12	65.692	8.023E-11	29.294	0	0
Ho166	2.369E-12	100	2.359E-12	97.482	3.046E-14	100	6.223E-13	100
Lu177	6.045E-12	71.996	2.127E-12	68.997	1.164E-12	72.605	4.997E-12	91.408
Lung Left								
Y90	2.977E-11	51.330	0	0	6.827E-13	100	7.586E-12	100
Ho166	1.373E-12	100	4.046E-14	100	0	0	0	0
Lu177	0	0	1.025E-12	92.334	1.679E-12	49.871	2.349E-14	100
Lung Right								
Y90	2.477E-11	53.941	2.708E-11	45.038	1.782E-11	45.164	5.661E-11	44.258
Ho166	3.619E-12	69.000	3.765E-12	78.259	1.025E-12	92.875	5.188E-12	69.608
Lu177	7.393E-12	30.121	8.958E-12	26.917	8.411E-12	20.897	9.130E-12	20.257
Stomach Total								
Y90	1.018E-10	100	2.975E-13	83.622	2.041E-12	73.181	3.246E-13	100
Ho166	6.968E-12	97.317	2.687E-12	88.115	6.496E-12	98.383	0	0
Lu177	5.166E-12	78.814	9.317E-12	65.461	6.271E-12	56.549	6.573E-11	99.475

Table A.4: ICRP 145 Male (AM) S values and Coefficient of variations. For a spherical lesion located in the liver ranging in diameter from 0.1cm to 3cm.

Appendix B

Requirements of Radiopharmaceuticals

All radiopharmaceuticals produced for biological and clinical use must:

- Use 'pure' radionuclide in the radiosynthesis of the radiopharmaceutical
- Have a high radiochemical purity, in correct chemical form (chemical purity) and in high specific activity
- Have the radiolabel incorporated in the correct position in the molecule
- Satisfy appropriate 'product release criteria'
- Bind, associate or incorporate within the biological target with high affinity, selectivity and specificity
- Be metabolically stable and must not interfere with the parent radiopharmaceutical or biological target
- Display appropriate kinetics, clearance rate and route, biological half-life

The product release criteria are quality control measures completed in nuclear medicine departments to ensure the radiopharmaceuticals produced are up to standard, and can be used in practice. These include:

- Physical appearance (colour, particle size, turbidity)
- Chemical purity
- pH
- Radiochemical purity
- Specific activity
- Radionuclidic purity
- Endotoxin (LAL)
- Sterility

- Environmental (Lab, air, benches, hot cells)
- Equipment (Cyclotron, radiochemistry molecules, instruments)

The product release criteria contain two important measurements relevant to radiopharmaceuticals and nuclear medicine. These are the compounds radiochemical purity and specific activity. Radiochemical purity is defined as the total radioactivity in the desired chemical form in the radiopharmaceutical sample. It is determined by measuring the half-lives and characteristic radiation emitted by individual radionuclides. This differs to the radionuclidic purity, which is the fraction of total radioactivity in the form of the desired radionuclide present in the radiopharmaceutical. Possible contamination in the sample can create an increased dose to the patient, and can cause incorrect counting rates in images.

The specific activity is defined as the amount of radioactivity per mass equivalent. The radionuclide has a large influence on the total mass of the radiopharmaceutical as the pharmaceutical mass is generally small. In order to not impact upon the biological processes occurring, the mass of the radionuclide must be low and hence the mass of the radiopharmaceutical must also be kept low. In order to keep the mass low and to fulfil its job in providing enough signal to detectors, the specific activity must be high [84].

A radionuclide may contain stable isotopes of the element of interest, called a carrier. If the sample doesn't contain a stable isotope of the element, it is called carrier free. The greatest possible specific activity is the carrier-free specific activity (CSFA), as it contains no stable isotopes in the sample [4]. These values are critical, as standardisation and consistency between and within nuclear medicine departments is important to ensure patient safety and correct dosages.

Other properties in the product release criteria are still important in the assessment of radiopharmaceuticals. The chemical purity is the fraction of the material in the desired chemical form of a sample. This is important as unwanted chemical impurities may cause toxic effects to patients, but also may cause incorrect labelling. The pharmaceutical which the radionuclide is attached to is also referred to as a tracer. A tracer is a radio-labelled molecule which follows a physiological or biochemical process. A suitable tracer will have known behaviours and is predictable, doesn't impact on the physiological or biochemical processes, has a small mass relative to the natural substance, and has a negligible difference between its mass and the mass of the radioisotope [4]. Some radiopharmaceuticals also require specific considerations for different applications. This includes the type and energy of emissions, which determine the availability of useful photons or gamma-rays for counting. Energies of 50-600 keV are useful for external detection as energies below this are highly likely to be absorbed in the body and won't be detected. This also increases dose to patients without providing useful information to practitioners. Finally, the physical half life of the radionuclide needs to be within the range of seconds to days (preferably minutes to hours), to allow for preparation, injection and imaging of the radiopharmaceutical. It is important that the half life is not extensively long, as a large part of the dosage will be incurred on the patient after the imaging procedure has occurred.

Nuclear medicine can be separated into diagnostic and therapeutic (more recently theranostic) dependent upon energies and half-life of radiopharmaceuticals. Diagnostic radiopharmaceuticals are primarily used for the imaging of disease in the body, whilst therapeutic radionuclides are used for the treatment of the disease. Diagnostic radiopharmaceuticals should have a short effective half-life to reduce dose to the patient whilst achieving the clinical goal. Diagnostic radiopharmaceuticals should also only emit gamma radiation to reduce dose to the patient to be easily imaged by gamma cameras. These pharmaceuticals should also have a high affinity for the target organ to reduce dose to non-target organs. This varies to therapeutic radiopharmaceuticals which should have particle emission (beta, alpha emission) to effectively treat tumorous cells. They should also have a relatively long half life (days) to allow the radiopharmaceutical enough time to treat the tumorous cells. A high activity is required to kill the cells as well. These considerations are all considered by a nuclear medicine physician and nuclear medicine physicist for the imaging and treatment of tumours cells in the body.

This demonstrates how vital radionuclides are in nuclear medicine, and highlights the rigorous preparation that needs to be completed.